ORNL/TM- 2024/3250

FUSION MATERIALS RESEARCH AT OAK RIDGE NATIONAL LABORATORY IN FISCAL YEAR 2023

Y. Katoh

C. On

C. M. Parish

August 2024

OAK RIDGE National Laboratory

ORNL IS MANAGED BY UT-BATTELLE LLC FOR THE US DEPARTMENT OF ENERGY

ORNL/TM- 2024/3250

Materials Science and Technology Division

FUSION MATERIALS RESEARCH AT OAK RIDGE NATIONAL LABORATORY IN FISCAL YEAR 2023

Complied by:
Y. Katoh
C. On
C. M. Parish

August 2024

Prepared by
OAK RIDGE NATIONAL LABORATORY
Oak Ridge, TN 37831
managed by
UT-BATTELLE LLC
for the
US DEPARTMENT OF ENERGY
under contract DE-AC05-00OR22725

CONTENTS

FIGURES

1. INTRODUCTION

Y. Katoh and C. M. Parish

The materials science challenge of providing a suite of suitable materials to satisfy the technology to achieve fusion energy is addressed in this ORNL program. The inability of currently available materials and components to withstand the harsh fusion nuclear environment requires development of new materials, and an understanding of their response to the fusion environment. The overarching goal of the ORNL Fusion Materials program is to provide the applied materials science support and materials understanding to underpin the ongoing DOE Office of Science—Fusion Energy Sciences program, in parallel with developing the materials for fusion power systems. In this effort the program continues to be integrated both with the larger U.S. and international fusion materials communities and with the U.S. and international fusion design and technology communities.

The excitement of this program comes from the priorities given to this subject in the two recent fusion reviews, by the FESAC and NAS committees. An important element of those recommendations is the support for pivoting the national R&D emphasis to the Fusion Materials and Technologies (FM&T), the long-advocated Fusion Prototypic Neutron Source, and for the Fusion Pilot Plant study that will help focus program direction and efforts. Furthermore, the surge of venture capital investment into the private fusion industry start-ups over the last few years is anticipated to help accelerate all aspects of the fusion energy development.

This twelfth annual report of the ORNL (Oak Ridge National Laboratory) Fusion Reactor Materials Program summarizes the accomplishments in Fiscal Year 2023 (FY2023). The year was the first to return to full post-COVID-restriction operations, with students and international assignees no longer impacted by COVID restrictions, as in FY20-21-22.

Following the pattern of planning used in this program, work for the year FY2023 focused on having the data and productivity to support a strong presence at the International Conference on Fusion Reactor Materials (ICFRM) 21, organized by Spain and occurred in October 2023. Twenty-nine ORNL-led abstracts were submitted, with all accepted. Four were invited presentations, nine contributed oral, fourteen posters, and two withdrawn due to unforeseen circumstances. Additionally, nine external abstracts with ORNL contributing authors were presented. These will be reported in the FY24 report next year.

Two ARPA-E/FES jointly funded GAMOW awards focusing on fusion materials development initiated in FY2021 continued into FY2023. A collaboration with LLNL (Lawrence Livermore National Laboratory) and TAMU (Texas A&M University) is exploring Additive Manufacturing options for fabrication of Plasma Facing Components, and an ORNL effort is scaling up Castable Nanostructured Alloy production. Both projects continued actively with excellent productivity through FY2023.

The major elements of this long-running ORNL program continue to pursue development of low activation structural materials, with the greatest effort directed at the Reduced Activation Ferritic/Martensitic (RAFM) Steels, higher strength/higher creep resistant/coolant compatible/radiation tolerant advanced steels, and silicon carbide composites. Tasks within the steels portfolio are pursuing several options for advanced steels: these include development of castable nanostructured alloys (CNAs), exploratory work on bainitic steels and oxide dispersion strengthened (ODS) steels, and aluminum-containing iron-based alloys that promise improved liquid metal compatibility. Parallel to this is the increased emphasis on radiation effects, high heat flux testing and the development of refractory metals, especially tungsten materials. This includes the development and evaluation of new tungsten materials, and the study and understanding of the irradiation performance of tungsten. Newer efforts also support the Blanket and Fuel Cycle Programs. In each case the materials are being developed in a design-informed fashion where properties improvements

are led by fusion-relevant design studies and directed at advancing the Technology Readiness Level (TRL) of the material systems.

Effort continues on tasks initiated in FY2019, including the investigation of application of Additive Manufacturing (AM) technologies to the production of materials and components for fusion systems. While the development of tungsten AM technologies and compositionally graded tungsten-RAFMS transition was transferred to an FES/ARPA-E GAMOW program, fundamental study on thermal stability of the transition continues in this research. Moreover, development of additively nanostructured RAFMS and AM SiC ceramics & composites are explored.

Limited integrated fundamental modeling is included in the program, directed especially at understanding experimentally observed behavior. Recent focus has been on the irradiation effects in the W-Re-Os system and on exploring new options for solid ceramic tritium breeder candidate materials. Modeling under the MPEX Digital Twin program is a synergistic activity.

This fusion materials program makes heavy reliance on neutron irradiation in the High Flux Isotope Reactor (HFIR) at ORNL, complemented by limited use of ion irradiation facilities when these are better suited to explore fundamental aspects of materials behavior under irradiation. Associated with the HFIR irradiations is the infrastructure needed to evaluate the effects of the irradiation on the material properties and microstructures. This infrastructure includes: 1) hot cells, which are needed for capsule/experiment disassembly and for testing highly radioactive specimens; and 2) the Low Activation Materials Development and Analysis (LAMDA) Laboratory, which contains shielded test equipment for lower-level radioactive materials. Maintaining, upgrading, and replacing these state-of-the-art suites of instruments and test stands is an ongoing effort, shared with other programs focused on similar needs. ORNL provided ICE (Institutional Capital Equipment) funds of approximately $2.3M in FY23 to purchase a state-of-the-art plasma focused ion beam (PFIB) to be located in LAMDA. This tool will be installed in FY24 and will support in part Fusion Materials. ORNL made a decision of providing additional ICE funds in FY24 to purchase an analytical scanning electron microscope (SEM) to support its applied materials programs, including Fusion Materials.

The fusion materials effort consists of a wide array of tasks and collaborations with both US and international partners. The major continuing international collaborating partners are the Japan Agency for Quantum and Radiological Science and Technology (QST), focused on structural materials, the Japanese National Institute for Fusion Sciences (the FRONTIER collaboration) and the Karlsruhe Institute of Technology in Germany, acting for EUROfusion (examining steel materials). A collaboration with the United Kingdom Atomic Energy Authority (UK AEA) formally began in FY2023.

Productivity and recognition of the ORNL Fusion Materials Program is demonstrated in Chapter 14 Awards, Honors and Recognition and Chapter 15 Publications and Presentations.

This research is funded by the Department of Energy, Office of Science, Office of Fusion Energy Sciences. We would like to acknowledge the active guidance that Guin Shaw of FES provides in setting the direction and priorities of this work, and her help in the effective conduct of the program.

2. ADVANCED STEELS

2.1 PERFORMANCE EVALUATION OF MODIFIED 3Cr-3WVTa BAINITIC STEELS

*Y. Yamamoto**
**yamamotoy@ornl.gov*

2.1.1 OBJECTIVE

This work aims to evaluate the advantages in the mechanical performance of newly proposed, modified 3Cr-3WVTa bainitic steels developed at ORNL. The proposed steel was designed to eliminate the need for post-weld heat treatment (PWHT), as well as providing improved mechanical properties of both base metal and weldments compared to those of existing commercial bainitic steels or ferritic-martensitic (F-M) steels. The target applications are high-temperature structural components in fusion reactors, such as helium-cooled vacuum vessels operating up to 450°C and blanket support structures operating up to 550°C. An optimization of thermomechanical treatment has been applied targeting the improvement of mechanical properties, especially for long-term creep performance as well as impact toughness after long-term isothermal exposure. The property improvements are to be measured by experimental approaches.

2.1.2 SUMMARY

There are two major updates on property evaluation of the "process-optimized" modified 3Cr-3WVTa steel: (1) the long-term creep-rupture tests of the base metal and cross-weld specimens, and (2) microstructure characterization and property evaluation of the isothermally aged modified 3Cr-3WVTa steel after applying an optimized thermomechanical treatment. A significant improvement of the base metal creep-rupture performance was observed in the process-optimized steel with more than doubled creep-rupture life at 550°C and 295MPa in the normalized-and-tempered condition. The cross-weld specimens of the process-optimized steel also achieved ~20% improvement of the creep strength compared to non-optimized cross-weld specimens. The long-term isothermal aging at 500°C for up to 10,000 h resulted in almost no changes in the microstructure, and only a significantly small amount of hardness reduction compared to the same material tempered at 700°C for 1 h. However, the reduction of impact toughness was also observed after only 1,000 h aging at 500°C. Detailed characterization is currently in progress to understand the embrittlement mechanism.

2.1.3 PROGRESS AND STATUS

A compositionally modified 3Cr-3WVTa bainitic ferritic steel (Mod. 3Cr-3WVTa steel, ID: MLC02T) was proposed with an advanced alloy design to improve the homogeneity across the weldment in the as-welded condition, targeting a PWHT-free bainitic ferritic steel for fusion structural applications. The nominal compositions of the original and modified steels are summarized in Table 1. Initial property evaluation of the modified steel suggested that the as-normalized MLC02T exhibited an improved room-temperature impact toughness compared to that after applying tempering, as opposed to the response in typical low-alloyed bainitic steels.

Table 1. Nominal composition of 3Cr-3WVTa base bainitic steels (balanced Fe).

Name	Alloy composition, wt.%	Remarks
MLC02T	3Cr-3W-0.2V-0.16Si-2.0Mn-0.1Ta-0.05C	Modified (newly proposed)
Original	3Cr-3W-0.2V-0.16Si-0.4Mn-0.1Ta-0.1C	Require PWHT, proposed in 1990's [ref.]

[ref.] R.L. Klueh et al., Int. J. Pressure Vessels and Piping, 84 (2007) 29-36.

Based on the initial results, the focus of systematic performance evaluation has been shifted to the as-normalized condition. In addition, a refinement of the prior austenite grains (PAG) was also conducted through optimization of thermomechanical treatments as well as normalization temperature, as reported previously, targeting the improved room-temperature mechanical properties including both tensile and toughness. The present report summarizes the progress of property evaluation of MLC02T with the refined PAG in the as-normalized condition.

A cast ingot of MLC02T produced through vacuum-induction-melting was homogenized at 1200°C, followed by hot-rolling and normalization at 1000°C to prepare an as-normalized plate with ~15 mm thickness and average PAG size of ~40 μm. A small piece was sectioned from the plate which applied tempering at 700°C to compare the mechanical performance with and without tempering. Uni-axial tensile creep-rupture tests of the base metal in the as-normalized and normalized-and-tempered conditions were conducted at 500 and 550°C. A part of the as-normalized plate was machined to have a single V groove and then applied a gas tungsten arc weld (GTAW) with a compositionally matched weld filler metal strip. The creep-rupture performance across the weldment was also evaluated at 500 and 550°C.

Three creep-rupture tests at 500 and 550°C of the as-normalized MLC02T base metal with refined PAG and as-welded (gas-tungsten arc weld or GTAW) specimens are currently in progress, as summarized with Larson-Miller Parameter in Figure 1a. The creep-rupture strength of the as-normalized base metal showed ~35% improvement to date compared to that of previously evaluated MLC02T (normalized at 1100°C + tempered). Direct comparison of the creep-rupture curves of the normalized-and-tempered MLC02T tested at 550°C and 295MPa (Figure 1b) indicated an apparent improvement of creep-deformation resistance by applying normalization at 1000°C, followed by tempering, with more than double creep-rupture life (6,274 h) compared to the non-optimized specimens (2,857 h). The as-normalized material of the process-optimized MLC02T specimen resulted in further improvement of creep-rupture life of 13,693 h at the given test condition. The cross-weld specimens of the process-optimized MLC02T steel also achieved ~20% improvement of the creep strength compared to non-optimized cross-weld specimens, indicating the effectiveness of the process optimization of the modified 3Cr-3WVTa steel in the creep performance of both base metal and the weldment.

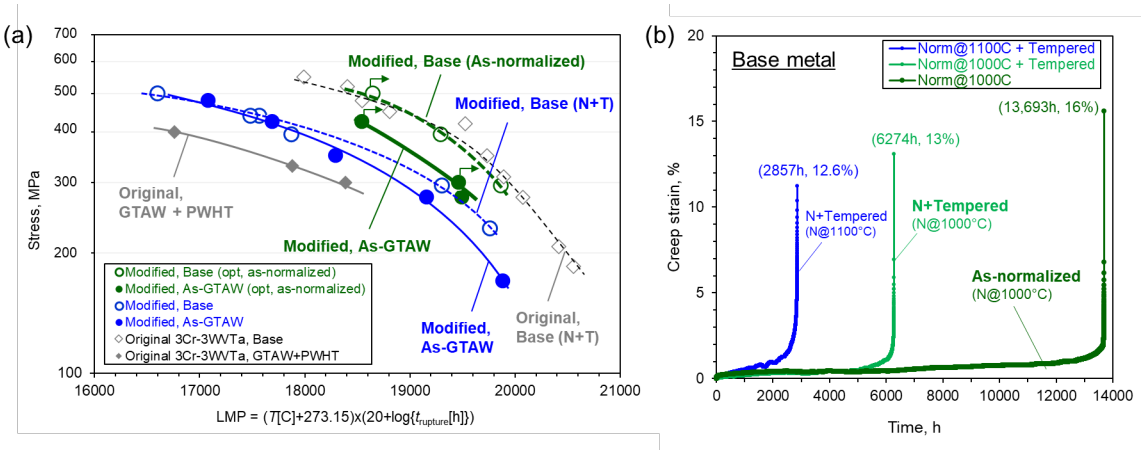

Figure 1. (a) Larson-Miller Parameter (LMP) plot of the process optimized MLC02T steel base metal and as-GTAW specimens, comparing with previously evaluated materials, and (b) creep-rupture curves of the modified 3Cr-3WVTa steel before and after re-normalization at 1,000°C, tested at 550°C and 295MPa.

Isothermal aging at 500°C in a laboratory air for up to 10,000 h was conducted for evaluation of long-term thermal stability in microstructure and mechanical performance of the process-optimized MLC02T plate in the as-normalized condition. Figure 2 represents optical micrographs of the process-optimized MLC02T steel aged for 1,000 h, 3,000 h, and 10,000 h compared to the as-normalized microstructure. The as-normalized specimen showed a fully bainitic microstructure, and the microstructural characteristics including prior-austenite grain (PAG) size and acicular bainite ferrite structure showed no significant changes including recrystallization or grain coarsening, even after 10,000 h exposure. Optical micrographs also indicated secondary phase precipitation inside the acicular bainite ferrite, although a detailed SEM characterization would require identifying the types of precipitates.

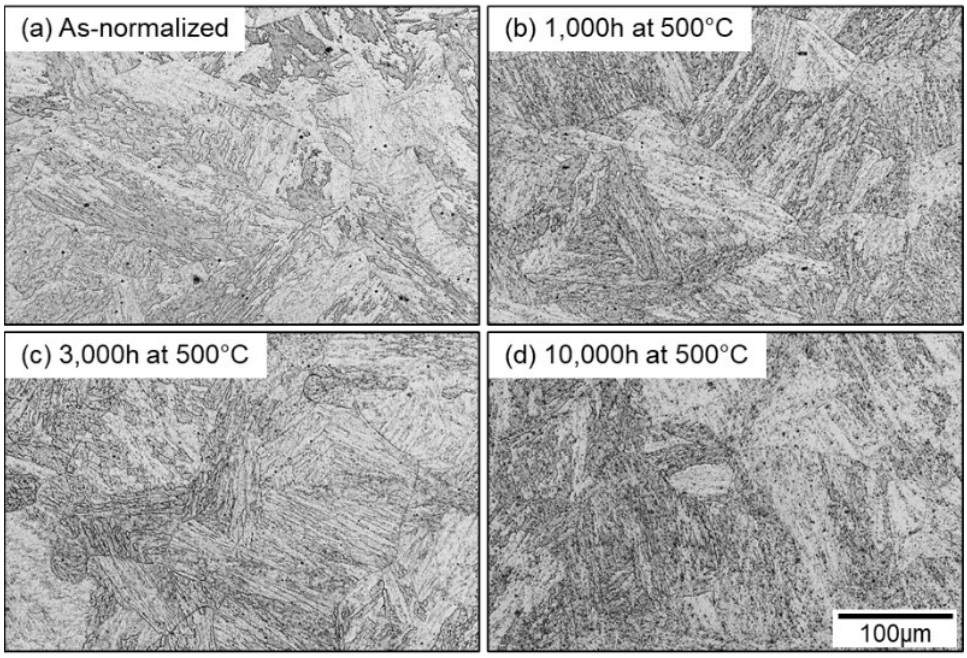

Figure 2. Optical micrographs showing fully bainitic structure of the process-optimized MLC02T before and after aging at 500°C: (a) as-normalized, (b) aged for 1,000 h, (c) 3,000 h, and (d) 10,000 h.

Figure 3a shows micro-Vickers hardness (HV0.5, averaged 25 indent measurements) of the process-optimized MLC02T steel plotted as a function of aging time at 500°C. The hardness values of the same material after tempering at 680°C or 700°C for 1 h are also plotted for comparison. The hardness showed very little change during aging, from 318 ± 9 HV in the as-normalized condition to 309 ± 10 HV after 10,000 h aging. The amount of the hardness reduction was significantly smaller than the same material tempered at 700°C for 1h (244HV) or even at 680°C for 1 h (300HV). Based on both microstructure characterization and hardness measurement, it is speculated that the microstructural stability of the process-optimized MLC02T steel at 500°C could be correlated with the small change in the hardness, which may lead to thermal stability of the other mechanical properties such as the long-term creep-rupture strength as discussed in Figure 1. However, as shown in Figure 3b, the Charpy impact toughness dropped significantly only after 1,000h aging, and the data was scattered with very low impact toughness even after 10,000h aging. Preliminary cross-sectional microstructure characterization of the Charpy tested specimens after 10,000h aging indicated that a lot of decohesion along the primary austenite grain boundaries (PAGBs) appeared near the fracture surface, regardless of either high or low absorbed energies (146 J and 4.6 J, respectively). This result suggests the susceptibility of crack formation along the PAGBs increased in the MLC02T when the material was thermally exposed at the expected service temperatures (400-550°C), which would not be negligible when considered the soundness of the structural components. It is important to understand the mechanism how this embrittlement appeared during the thermal exposure of MLC02T, and detailed microstructure characterization and compositional analysis near the PAGB are currently in progress.

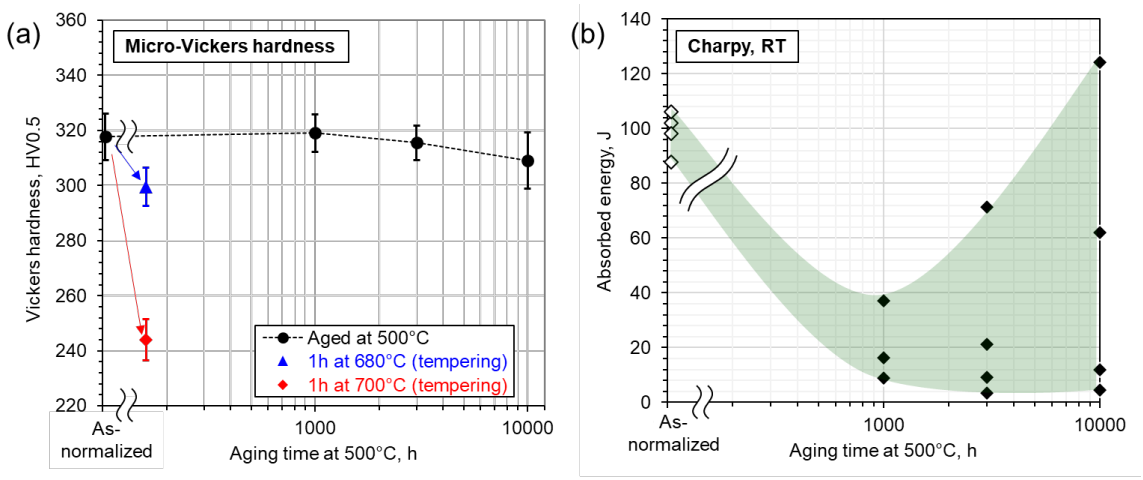

Figure 3. (a) Micro-Vickers hardness and (b) Charpy impact toughness, plotted as a function of aging time at 500°C. The hardness was also compared with those after tempering at 680 and 700°C for 1h.

2.1.4 FUTURE RESEARCH

Detailed microstructure characterization of the long-term creep-ruptured and isothermally aged MLC02T will be conducted to be correlated with the process or test conditions. Evaluation of the creep-rupture performance will be continued, and Charpy impact toughness and tensile tests of the isothermally aged samples will also be conducted. A compositionally matched metal-core wire of MLC02T steel was produced and a wall has been printed through wire-DED process, so that the microstructure characterization and property evaluation will also be conducted.

2.2 MICROSTRUCTURE AND TENSILE PROPERTIES OF 0.25-TON SCALE CASTABLE NANOSTRUCTURED ALLOY ROD

W. Zhong, Y. Wang, Y. Yang*
**zhongw@ornl.gov*

Supported by DOE-FES and ARPA-E

2.2.1 OBJECTIVE

Lab-scale castable nanostructured alloys (CNA) have shown promising properties as fusion structural materials [1]. To meet the fusion industry needs, scalability of CNAs must be examined. The objective of this project is to demonstrate the scalability of CNA for production and performance for use as fusion first wall and blanket structural materials. A quarter-ton scale CNA rod batch was fabricated, and the examination of multiple properties is ongoing. In addition, fabrication of multi-ton scale CNA plates is ongoing.

2.2.2 SUMMARY

This work investigates the properties of 0.25-ton heat CNA rods, which were fabricated by Metalwerks Inc. Multiple heat treatments have been performed on CNA rods, the optimized heat treatment was identified, and the hardness of materials were found to satisfy the desired criteria (102 ± 3 HRB). Microstructural characterization was performed on the CNA to examine grain structure and precipitate distribution. The result of precipitate size and distribution is reported here. $Cr_{23}C_6$ precipitates of 30-150 nm were observed at grain boundaries with number densities on the order of 10^{19} m^{-3}. Both coarse (50-250 nm) TiC precipitates with low number density (~10^{17} m^{-3}) and ultrafine (3-10 nm) TiC precipitates with high number density (~10^{21} m^{-3}) were observed, and they were distributed inside the matrix. Tensile tests were performed at room temperature as well as elevated temperatures up to 700°C with 1 – 4 tests per temperature following ASTM standards E8 and E21. Comparing to Eurofer 97, CNA demonstrates higher tensile yield strength and ultimate tensile strength, with slightly lower total elongation and area reduction.

2.2.3 PROGRESS AND STATUS

As-received 0.25-ton scale CNA rods (1 inch diameter) from Metalwerks require additional heat treatment to meet the hardness design specification of 102 ± 3 HRB. An optimized heat treatment (designed as HT7) was selected based on the screening tensile tests using SS-J3 samples. These optimized CNA were normalized at 1180°C for 10 minutes, followed by water quenching. Tempering was then performed at 710°C for 60 minutes with subsequent air cooling.

Scanning transmission electron microscopy (STEM) was used to characterize the precipitates' distribution in the CNA rods. Figure 4 shows the dark field STEM image and Ti/Cr energy dispersive spectroscopy (EDS) maps of the TEM sample that was prepared at the center of a 25.4 mm diameter rod. $Cr_{23}C_6$ precipitates were distributed at boundaries with sizes of 30-150 nm and number densities on the order of 10^{19} m^{-3}. A few coarse (50 – 250 nm) TiC precipitates were observed with a lower number density on the order of 10^{17} m^{-3}. The presence of these coarse TiC precipitates is likely attributed to the undissolved TiC precipitates from the normalization step in the additional heat treatment. In addition to these coarse TiC precipitates, ultrafine TiC precipitates (~3-10 nm) were observed, as shown in the dark field STEM image and Ti EDS map in Figure 5. These ultrafine TiC precipitates have a high number density of the order of 10^{21} m^{-3}.

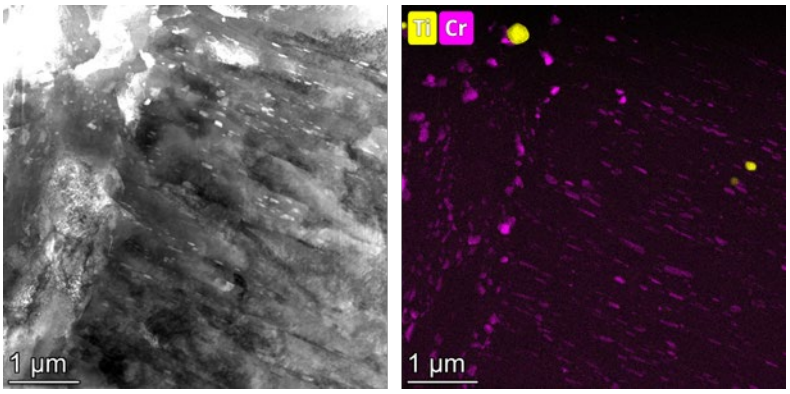

Figure 4. (left) Dark field STEM image and (right) Ti/Cr EDS maps showing the distribution of $Cr_{23}C_6$ and coarse TiC particles in the CNA rods with optimized heat treatment.

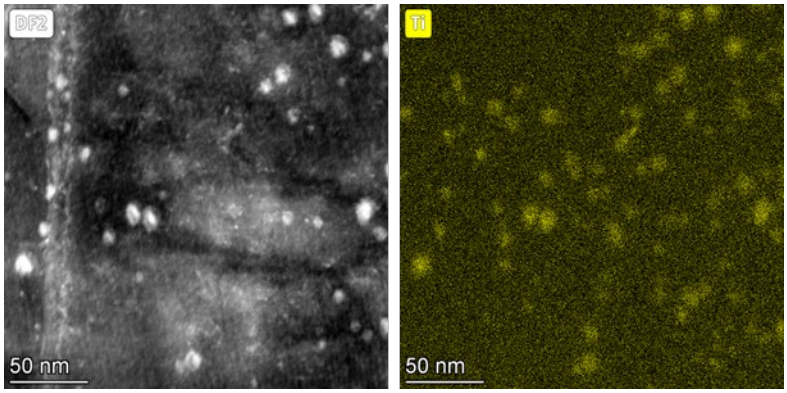

Figure 5. (left) Dark field STEM image and (right) Ti EDS map showing the distribution of ultrafine TiC precipitates in the matrix of CNA rods with optimized heat treatment.

To investigate the tensile properties of CNA rods, ASTM-standard tensile samples with 6.35 mm diameter and nominal gage length of 32 mm were machined from the CNA rods with optimized heat treatment. Tensile tests were performed in air. The tensile testing procedure follows ASTM E8 for room temperature testing and ASTM E21 for elevated temperature testing. Figure 6 shows the 0.2% offset yield stress, total elongation, and area reduction of CNAs, in comparison to Eurofer 97 [2]. CNA rods demonstrate higher yield strength than Eurofer 97 for all investigated temperatures, with the increases of ~140 MPa and ~70 MPa at 23°C and 700°C, respectively. The higher yield strengths are accompanied by reduced elongation and smaller reductions of area for the CNA rods.

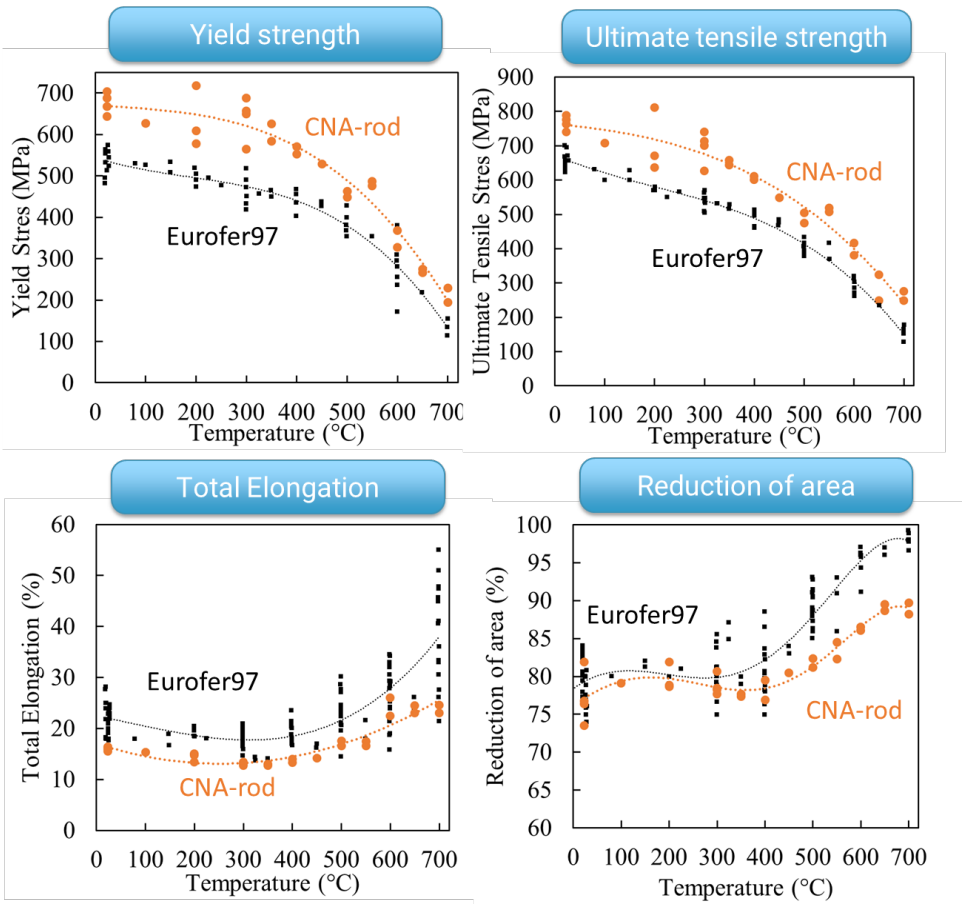

Figure 6. 0.2% offset yield strength, ultimate tensile strength, total elongation, and reduction of area of CNA tensile properties, in comparison to Eurofer97 [2], during testing at temperatures up to 700°C.

2.2.4 FUTURE RESEARCH

Other properties of CNA rods are under investigation, such as creep, fracture toughness, low-cycle fatigue properties, weldability, and compatibility with liquid-metal coolants. In addition, fabrication of multi-ton CNA plates are on-going, which will be followed by microstructure characterization and mechanical property testing on the CNA plates.

2.2.5 REFERENCES

[1] L. Tan, T. Graening, X. Hu, W. Zhong, Y. Yang, S. J. Zinkle, and Y. Katoh. Effects of carbonitrides and carbides on microstructure and properties of castable nanostructured alloys, J. Nucl. Mater. 540 (2020): 152376.

[2] E. Lucon, and W. Vandermeulen. Overview and Critical Assessment of the Tensile Properties of unirradiated and irradiated EUROFER97. No. BLG--1042. Belgian Nuclear Research Center SCK-CEN (Belgium), 2007.

2.3 CHARPY IMPACT TESTING OF CNA STEELS AFTER DIFFERENT HEAT TREATMENTS

X. Chen, W. Zhong, Y. Yang*
**chenx2@ornl.gov*

Supported by DOE-FES and ARPA-E

2.3.1 OBJECTIVE

Reduced-Activation Ferritic-Martensitic (RAFM) steels are essential candidate materials for first-wall/blanket applications of fusion energy. To increase the operation temperature window of the current benchmark RAFM steels, Castable Nanostructured Alloys (CNAs) have been developed and examined in laboratory-scale heats, which demonstrated improvements in various properties that are critical to fusion applications. To establish a US-RAFM steel based on CNAs, it is vital to perform property and microstructure evaluation of industry-scale heats of CNAs and benchmark their performance against laboratory-scale CNAs and current RAFM steels, e.g., F82H and EUROFER97. In this task, we focus on the Charpy impact testing of CNA steels after different heat treatments.

2.3.2 SUMMARY

Our goal is to determine the optimal heat treatment condition for the CNA 5-ton heat, which is critical for upscaling the US candidate RAFM steel. We want to achieve a high level of hardness and strength, as well as a good resistance to fracture and impact. To do this, we are testing how different heat treatment parameters affect the mechanical properties of the CNA rod, such as the hardness and the Charpy impact energy. By analyzing the results, we hope to find the best combination of heat treatment conditions that can enhance both the strength and the fracture toughness of the CNA rod.

2.3.3 PROGRESS AND STATUS

0.25-ton scale CNA rods (1 inch diameter) from Metalwerks were used for Charpy specimen machining as shown in Figure 7. Different heat treatment conditions, summarized in Table 2, were applied to the rod material to optimize the hardness and Charpy impact properties. Standard full-size Charpy specimens with a dimension of 55 × 10 × 10 mm^3 were machined in the LC orientation. Charpy impact testing was performed with an Instron Charpy frame with an MPM in-situ heating/cooling stage as shown in Figure 8.

The Charpy impact energy results are shown in Figure 9. The CNA rod material exhibited the classic ductile to brittle transition behavior of ferritic steels. The 41J ductile-to-brittle transition temperature (DBTT) was 2°C and the upper shelf energy (USE) was 308 J for the HT7 treatment. Corresponding values for the HT9 treatment were -12°C and 392 J. For the remaining heat treatment conditions, only room temperature Charpy tests were performed as an initial screening. Among those results, HT10 and HT11 showed the highest Charpy impact energy, while the Charpy impact results were similar for HT8, HT12, HT13, and HT14. In summary, the room temperature Charpy impact energy follows the order of HT10 ≈ HT11 > HT8 ≈ HT9 ≈ HT12 ≈ HT13 ≈ HT14 > HT7 (see As-received 0.25-ton scale CNA rods (1 inch diameter) from Metalwerks require additional heat treatment to meet the hardness design specification of 102 ± 3 HRB. An optimized heat treatment (designed as HT7) was selected based on the screening tensile tests using SS-J3 samples. These optimized CNA were normalized at 1180°C for 10 minutes, followed by water quenching. Tempering was then performed at 710°C for 60 minutes with subsequent air cooling.

Scanning transmission electron microscopy (STEM) was used to characterize the precipitates' distribution in the CNA rods. Figure 4 shows the dark field STEM image and Ti/Cr energy dispersive spectroscopy (EDS) maps of the TEM sample that was prepared at the center of a 25.4 mm diameter rod. $Cr_{23}C_6$ precipitates were distributed at boundaries with sizes of 30-150 nm and number densities on the order of 10^{19} m^{-3}. A few coarse (50 – 250 nm) TiC precipitates were observed with a lower number density on the order of 10^{17} m^{-3}. The presence of these coarse TiC precipitates is likely attributed to the undissolved TiC precipitates from the normalization step in the additional heat treatment. In addition to these coarse TiC precipitates, ultrafine TiC precipitates (~3-10 nm) were observed, as shown in the dark field STEM image and Ti EDS map in Figure 5. These ultrafine TiC precipitates have a high number density of the order of 10^{21} m^{-3}.).

Besides Charpy impact testing, Vickers hardness measurements were also performed. Table 3 lists the available results. The data suggest a negative relationship between the hardness and the impact energy at room temperature. More tests are underway to confirm this finding.

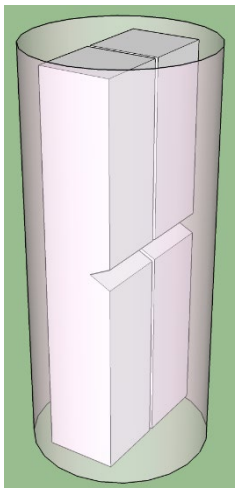

Figure 7. Schematic of Charpy specimen machining from 1" diameter CNA Rod.

Table 2. Heat treatment conditions applied for CNA rods.

Heat treatment ID	Normalization	Cooling after normalization	Tempering	Cooling after tempering	Room temperature Charpy (J)
HT7	1180°C/10 min	Water quench	710°C/60 min	Air cool	32, 97, 184
HT8	1170°C/30 min	Water quench	730°C/60 min	Air cool	186, 196, 202, 220
HT9	1170°C/30 min	Water quench	750°C/60 min	Air cool	54, 218, 238, 253
HT10	1170°C/30 min	Water quench	750°C/120 min	Air cool	311, 339
HT11	1130°C/30 min	Water quench	750°C/60 min	Air cool	289, 396
HT12	1170°C/30 min	Water quench	710°C/60 min	Air cool	218, 257
HT13	1170°C/30 min	Water quench	710°C/120 min	Air cool	219, 249
HT14	1170°C/30 min	Water quench	710°C/180 min	Air cool	142, 225

Figure 8. Instron Charpy impact frame equipped with an MPM in-situ heating/cooling stage.

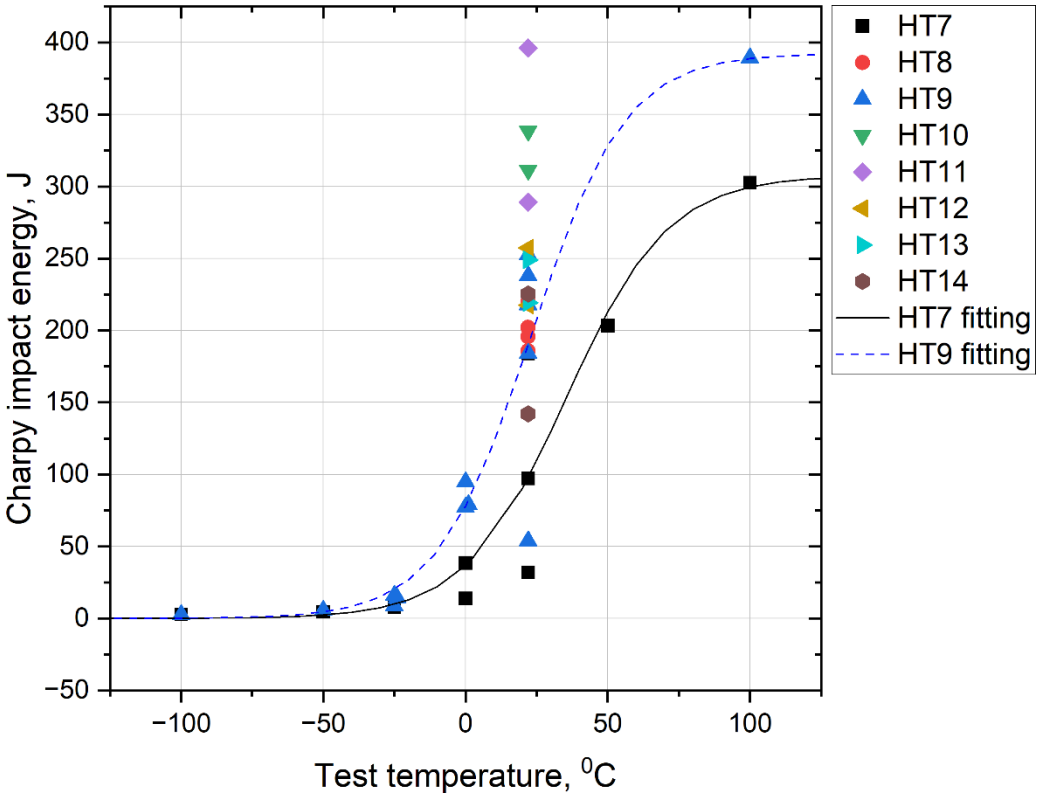

Figure 9. Charpy impact results of CNA rods after different heat treatment conditions.

Table 3. Vickers hardness results of CNA rods after different heat treatment conditions.

Heat treatment ID	Vickers hardness (10kgf)	Standard deviation
HT7	271.7	2.7

HT8	TBD	TBD
HT9	229.3	1.4
HT10	214.0	1.1
HT11	209.7	3.5
HT12	236.3	7.3
HT13	231.8	1.2
HT14	232.2	4.0

2.3.4 FUTURE RESEARCH

Additional microstructural characterization is being performed to elucidate the microstructure-property correlation. The results will be used to guide the determination of the optimal heat treatment for the CNA 5-ton heat.

2.4 THE MICROSTRUCTURE EFFECTS ON IRRADIATION RESPONSE OF FERRITIC-MARTENSITIC STEELS

W. Zhong, L. Tan*
**zhongw@ornl.gov*

2.4.1 OBJECTIVE

Reduced activation ferritic-martensitic (FM) steels are one of the candidates for fusion first wall and blanket structural materials application. The objective of this work is to investigate the neutron irradiation effects on the tensile properties and microstructural evolution of two FM steels. In this work, the tensile properties of two irradiated FM steels are reported, in comparison to the unirradiated materials. Microstructures of these FM steels before and after irradiation are also presented.

2.4.2 SUMMARY

Two ferritic-martensitic steels (9Cr-Ta and 9Cr-NbMo) were irradiated in High Flux Isotope Reactor (HFIR), and their post-irradiation tensile properties were tested and compared. Irradiation-induced hardening at 400°C (≈0.38 T_M) was observed for both materials, which is commonly observed for FM steels at low irradiation temperature (< ~0.45 T_M). Following irradiation at 490°C to 7.4 dpa, different tensile behaviors were observed. 9Cr-Ta exhibits irradiation induced softening, whereas 9Cr-NbMo maintains similar strength, compared to the unirradiated materials. Microstructure characterization on the pre-irradiated materials showed different microstructures. 9Cr-Ta has a smaller grain size, whereas 9Cr-NbMo has a higher dislocation density and higher number density of precipitates. After irradiation, dislocation loops and cavities were observed in 9Cr-Ta, as reported in Ref. [1]. On the other hands, no dislocation loops were observed in 9Cr-NbMo, but nanoscale cavities were visible.

2.4.3 PROGRESS AND STATUS

Two 9% Cr FM steels were investigated to understand the effects of irradiation on their tensile properties. The compositions of these two steels are Fe-8.9%Cr-1.9%W-0.47%Mn-0.14%Si-0.2V-0.4%Mo-0.1%Nb-0.1%Ni-0.1%C-0.05%N (designated as 9Cr-NbMo) and Fe-9.0%Cr-1.1%W-0.46%Mn-0.23%Si-0.3%V-0.1%Ta-0.1%C-0.05%N (designed as 9Cr-Ta) respectively. Shown in Figure 10 are the stress–strain curves for the unirradiated and irradiated materials, both of which were tested at room temperature; the solid lines represent 9Cr-NbMo, and dashed lines represent 9Cr-Ta. The irradiation conditions were labeled using the same colors as the stress–strain curves. Before irradiation, the tensile behaviors for 9Cr-NbMo and 9Cr-Ta are similar, as indicated by the black curves. The yield strength of these alloys are ~744 – 773MPa.

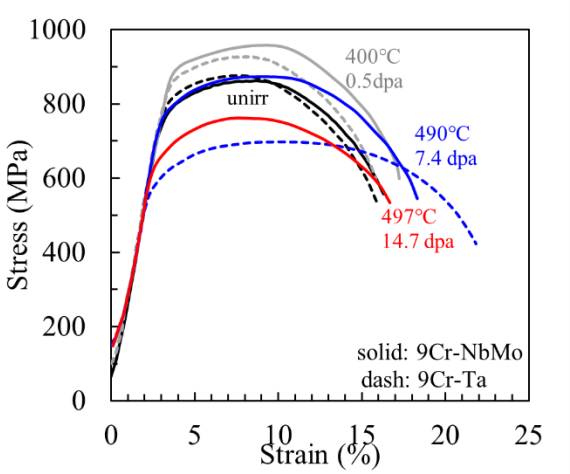

Figure 10. Stress–strain curves of unirradiated and irradiated 9Cr-NbMo (solid curves) and 9Cr-Ta (dashed curves) alloys. Tensile tests were performed at room temperature.

After the irradiation at lower temperature (400°C, 0.5 dpa), both alloys exhibit irradiation-induced hardening by about 50–130 MPa. Such irradiation-induced hardening is consistent with the hardening that has commonly been observed in FM steels at low irradiation temperature (less than about < ~0.45T_M). At higher irradiation temperature (490°C, 7.4 dpa), 9Cr-Ta exhibited irradiation-induced softening: yield stress decreased by about 27% to 565 MPa. By contrast, under the same irradiation conditions, 9Cr-NbMo maintained yield stress of 761 MPa, like the unirradiated materials (744 MPa). Extended irradiation to 14.7 dpa causes softening to 641 MPa in 9Cr-NbMo.

Microstructure characterizations were performed on the unirradiated materials. Figure 11 shows the inverse pole figure of these two alloys with the insets showing high-angle boundaries (>15 degrees). The intercept method was used to examine the grain size. The mean number of intersections per unit length are 0.23 ± 0.03 μm^{-1} and 0.35 ± 0.03 μm^{-1}, corresponding to average grain sizes of 4.3 ± 0.5 μm and 2.8 ± 0.3 μm for 9Cr-NbMo and 9Cr-Ta, respectively.

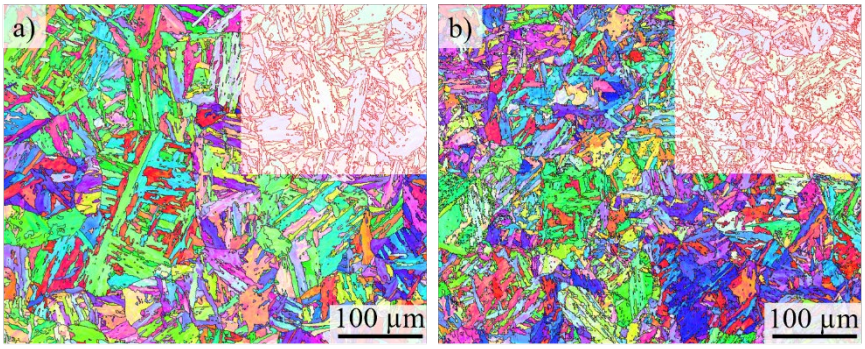

Figure 11. Inverse pole figure maps for unirradiated (left) 9Cr-NbMo alloy and (right) 9Cr-Ta alloys with the high angle grain boundary distributions shown in the insets.

Transmission electron microscopy (TEM) was used to identify the precipitate and dislocation structure in both alloys. The Cr/V energy dispersive spectroscopy (EDS) maps in Figure 12a and Figure 12b reveal the distribution of $Cr_{23}C_6$ and MX precipitates in 9Cr-NbMo and 9Cr-Ta, respectively. MX precipitates in 9Cr-Ta are (V,Ta)(C,N) that are distributed inside the matrix, while they are VN in 9Cr-NbMo that are distributed at the grain boundary. Both $Cr_{23}C_6$ and MX precipitates in 9Cr-NbMo are smaller but have

higher number density than 9Cr-Ta. In addition to the VN precipitates located at the grain boundary in 9Cr-NbMo, platelet VN precipitates were also observed, as shown by dark field imaging in Figure 12a inset. These platelet VN precipitates have a higher number density by two orders of magnitude compared to both the $Cr_{23}C_6$ and coarser VN precipitates in 9Cr-NbMo. Images of dislocations in both alloys were taken by the on-zone STEM method, as shown in Figure 12c and Figure 12d. The dislocation density of 9Cr-NbMo is higher than that of 9Cr-Ta.

Although the yield strength of both alloys is similar before the irradiation, the microstructures are different: 9Cr-Ta has smaller grain size, whereas 9Cr-NbMo has higher dislocation density and higher precipitate number density, indicating different strengthening contribution from these alloys.

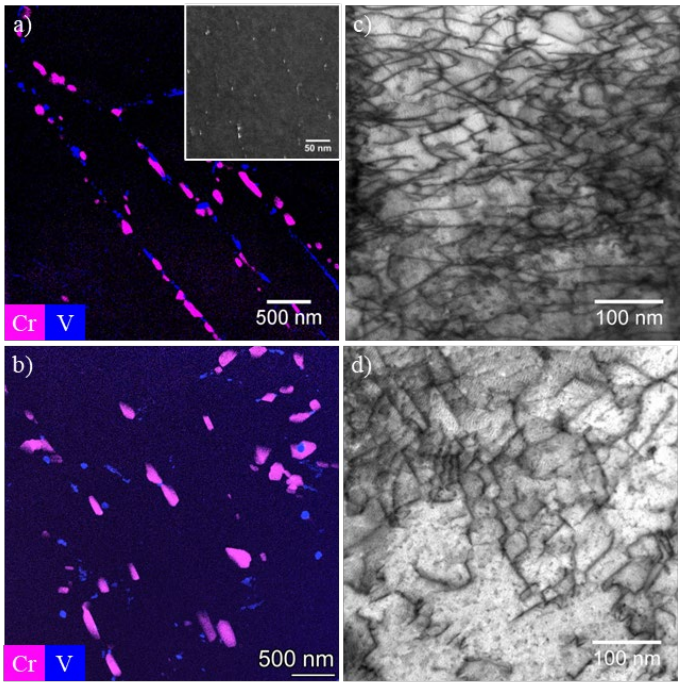

Figure 12. Precipitate and dislocation distributions in unirradiated (a,c) 9Cr-NbMo and (b,d) 9Cr-Ta.

Irradiation induced cavity and dislocation loops were observed in 9Cr-Ta, as reported in Ref. [1]. However, no dislocation loops were observed in the irradiated 9Cr-NbMo. Nanoscale cavities, on the other hand, are present in the irradiated 9Cr-NbMo. Figure 13 shows the cavity distributions in irradiated 9Cr-NbMo (a) for 7.4 dpa and (b) for 14.7 dpa. No obvious increase in cavity size was observed when the dose increased from 7.4 dpa to 14.7 dpa; the average cavity sizes are 1.5 ± 0.4 nm and 1.4 ± 0.3 nm, respectively. The calculated swelling in both samples is negligible using the formula of $\frac{1}{6}\pi N d^3$, with values on the order of 10^{-5} to 10^{-4}. The swelling of 9Cr-NbMo at 7.4 dpa is larger than that of 9Cr-Ta at the same irradiation condition [1].

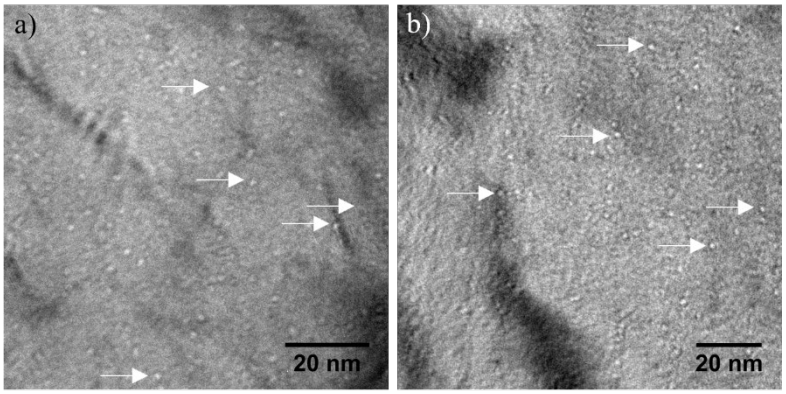

Figure 13. Cavities in 9Cr-NbMo irradiated to a dose of (a) 7.4 da at 490°C and (b) 14.7 dpa at 497°C. The images were taken using the under-focus technique. Examples of cavities are labeled with white arrows.

2.4.4 FUTURE RESEARCH

Post irradiation examination will be performed on the FM steels with TiC precipitates (i.e. castable nanostructured alloys).

2.4.5 REFERENCES

[1] L. Tan, W. Zhong, and T. Chen. Microstructural stability of tantalum-alloyed ferritic-martensitic steel with neutron irradiation to 7.4 dpa at~ 490 C. Materialia 9 (2020): 100608.

2.5 ADVANCED CASTABLE NANOSTRUCTURED ALLOYS (CNAs) FOR FIRST-WALL/BLANKET APPLICATIONS

Ying Yang, Weicheng Zhong, Tim Graening, Wei Tang, Yanli Wang, Xiang Chen, Bruce Pint, Marie Romedenne, Yutai Katoh*
**yangying@ornl.gov*

Supported by DOE-FES and ARPA-E

2.5.1 OBJECTIVE

The objective of this project is to establish a US-RAFM (reduced-activation ferritic-martensitic) steel based on the carbide-strengthened Castable Nanostructured Alloys (CNAs) and to demonstrate the viability and advantages of CNAs through the production and performance of industry-scale heats for use in integrated first-wall and blanket systems. This project is intended to establish or demonstrate a path toward technical feasibility for the fusion energy subsystem of integrated first-wall and blanket technologies, and improve the ease of maintainability, reduce regulatory risk, and increase environmental friendliness.

2.5.2 SUMMARY

In FY23, the project effort mainly focused on two activities. One is the procurement of 5-ton scale CNA heat and the other is to evaluate the properties of the 0.25-ton CNA rods. For the first activity, the 5-ton scale heat has completed the manufacturing steps of ingot melting, refining, forging, and rolling; now, it is waiting for the final heat treatment. For the second activity, the mechanical properties (tensile, charpy, creep), the welding performance, and the liquid coolant compatibility have been evaluated for the 0.25-ton heat.

2.5.3 PROGRESS AND STATUS

2.5.3.1 Procurement of 5-ton scale CNA heat

A 5-ton CNA ingot has been casted through vacuum induction melting and refined through vacuum arc refining at Saarchimiede Inc. The ingot was then subjected to hot forging and hot rolling, which leads to the plate form, as shown in Figure 14. The resulting chemistry and plate dimensions satisfactorily met the design specification. Before applying the final normalization and tempering, a few trial heat treatments were requested to make sure that the hardness and Charpy results meet the design specification. The preliminary results from trial heat treatment suggested a nonhomogeneous grain size in the plate. It is not clear if the non-homogeneity in grain size was due to the overshooting of tempering temperature leading to a partial austenization of microstructure. A piece of as-rolled material was requested and an in-house normalization and tempering will be performed at ORNL, followed by microstructural characterization. The final heat treatments will be instructed to Saarchimiede based on inhouse heat treatment results. Because of this, the final delivery of the 5-ton scale CNA plates is anticipated to be delayed until the Q2 of FY24.

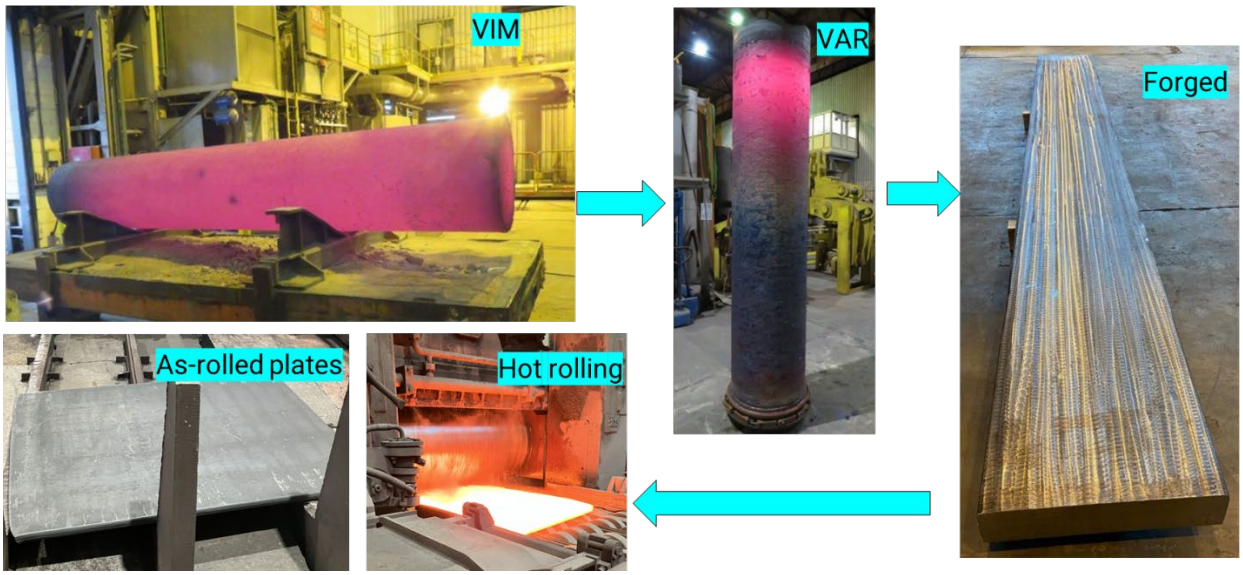

Figure 14: Production steps that have been completed for the 5-ton scale CNA plates

2.5.3.2 Evaluation of the 0.25-ton CNA rods

Mechanical behavior

The 0.25-ton heat of CNA rods have a hardness of HRC16 following normalization at 1050°C for 30 min and tempering at 750°C for 30 min. This is significantly lower than the design specification of HRC25±3. Therefore, these rods were subjected to additional heat treatments to meet the hardness requirements. A few trial heat treatments suggested that normalization at 1180°C for 10 min followed by tempering at 710°C for 30 min would bring the material in the right hardness range. The tensile, creep and DBTT properties of CNAs are shown in Figure 15. Because the in-house furnace has limited capability to heat treat the rods in one batch, they were heat treated in different batches, which caused some variations in mechanical behavior from batch to batch. In general, the CNA rods show lower strength and larger elongation than laboratory heats. The lower strength in CNA rod may also be contributed from different sizes of tensile specimen and different tensile frames. In laboratory heats, all tensile specimen are SSJ3 but in CNA rods, the specimen size follows the ASTM standards, which is much larger than the SSJ3 size. We tested the tensile property from the same heat-treated material and confirmed the ASTM specimen would result in lower yield and tensile strength. For creep test, the creep rupture life of the rods at 600 and 650°C tested in air is consistent with the trend observed for the laboratory heats. One specimen that was tested in inert gas atmosphere at 650°C and 90MPa showed longer creep rupture life than that of the laboratory CNA heats. Additional tests are currently ongoing to reproduce the test results. In summary, both tensile strength and creep rupture life of the 0.25-ton CNA rods are consistent or slightly worse than the laboratory heats but better than E97. For the Charpy impact test results, the CNA rods show a higher DBTT (~2°C) than laboratory heats and other RAFM steels (E97 and F82H). A possible reason for the elevated DBTT is due to the lower tempering temperature used in CNA rods, i.e., 710°C, which is lower than 750°C used for laboratory scale heat. To understand how tempering temperature affects the DBTT, selected rods were tempered at 750°C for 1 h, similar to the laboratory heats and other RAFMs. The higher tempering temperature reduced the DBTT by 14 degrees and increased the upper shelf energy by almost 100J. Careful microstructural characterization is currently ongoing to understand the underlying mechanism. Additional tensile and creep-rupture tests were also ongoing to see how the tempering temperature would affect these properties.

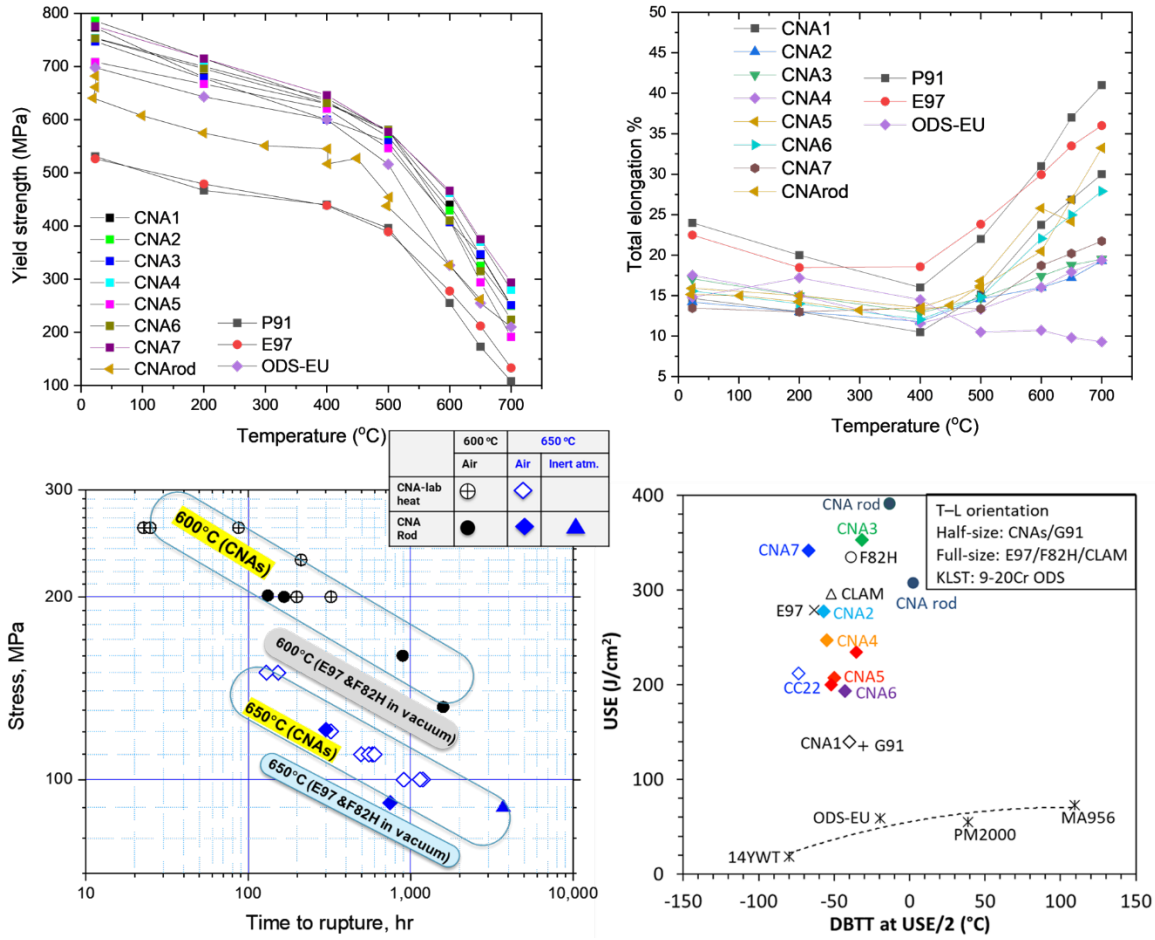

Figure 15: Tensile property, creep rupture life, DBTT and upper shelf energy of CNA rods compared to laboratory heats.

Welding performance

In FY23, a gas tungsten arc welding (GTAW) process for CNA plates using the CNA welding wire (produced from CNA rods) was developed and the microstructure and mechanical properties of the welded joint were evaluated in both the as-welded and post weld heat-treated conditions. The welded joint successfully passed the radiographic and dye penetration tests. Post weld heat treatments (PWHTs) that were the same as the final heat treatment of the CNA rods (normalization at 1170°C for 30min and tempering at 750°C for 1h) were applied to coupons removed from the welded joint. Optical and SEM microstructural characterization were performed on the weld zone and heat affected zone (HAZ). It was found that non-tempered martensite at the welded zone and over-tempered martensite at the heat affected zone led to non-uniform hardness distribution across the weldment. The uniform hardness distribution can be restored through PWHT. Transverse tensile tests were performed on welded joint specimens in the as welded and PWHT conditions. The specimen in the PWHT condition exhibited ~5% higher yield strength than the as-welded condition, and they all exhibited similar tensile strength as the CNA rods. The elongation and reduction of area (RoA) of the PWHT specimens resulted in an ~40% increase compared with the as welded condition. This improvement is believed to be caused by eliminating the strain

localization in HAZ through PWHT and the presence of non-tempered martensite. The results are summarized in Figure 16.

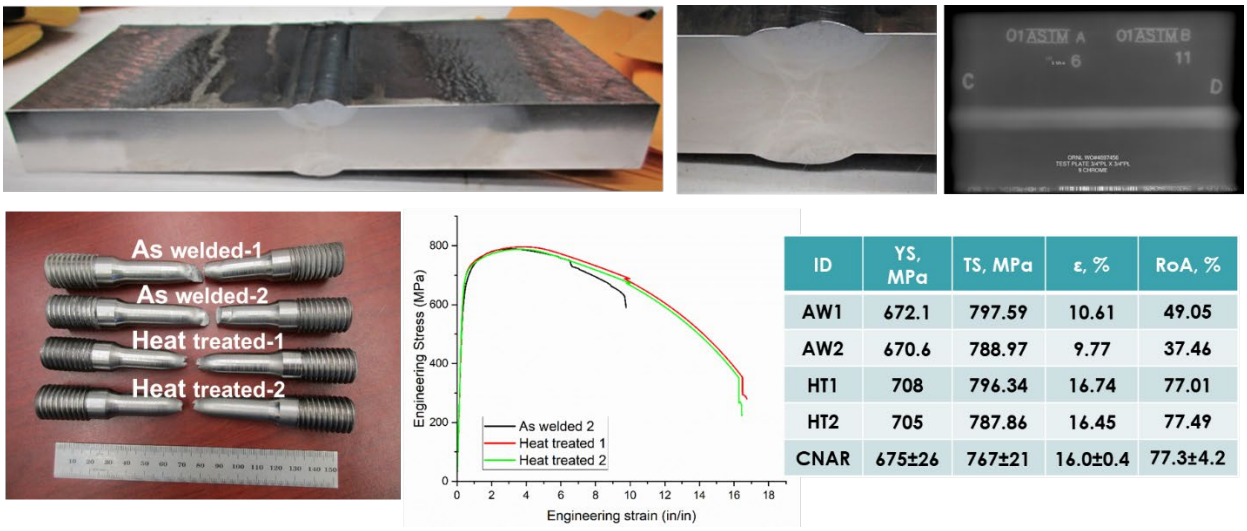

ID	YS, MPa	TS, MPa	ε, %	RoA, %
AW1	672.1	797.59	10.61	49.05
AW2	670.6	788.97	9.77	37.46
HT1	708	796.34	16.74	77.01
HT2	705	787.86	16.45	77.49
CNAR	675±26	767±21	16.0±0.4	77.3±4.2

Figure 16: A CNA welded joint made from the gas tungsten arc welding (GTAW) process and tensile test results of the as welded and PWHT conditions.

Pb-Li compatibility

Coupons of CNA rods were contained in specially designed capsules, and coolant compatibility test of these capsules was performed at 500, 600 and 700°C, respectively, for 1000 h in Pb-17at%Li coolant. E97 and F82H were tested at 600°C as well to serve as references. The results in Figure 17 show that the weight changes for all three materials are comparable at 600°C (within experimental uncertainty), suggesting similar performance of CNA to other RAFMs in Pb-17at%Li coolant. The results also show the weight loss increases with temperature. Similar coupons were cut from the weldment in as welded and PWHT conditions. These coupons were assembled into similar capsules and are currently undergoing coolant compatibility tests.

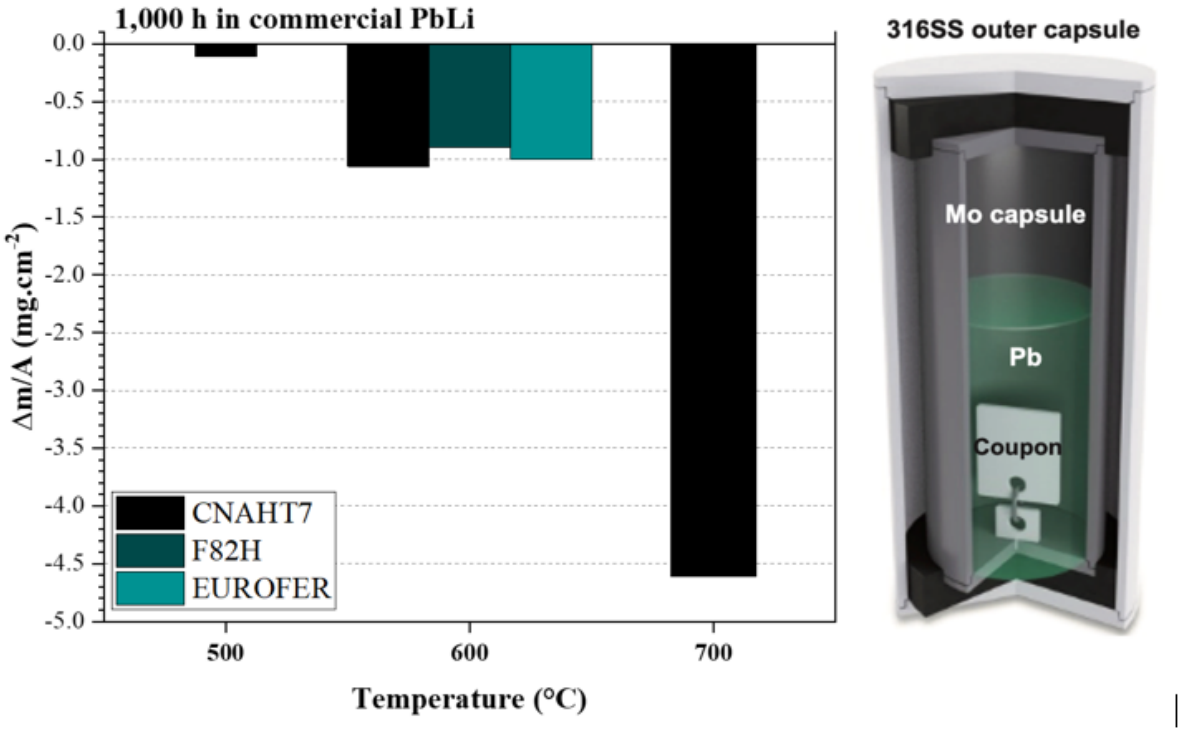

Figure 17: Testing capsules in Pb-Li coolant and the resulted weight loss at 500, 600 and 700°C, for 1000 h

2.5.4 FUTURE WORK

We anticipate receiving the 5-ton scale CNA plates in FY24 Q2. A comprehensive property evaluation on CNA plates will be performed and their properties will be compared with the refence materials of E97 and F82H.

2.6 MECHANICAL PROPERTIES OF LOW-COST ODS ALLOYS

T.S. Byun, D.A. Collins, K.L. Epps, D.T. Hoelzer*
**byunts@ornl.gov*

2.6.1 OBJECTIVE

This research is to develop an economically attractive processing route for oxide dispersion strengthened (ODS) alloys with little scale-up limitation. A variety of high-temperature thermomechanical cycles were applied to the simple mixtures of 14YWT alloy and oxide powders and the tensile properties of the newly produced ODS alloys were evaluated and used to downselect the processing route.

2.6.2 SUMMARY

This research attempts a solid-state ODS alloy processing approach consisting of powder mixture consolidation and a continuous thermomechanical activation process, both of which are based on the traditional metallurgical hot-working processes such as hot rolling, forging, and extrusion. Despite many scientific merits of the advanced oxide-dispersion strengthened (ODS) alloys, such as the nanostructured ferritic alloy (NFA) 14YWT, the only viable processing path for a high-quality product to date has been the mechanical alloying process [1]. This mechanical alloying is often a multi-day high-speed ball milling process of alloy powder with a small quantity of yttria (Y_2O_3) powder, followed by consolidation (typically by extrusion) to produce a solid product. To overcome such a practical hurdle in processing route and make a breakthrough advance in fusion materials technology, it is proposed to explore a new processing route that skips the mechanical alloying step and instead uses the continuous thermomechanical processing (CTMP) method. The CTMP method induces high-temperature severe plastic deformation (HT-SPD) [2] to achieve the effective distribution of oxide particles in a nanograin structure and thus desirable mechanical properties. A select combination of powder consolidation at 900°C and continuous thermomechanical activation (by 600°C CTMP) yielded both the nanograin structure and the nanoparticle distribution and thus a good combination of strength and ductility.

2.6.3 PROGRESS AND STATUS

2.6.3.1 Production and Characterization of ODS Alloys

This task aimed to produce nanostructured ODS alloys, i.e., the nanograined ferritic alloy structures with nanoparticle dispersion hardening, by effectively controlling the solid-state thermomechanical processing for oxide (oxygen source) dissolution, elemental diffusion, and grain refinement and enhance nanoscale clustering of oxygen and alloy elements with high oxygen affinity such as Ti and Y. That is, the CTMP process was designed to provide extreme metallurgical conditions to the solid materials, including very high internal stress, high densities of mobile dislocations, and thermal energy, under which oxide particles are fragmented and oxygen atoms can be dissolved from the source compound (an oxide) and diffused to the high oxygen-affinity elements. The first step of the ODS alloy production was a simple mixing of Fe-Cr base alloy powder and oxygen-source powder. The ODS materials were named HR1 through HR4 based on the combination of alloy powder and oxide powder. Each powder mixture was canned into a thick-wall (2.5 cm at minimum thickness portion) stainless steel container with a volume capacity of 0.17–0.25 L and sealed with a threaded plug. The second processing step was the consolidation of the powder mixture, during which hot-rolling cycles at 900°C or 1200°C were applied to the sealed containers of powder mixtures. The third step is a simple but controlled thermomechanical process comprising heating and hot-rolling cycles. It was assumed that an internal oxidation process at 500–900 °C for steels (< ~0.7 homologous temperature) can produce a high density of oxide nanoparticles in Fe-Cr steels, and therefore all TMP processes were performed in that temperature range. Table 4 describes the details of powder

mixtures, consolidation conditions, TMP conditions, and the total plasticity amounts applied by the hot-rolling process for powder consolidation and by the TMP cycles.

Table 4. Summary of base materials and processes for production of ferritic ODS alloys (T1/T2 = consolidation temperature/TMP temperature)

Materials ID	Powder Mixture (in wt.%)	Consolidation Process	Continuous TMP
HR1(T1/T2)	**14YWT alloy doped with Y & O**: Fe-14Cr-3W-0.4Ti-0.23Y-(0.07-0.14)O (no oxide powder)	Six hot-rolling cycles at 900 ºC for 80% plastic strain	Eight hot-rolling cycles at 600–900 ºC for 220–310% plastic strain
HR2(T1/T2)	**14YWT base+Fe_2O_3:** Fe-14Cr-3W-0.4Ti-(0.20-0.29)Y-(0.0140-0.02)O+0.22Fe_2O_3	Four to six hot-rolling cycles at 900 ºC or 1200 ºC for 60–80% plastic strain	Six to eight hot-rolling cycles at 500–900 ºC for 220–310% plastic strain
HR3(T1/T2)	**14YWT base+Y_2O_3:** Fe-14Cr-3W-0.4Ti-0.12Y-(0.011-0.024)O+0.3Y_2O_3	Six hot-rolling cycles at 900 ºC for 80% plastic strain	Eight hot-rolling cycles at 600–700 ºC for 240% plastic strain
HR4(T1/T2)	**Fe-10Cr base+Y_2O_3:** Fe-10Cr-1W-0.3Ti-0.2V+0.3Y_2O_3	Four to six hot-rolling cycles at 900 ºC or 1200 ºC for 60–80% plastic strain	Six to eight hot-rolling cycles at 500–600 ºC for 220–270% plastic strain

Room-temperature tensile testing was performed for all of the newly produced ODS alloys, and the tensile property data such as the strength and ductility parameters were used as criteria for downselecting the processing routes and further characterization. Further characterization, including high temperature tensile testing up to 700 ºC and microstructure analysis, was performed for a selected set of materials only. The SS-J2 specimens have a nominal gage section of 5 × 1.2 × 0.5 mm, all of which were in the rolling direction of TMPs.

2.6.3.2 Mechanical Properties

Demonstrating a high strength level over a range from room to tentative operation temperature is essential to the fusion reactor application of an ODS alloy. That is, to favorably replace the traditional quenched and tempered ferritic-martensitic (FM) steels which show limitations in high-temperature (> ~500ºC) strength and creep resistance, the candidate ODS alloy should demonstrate both yield and ultimate strengths significantly higher than those steels. Figure 18 compares the yield strength (YS) and ultimate tensile strength (UTS) of the newly produced ODS alloys via various CTMPs. It is first noted that the final TMP temperature, i.e., the hot-rolling temperature is the most influential parameter to determine the strength of the product. The ODS alloys SPD processed at the highest temperature of 900ºC generally show relatively lower strengths that are similar to those of traditional FM steels (i.e., ~400 MPa for YS and ~600 MPa for UTS). The CTMPs processed at lower temperatures demonstrate higher strengths. The higher consolidation temperature, 1200ºC, resulted in generally lower strengths regardless of the base materials. This might be due to the over-coarsened grains and particles during the repeated hot-rolling at such a high temperature. The consolidation temperature needs to be lower; the 900ºC process resulted in satisfactory strengths. It is noted that this coincides with the optimized consolidation (extrusion) temperature range (800–850 °C) for the mechanically alloyed 14YWT NFAs [1].

The HR2 and HR3 materials processed by 900°C consolidation and 600°C continuous TMP demonstrate high enough strengths: YS > 800 MPa and UTS > 1 GPa. These strength values are nearly twice those of the traditional FM steels and can be accepted as the desirable strength level of an ODS alloy aiming at high temperature fusion reactor application. The pre-alloyed (HR1) material shows high strengths regardless of processing route but cannot reach those of the HR2 and HR3 alloys after the same processing. In these cases, the oxide forming elements Ti and Y might have been overly segregated at some preferred sites such

as grain boundaries during the gas atomization of the Y/O-alloyed 14YWT. The tensile strength data indicate that further TMP steps could not reverse the segregation. Finally, the Fe-9Cr based HR4 material shows similar strength as the HR1 alloy if compared at the same CTMP conditions.

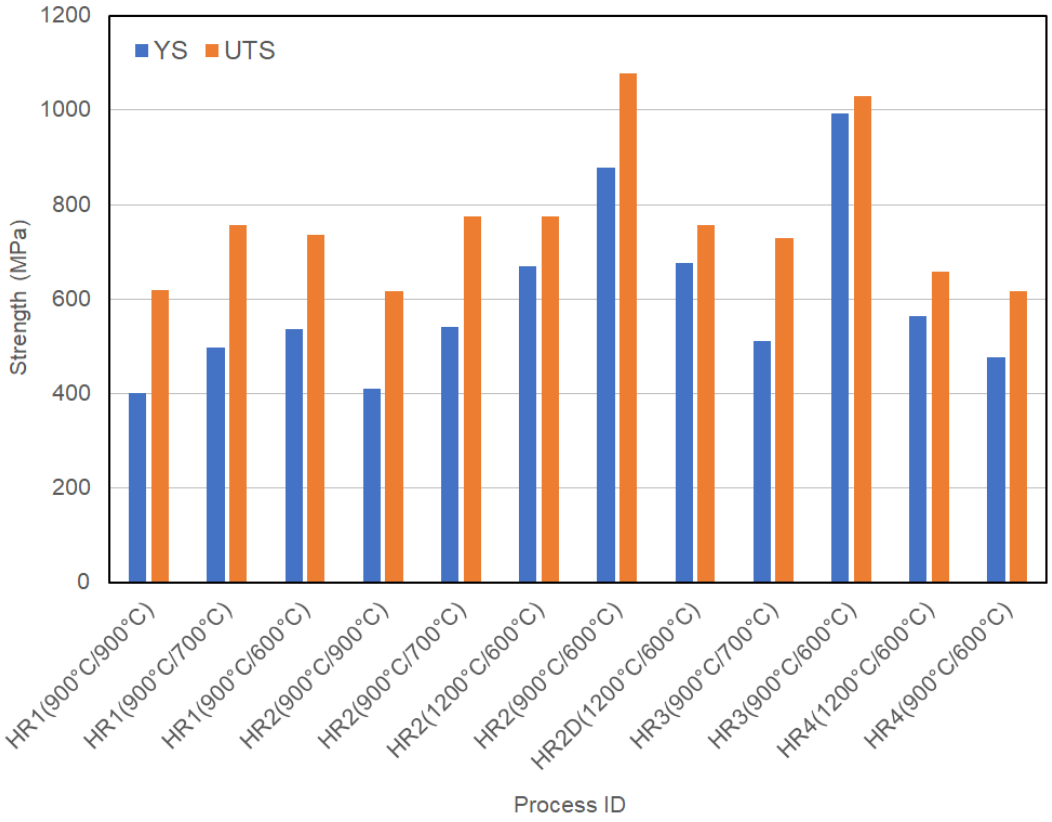

Figure 18. Comparison of strengths for the four alloys after various consolidation/CTMP processes

Figure 19 displays the uniform and total elongation data (UE and TE) for the four alloys. Except for the highest temperature consolidation/lowest temperature SPD combination, relatively high ductilities were measured for their high strengths. In particular, the HR1(900ºC/900ºC) alloy demonstrates outstandingly high UE and TE (~25% and ~33%) although its strength is in the same range of traditional FM steels. It is a highly positive result that no embrittled or near-embrittled materials are produced by any of the processes tested. This might indicate that the simply-repeated application of traditional TMT can efficiently weld the alloy/oxide powder particles while creating high strength microstructures. It is notable that both the highest strength HR2 and HR3 alloys processed in the (900ºC/600ºC) condition demonstrate significant ductility or UE and TE > 5%. Since only those two alloys are considered to satisfy the criteria for advanced ODS alloys (e.g., YS > 800 MPa, UTS > 1 GPa, TE > 5%), they are downselected for further characterization.

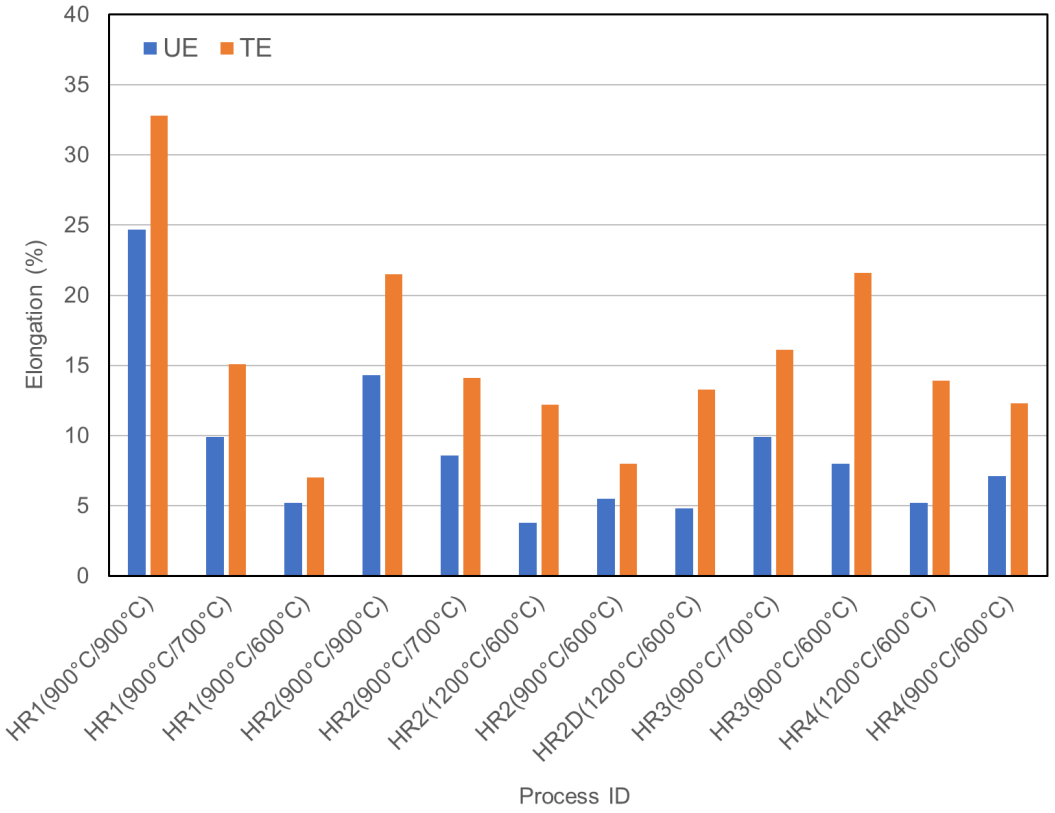

Figure 19. Comparison of ductilities for the four alloys after consolidation/CTMP processes

The strength data of the select two alloys HR2 and HR3 are compiled in the YS versus test temperature plots in Figure 20. As observed in many other FM steels and ferritic ODS alloys, the strengths of these ferritic ODS alloys are relatively high at room temperature and decrease at different rates with increasing test temperature. It is observed that the highest strength ODS alloys–the HR2(900°C/600°C) and HR3(900°C/600°C) alloys showing high room temperature strengths of YS > 800 MPa and UTS > 1 GPa–can maintain their strengths quite well above 550 MPa up to 500°C but the decrease of strength accelerates above 500°C. The other HR2 and HR3 materials show much lower room temperature strengths when compared to the strongest materials. The overall strength differences among the materials, however, become less significant at the highest test temperature of 700°C. At this highest test temperature, the HR3(900°C/600°C) alloy retains the highest strength among all the ODS alloys tested. This may be because the yttrium oxide supply is more effective in creating a more stable high-temperature microstructure compared to the addition of iron oxide to form the initial powder mixture (in HR2).

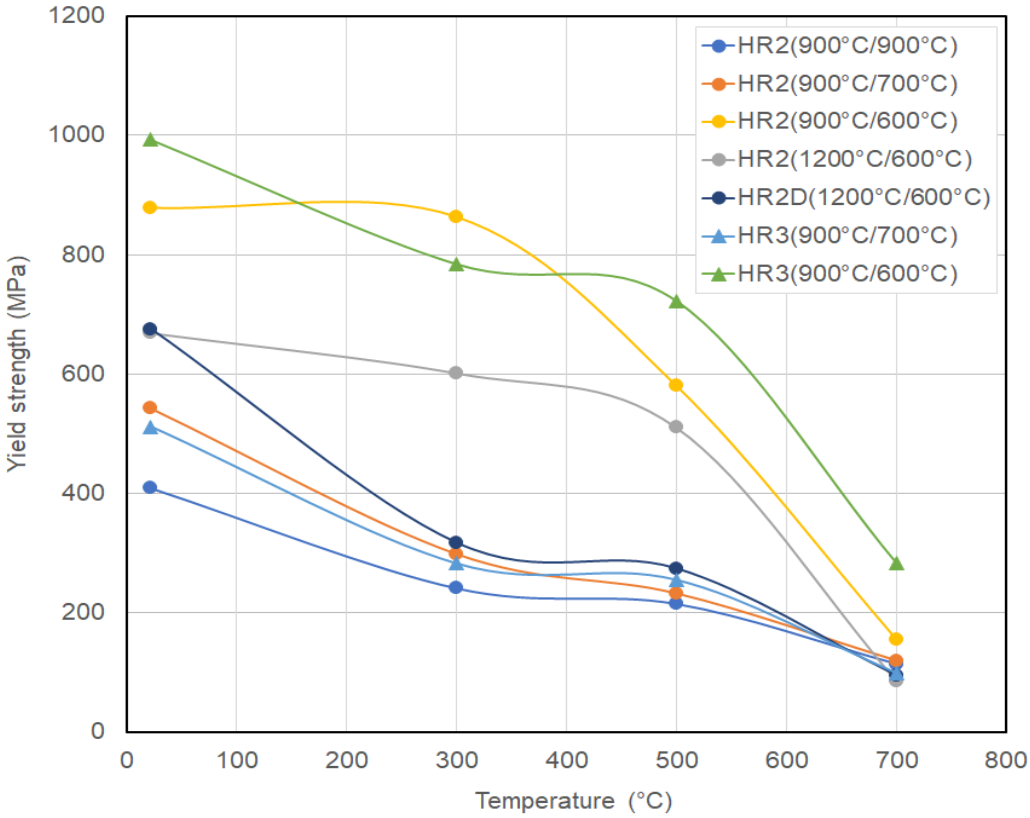

Figure 20. Temperature dependence of YS in the HR2 and HR3 alloys

The temperature dependence of ductility, i.e., the total elongation (TE) versus test temperature plots, is summarized in Figure 21. In contrast to the relatively monotonic temperature dependence of YS, the ductility parameters show rather complex temperature dependencies that are affected by the processing route and hence on the strength of the materials, as well some unique micromechanisms in ferritic steels, such as dynamic strain aging. In general, the rankings of room temperature strength parameters are approximately reversed in the ductility parameters, and their temperature dependence curves form either a monotonically decreasing line (for the HR2(900ºC/900ºC only) or a curve with minimum over the test temperature range. Except for the lowest ductility case HR2(900ºC/900ºC), all processing routes attempted in this study resulted in at least 3% TE and the vast majority in more than 10% TE.

As implied in the rapid reduction of strength in the temperature above ~500 ºC, the total ductility increases significantly between 500ºC and 700ºC. Notably, the TE values at the highest test temperature of 700°C are higher than those at RT, with all TE data contained in the high ductility range > 20%.

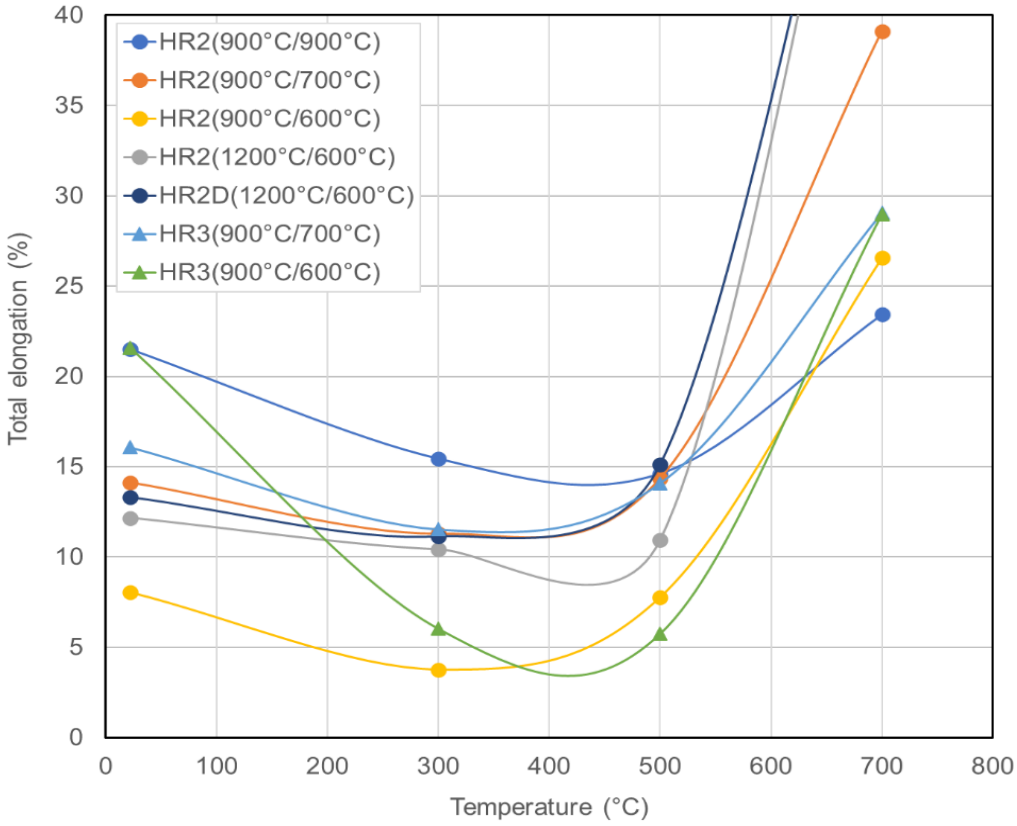

Figure 21. Temperature dependence of TE in the HR2 and HR3 alloys

2.6.3.3 Concluding Remarks

As a new approach to develop a low-cost processing method for production of ODS alloys, we explored an ODS steel processing method that does not include mechanical alloying but rather uses traditional thermomechanical processing (TMP) only, which is to use the effect of high-temperature severe plastic deformation (HT-SPD). It is a notable finding that the HR2 and HR3 alloys processed in the (900°C/600°C) condition can demonstrate both high strength (YS > 800 MPa, UTS > 1 GPa) and significant ductility (UE and TE > 5%). Since only those two alloys are considered to satisfy the criteria for advanced ODS alloys (UTS > 1 GPa, TE > 5%), they were downselected and further characterized.

2.6.4 FUTURE RESEARCH

The downselected processing route will be applied to create novel microstructures with oxide-carbide hybrid strengthening to achieve further improved mechanical properties over a wide temperature range. Mechanical testing and high-resolution microscopy will be continued for the select ODS alloys with proper high strength and ductility.

2.6.5 REFERENCES

[1] D.T. Hoelzer. History and outlook of ODS/NFA ferritic alloys for nuclear applications. Trans. American Nuclear Society, 118 (2018) 1587-1590.

[2] K. Edalati et al. Nanomaterials by severe plastic deformation: review of historical developments and recent advances. Mater. Res. Lett. 10 (2022) 163-256

2.7 MICROSTRUCTURAL CHARACTERISTICS OF LOW-COST ODS ALLOYS

T.S. Byun, T.G. Lach, Y. Lin*
**byunts@ornl.gov*

2.7.1 OBJECTIVE

This research is to develop an economically attractive, technically feasible processing route for oxide dispersion strengthened (ODS) ferritic alloys for fusion reactor applications. The ODS alloys produced via the new continuous thermomechanical processing (CTMP) methods were downselected by mechanical properties to analyze detailed microstructures and to pursue further development.

2.7.2 SUMMARY

To overcome the practical hurdles in the ODS steel production method based on the high-power mechanical alloying, we pursued a solid-state ODS alloy processing approach consisting of the continuous thermomechanical processing (CTMP) method only. A combination of powder consolidation process at 900°C and continuous thermomechanical processing at 600°C yielded both a nanograin structure and a nanoparticle distribution and thus a good combination of strength and ductility. This report summarizes the results of microstructure analysis on the 14YWT alloy based ODS alloy processed by the downselected processing routes.

2.7.3 PROGRESS AND STATUS

2.7.3.1 Processing and Characterization of ODS Alloys

The ODS ferritic alloys that have been processed through the solid-state thermomechanical processing and have delivered desirable mechanical properties were downselected for further microstructural analysis. Table 5 describes the details of powder mixtures, consolidation conditions, CTMP conditions, and the total plasticity amounts applied by the hot-rolling steps for powder consolidation and CTMP.

Table 5. Summary of base materials and select processes for production of ODS ferritic alloys

Materials ID	Powder Mixture (in wt.%)	Consolidation Process	Continuous TMP
HR1(900ºC/600ºC)	**14YWT alloy doped with Y & O**: Fe-14Cr-3W-0.4Ti-0.23Y-(0.07-0.14)O (no oxide powder)	Six hot-rolling cycles at 900 ºC for 80% plastic strain	Eight hot-rolling cycles at 600 ºC for 220–310% plastic strain
HR2(900ºC/600ºC)	**14YWT base+Fe_2O_3:** Fe-14Cr-3W-0.4Ti-(0.20-0.29)Y-(0.0140-0.02)O+0.22Fe_2O_3	Four to six hot-rolling cycles at 900 ºC for 80% plastic strain	Six to eight hot-rolling cycles at 600 ºC for 220–310% plastic strain
HR3(900ºC/600ºC)	**14YWT base+Y_2O_3:** Fe-14Cr-3W-0.4Ti-0.12Y-(0.011-0.024)O+0.3Y_2O_3	Six hot-rolling cycles at 900 ºC for 80% plastic strain	Eight hot-rolling cycles at 600 ºC for 240% plastic strain

Microstructural analysis was performed for the newly produced ODS alloys by using a TESCAN MIRA3 SEM equipped with an Oxford Instruments electron backscatter diffraction (EBSD) detector and an FEI Talos 200 keV scanning transmission electron microscope (STEM) equipped with a X-field emission gun high-brightness source, bright field (BF) and multiple annular dark field detectors, and a quadrupole FEI ChemiSTEM energy dispersion x-ray spectroscopy collection system. The EBSD images–the colored inverse pole figure (IPF) maps–for grain structures and high-resolution BF images that show subgrain and dislocation structures were obtained from the SEM and STEM equipment, respectively.

2.7.3.2 Grain Structure and Particle Distribution

The SEM-EBSD images (IPF maps) for the four 14YWT based ODS alloys–the HR1, HR2, HR3 alloys in the (900ºC/600ºC) condition, and the reference (mechanical alloying based) 14YWT [1]–are presented in Figure 22, in which all EBSD images demonstrate very fine grain structures. The IPF maps of the HR1 and HR2 alloys show strong textures with [001] and [111] orientations and large grain conglomerations containing large numbers of similar grain orientations. In these images many nanograins are observed while some of the grains are relatively coarser, as large as a few micrometers. Since the grains with similar orientations and the resolution limit of EBSD imaging cannot reveal all grain boundaries, the real nanograin features in an ODS alloy can be revealed by a higher resolution TEM image.

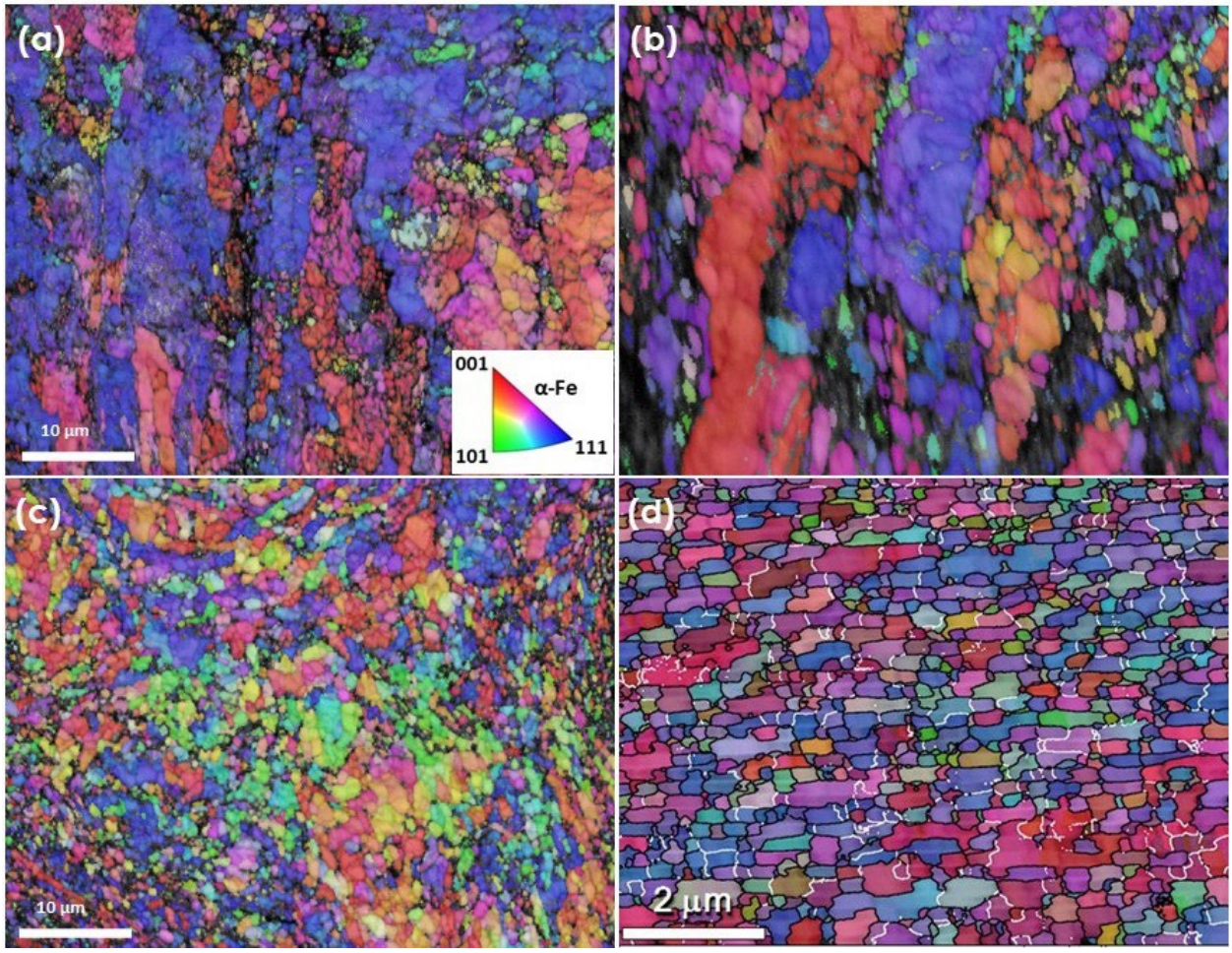

Figure 22. EBSD images showing grain size and orientation distributions in ODS alloys (a) HR1, (b) HR2, (c) HR3 in the (900ºC/600ºC) condition, and (d) reference 14YWT produced via mechanical alloying.

Figure 23 shows a TEM bright field (BF) image from the newly produced ODS alloy HR2 (900ºC/600ºC) showing such a nanograin structure and the Ti map showing a high-density distribution of particles in the same area. The BF image (left) shows that the average interception length is less than 200 nm across the elongated grain width and 400–500 nm along the grain-elongation (hot-rolling) direction. In addition, the Ti energy dispersive X-ray spectroscopy (EDS) map (right) indicates that a high density of nanosized Ti-enriched particles are broadly distributed after the TMP method. Further, along with the larger particles,

very small Ti-rich particles are observed in the form of small dense particle 'clouds'. Indeed, the number density of Ti-rich particles is considered to be high, and the small and large Ti-enriched oxide and carbide particles are believed to provide very high resistance to the high-temperature deformation. It is also noted that the Ti distribution is inhomogeneous as we observe some areas with little Ti content next to the 'cloud'-like areas with both numerous fine and coarse particles. Some Ti distribution patterns also coincide with the grain structure features in the BF image, which indicates the Ti atoms distribute preferentially in grain or subgrain boundary areas.

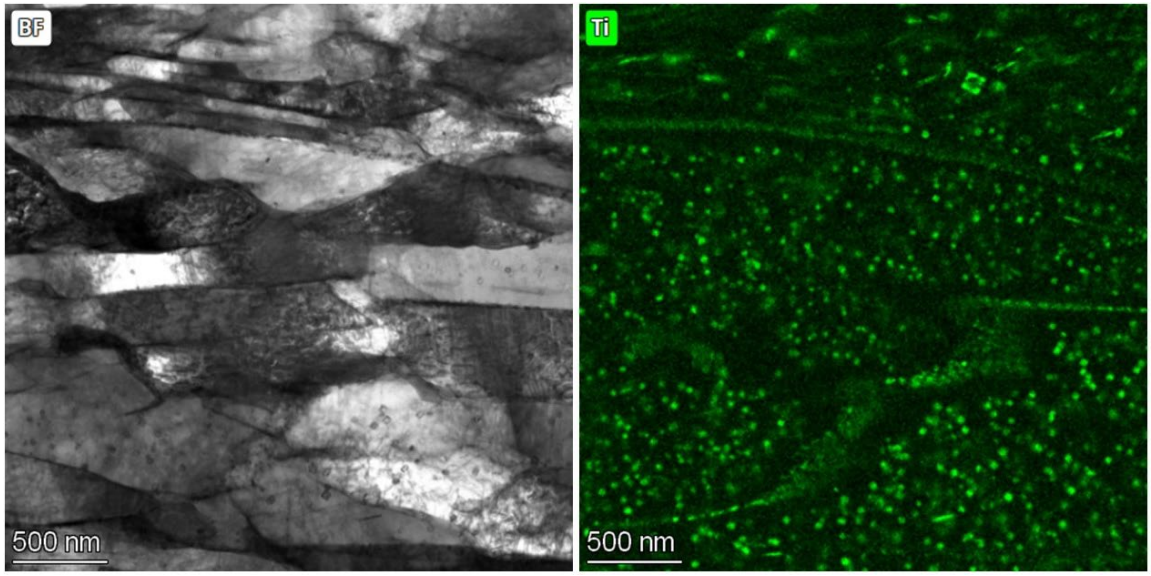

Figure 23. Bright field (BF) image from a HR2 (900ºC/600ºC) alloy showing a nanograin structure and Ti map showing a high-density particle distribution

Elemental maps obtained for a polycrystalline area of HR2(900ºC/600ºC) using STEM are collected and displayed in Figure 24. In the multigrain area (seen as the BF image) the TiY-rich oxide particles and TiWV-rich carbide particles coexist in a mixed distribution. Many of the W-rich particles coincide with the Ti-rich carbides, which indicates TiW carbides: the V distribution is relatively weak in these particles and sometimes W (or possibly W-C) tends to distribute on the surface of Ti-rich carbides or separately from the other carbides or oxides. Comparing the carbon and oxygen maps, indeed, many of their distribution areas (i.e., particles) are not overlapping, which might indicate that the carbide and oxide particles are formed separately. It is also observed that some elements such as W and Ti are enriched in both large carbide and large oxide particles, which might be because both elements have strong affinities with the carbon and oxygen atoms.

Some additional findings from the STEM analysis are summarized as the unique characteristics of the HR2 ODS alloy: the nanograin structure produced via the low-cost processing using CTMP only has a grain size range of ~100–500 nm and it is a semi-annealed structure with a high density of dislocations. The elemental maps show residual element segregation at some features like grain boundaries and precipitates along grain boundaries. Carbides are formed both in the matrix and at grain boundaries and often have relatively high aspect ratios (or elongated shapes). In the observation, the majority of carbides are within the size range of ~10–50 nm while the oxide particles are smaller (> ~5 nm). Much larger (e.g.,~80 nm) oxide and carbide particles are also observed, which are considered to be fragmented from the pre-existing particles but not completely dissolved during thermomechanical processing. Finally, the total density of oxide and carbide particles is estimated to be at least an order of magnitude lower than that of the well-developed 14YWT (i.e., $< 10^{23}$ m^{-3}). Additional samples need to be examined to obtain more accurate particle density data.

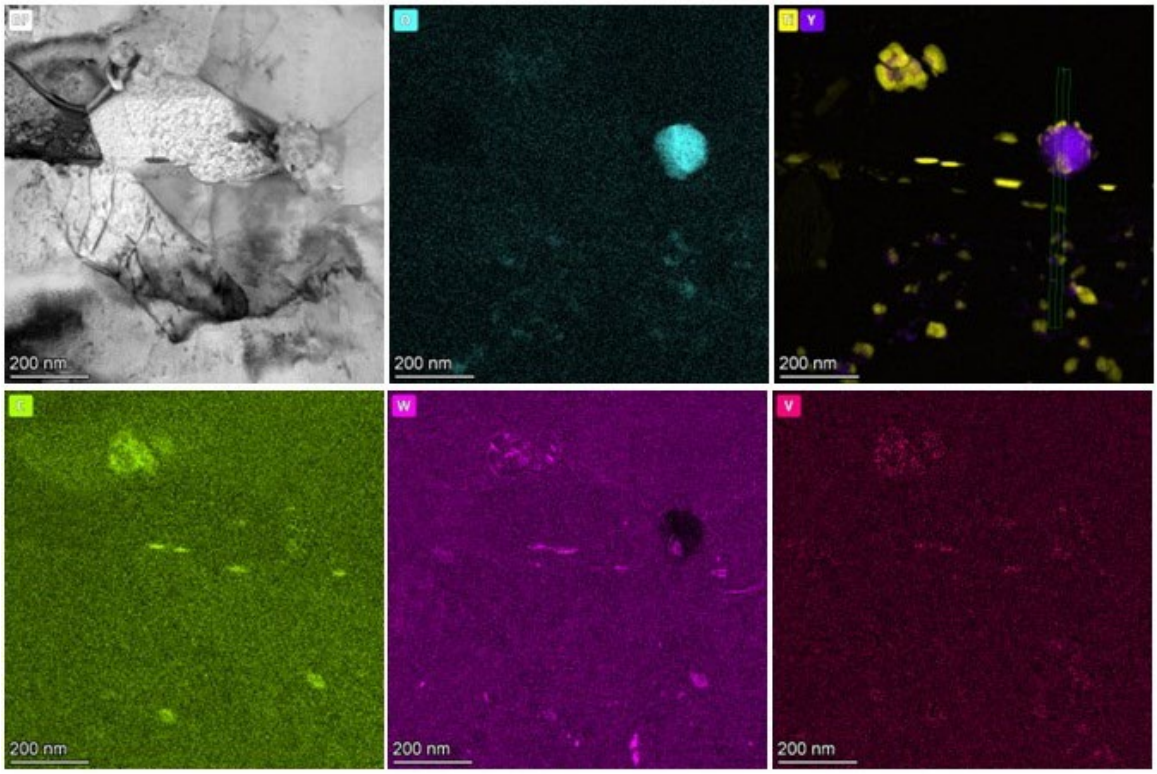

Figure 24. Mixture of TiY-rich oxide (top) and TiWV-rich carbide (bottom) particles in the multigrain area (BF image in the top left image)

2.7.3.3 Concluding Remarks

The select TMP only approach to develop a low-cost production route for ODS demonstrated a good combination of high strength (YS > 800 MPa, UTS > 1 GPa) and significant ductility (UE and TE > 5%). The result of microstructural analysis also confirmed that both a nanocrystalline structure and a distribution of nanoparticles (includes both oxides and carbides) were created in those ODS alloys by the continuous TMP method.

2.7.4 FUTURE RESEARCH

The downselected processing route will be applied to create novel microstructures with oxide-carbide hybrid strengthening to achieve further improved mechanical properties over a wide temperature range. Mechanical testing and high-resolution microscopy will be continued for the newly produced ODS alloys that are downselected with high strength and ductility data.

2.7.5 REFERENCES

[1] D.T. Hoelzer. History and outlook of ODS/NFA ferritic alloys for nuclear applications. Trans. American Nuclear Society, 118 (2018) 1587-1590.

3. CERAMIC AND COMPOSITE MATERIALS

3.1 THE RESPONSE OF B-11 ENRICHED ZrB_2 ULTRA-HIGH TEMPERATURE CERAMIC TO NEUTRON IRRADIATION AT ELEVATED TEMPERATURES

Y. Lin, T. Koyanagi, D.J. Sprouster (Stony Brook University),C.M. Petrie, Y. Katoh,*
W. Fahrenholtz (Missouri University of Science and Technology), G.E. Hilmas (Missouri University of Science and Technology)
**liny@ornl.gov*

3.1.1 OBJECTIVE

This study comprehensively investigates neutron-induced property changes in B-11 enriched ZrB_2, an ultra-high temperature ceramic (UHTC). The research aims to understand and quantify the effects of neutron irradiation on the microstructure, volume change, and thermal diffusivity of ZrB_2, which is particularly crucial for assessing its viability in plasma-facing materials for fusion reactor applications.

3.1.2 SUMMARY

ZrB_2 is a candidate material for fusion reactor plasma-facing applications due to its high-temperature durability, yet its response to neutron irradiation is not fully understood. The transformation of B-10 to helium poses a risk of swelling and cracking [1]. We used advanced TEM and synchrotron XRD to study how B-11 enriched (99.37 wt.%) ZrB_2 changes under mixed-spectrum neutron irradiation. At 220°C and 620°C in HFIR, the neutron fluence of 2.2×10^{25} neutrons/m^2 (E > 0.1 MeV) reduced thermal diffusivity by 5-10 times. Samples irradiated at 620°C showed cavities, while those irradiated at 220°C did not, and the 620°C samples had fewer microcracks than the 220°C ones. X-ray diffraction indicated lattice expansion along the *a*-axis and shrinkage along the *c*-axis post-irradiation. The prevalence of dislocation loops on prism planes suggests *a*-axis lattice swelling, a primary contributor to grain boundary microcracking that decreases with higher irradiation temperatures. ZrB_2's prism planar defects and a > c lattice swelling, uncommon for hexagonal ceramics, might relate to its lower c/a ratio of 1.12. The formation of cavities in the samples irradiated at 620°C likely originates from helium production resulting from residual B-10 transmutation, even at a lower irradiation temperature than the anticipated vacancy mobility temperature (~1100°C), which is approximately one-third of the melting temperature.

3.1.3 PROGRESS AND STATUS

As part of the ongoing investigation into UHTCs, with a particular focus on ZrB_2 as a potential candidate material for high-heat and plasma-facing applications within fusion reactors, significant progress has been made. The compound exhibits promising properties for these applications; however, its response to neutron/ion irradiation, especially concerning potential swelling and crack formation due to He accumulation from residual B-10 transmutation [1], remains a subject of limited understanding. To mitigate these concerns, the study incorporated the production of isotopically-enriched B-11 ZrB_2 samples specifically designed for neutron irradiation testing. These samples were enriched with 99.37 wt.% in B-11, contributing to a 17.9 wt.% concentration of Boron within the samples. Subsequently, the samples were subjected to neutron irradiation at intended temperatures of 220°C and 620°C.

Insights gleaned from the irradiation studies, analyzed using a variety of techniques, offered a nuanced perspective on the microstructural changes post-irradiation. Transmission electron microscopy (TEM) analysis revealed the presence of irradiation-induced defects, specifically dislocation loops and networks, with variations in size and density at different irradiation temperatures. The investigation further uncovered a homogeneous distribution of cavities within ZrB_2 samples irradiated at 620°C, in contrast to samples

irradiated at 220°C, which did not exhibit such cavity formations (Figure 25). These cavities displayed bimodal characteristics in size, indicative of transmutant He gas atoms, with larger faceted cavities showing a typical elongation along the 100 projected direction, while smaller ones appeared spherical.

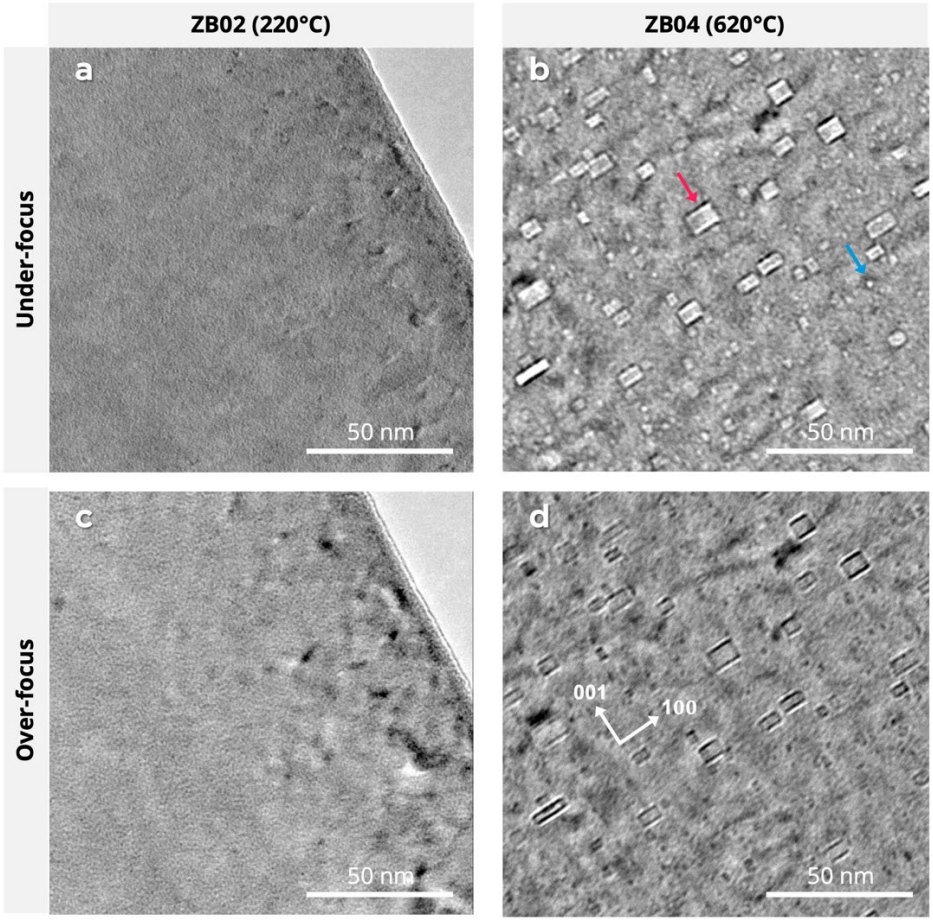

Figure 25. TEM bright field images showing cavities in neutron-irradiated ZrB2 at 220°C and 620°C, at 3.9 dpa and a total helium content of 4200 appm. The red arrow indicates larger faceted cavities, while the blue arrow indicates smaller spherical cavities.

Additionally, observations through scanning electron microscopy (SEM) and synchrotron X-ray diffraction were instrumental in studying surface crack formations and lattice parameter changes. As shown in Figure 26, lattice expansions and contractions along the "a" and "c" axes were detected in samples irradiated at 220°C and 620°C. These findings were consistent with the discoveries of dislocation loops and other microstructural modifications. In addition, irradiation-induced amorphization was not observed at the low irradiation temperature of ~220°C. An important observation from the investigations was the significance of grain boundary microcracks contributing to the volumetric swelling in neutron-irradiated ZrB_2. This suggests potential applications for this material but highlights the necessity for further studies on vacancy and interstitial diffusivity to determine operational temperature ranges for nuclear applications.

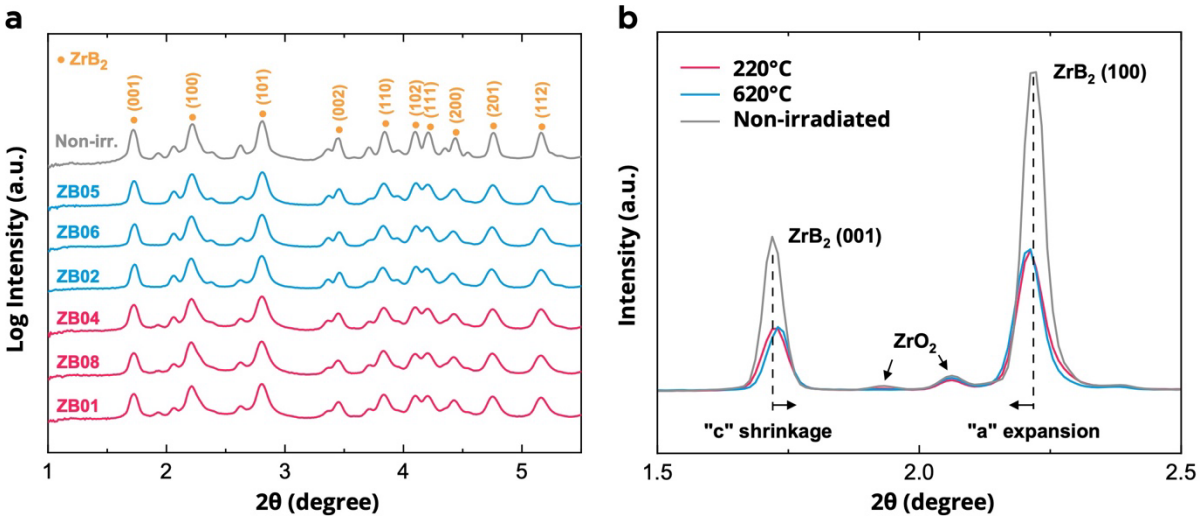

Figure 26. Synchrotron-based X-ray diffraction patterns of neutron irradiated ZrB_2 at 220°C (ZB01, ZB04, ZB08) and 620°C (ZB02, ZB05, ZB06).

3.1.4 FUTURE RESEARCH

A manuscript detailing the current study on neutron-irradiated ZrB_2 is currently in progress and will be submitted to a peer-reviewed journal. Future works will concentrate on post-irradiation examination on ZrB_2 and TiB_2 materials at elevated doses (3-5 HFIR cycles) and higher nominal irradiation temperatures (>1000°C).

3.1.5 REFERENCES

[1] E.U. Grinik, V. V Ogorodnikov, A.G. Krainy, Fracturing of borides under neutron irradiation, J. Nucl. Mater. 233–237 (1996) 1349–1354.

3.2 CORROSION CHARACTERISTICS OF SiC MATERIALS IN BERYLLIUM-BEARING MOLTEN FLUORIDE SALT

T. Koyanagi, J. Lee, J. Keiser, H. Gietl, Y. Katoh*
**koyanagit@ornl.gov*

3.2.1 OBJECTIVE

To understand the chemical compatibility of SiC in beryllium-bearing molten salt for potential fusion blanket applications, this study investigated the corrosion behavior of grades of high-purity monolithic SiC in purified 2LiF-BeF_2 (FLiBe) at 750°C for 500 and 1000 h.

3.2.2 SUMMARY

Chemical vapor deposited SiC single crystals and polycrystals were exposed to a static beryllium-bearing molten fluoride salt, FLiBe, for 500 and 1000 h at 750°C. Overall, the single crystal and polycrystalline SiC materials experienced slight weight loss and nominal surface etching regardless of the material type. Localized pitting and nonuniform Si removal from surface regions were associated with trace metal impurities and oxygen. Cross-sectional observation revealed minimal subsurface changes in the microstructure. The corrosion damage processes were similar to those reported for molten LiF–KF–NaF salt with trace impurities, indicating that the impurities significantly affect SiC corrosion.

The details of the experiment and analysis are reported in Corrosion Science Volume 220, (2023) 111301.

3.2.3 PROGRESS AND STATUS

After the corrosion test at 750 °C for 1000 h, the Rohm and Haas grade SiC specimens had lost only 0.26 mg/cm^2, which can be explained by removal of Si from the material; the mass loss corresponds to a formation of 5.5 μm deep C-rich phase with a 50% area fraction, assuming a density of the C-rich phase equal to the theoretical density of graphite (2.26 g/cm^3). The calculated depth of the C-rich phase is comparable with that from the observations of the cross sections. The mass loss of SiC is much smaller than that of alloy specimens tested using the same grades of FLiBe salt and the same capsule material. For example, the mass losses were 0.6 mg/cm^2 for Hastelloy N and 1.9–3.5 mg/cm^2 for 316H stainless steel following testing at 750°C for 1000 h using the same method and salt as those used in this work. The other SiC specimens also experienced marginal mass loss of 0.08–0.24 mg/cm^2 after the 500 h exposure. Therefore, the SiC materials show great potential for use in future molten-salt reactors. The results of this study encourage further investigations of SiC's chemical compatibility with FLiBe because SiC's corrosion behavior in the operating reactor environment will likely be different from that in the Mo capsule.

Regardless of the material type, C-rich phases were observed to form on the surface and in shallow pits (Figure 27). The pit formation and the removal of Si from the SiC materials are consistent with the mass loss after the corrosion tests. The C-rich regions accompanied O and metallic impurities. Because of the hygroscopic nature of FLiBe, O tends to be a persistent contaminant expected in a trace quantity. The metallic impurity effects in this study were unintentional, but impurities were likely sourced from the Mo capsule and potentially from the experiment preparation processes. Regarding the impurities detected, transition metals, including Cr, Ni and Fe, are expected to be present in the reactor salt because they comprise most of the core volume (e.g., 316H stainless steel proposed for the reactor vessel).

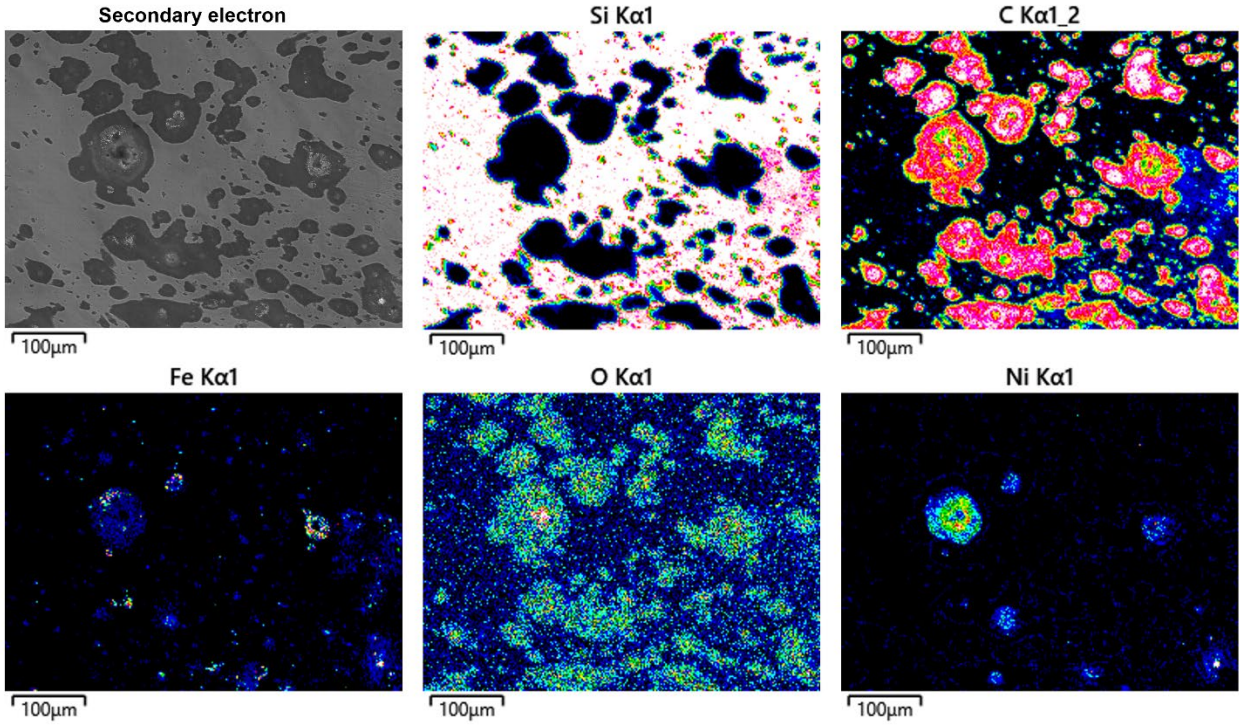

Figure 27. Energy dispersive X-ray spectroscopy maps of pitting corrosion of Rohm and Haas grade chemical vapor deposited SiC surface exposed to FLiBe salt at 750°C for 500 h.

3.2.4 FUTURE RESEARCH

Investigating the corrosion resistance in more aggressive and reactor-relevant corrosion environments (e.g., corrosion in flowing salt) requires further research. Additionally, a corrosion test capsule made of ultrahigh-purity SiC or carbon material is recommended for better control of the corrosion environment.

4. HIGH HEAT FLUX AND PLASMA FACING MATERIALS

4.1 PRECIPITATE FORMATION OF K-DOPED TUNGSTEN UNDER HFIR IRRADIAION

W. Zhong, T. Koyanagi*
**zhongw@ornl.gov*

4.1.1 OBJECTIVE

K-doped tungsten was irradiated in High Flux Isotope Reactor (HFIR). The objective of this work is to investigate the neutron irradiation effects on the microstructure of K-doped W. The characterization on the irradiation induced precipitates is presented in this report. The results of this work will be used to identify the hydrogen trapping sites in irradiated K-doped tungsten.

4.1.2 SUMMARY

K-doped tungsten samples were irradiated in HFIR to 0.47 dpa at a nominal temperature of 1100°C. The transmutation elements (primarily Re and Os) form clusters and precipitates. Scanning transmission electron microscopy (STEM)/Energy dispersive spectroscopy (EDS) and high-resolution TEM were used to identify the composition and the phase of Re/Os-rich precipitates. These precipitates exhibit Re-cloud and Os-core morphology, which were identified as χ phase. Two orientation relationships of the χ phase precipitates with the tungsten matrix were observed: $[110]_W||[110]_X$, $(002)_W||(006)_X$ and $[110]_W||[110]_X, (002)_W||(\bar{4}4\bar{2})_X$.

4.1.3 PROGRESS AND STATUS

K-doped tungsten has demonstrated greater resistance against recrystallization than pure tungsten. In this report, we present the characterization results on the irradiation induced precipitates in K-doped tungsten, which was irradiated at a nominal temperature of 1100°C to 0.47 dpa in HFIR. Tungsten under neutron irradiation transmutes to Re and Os, which often form clusters and precipitates at concentrations below their equilibrium solubility limits.

Figure **28** shows a STEM high angle annular dark field (HAADF) image and Re and Os energy dispersive spectroscopy (EDS) maps of the same region in the irradiated K-doped tungsten. A grain boundary is captured in this TEM foil, which shows Re and Os segregation. In addition, precipitates were observed, and they have Os-core and Re-cloud morphology.

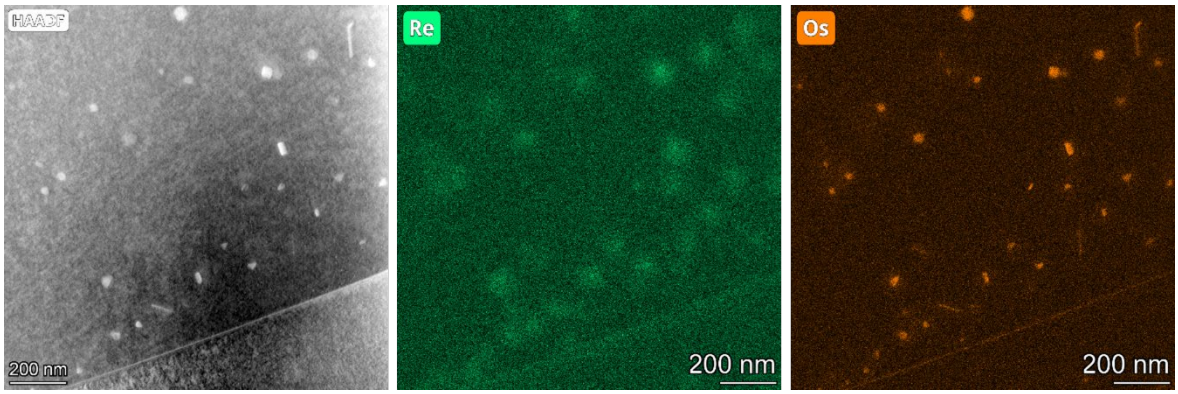

Figure 28. (left) HAADF image, (middle) Re, and (right) Os EDS maps of K-doped W irraidated at 1100°C to 0.47 dpa.

To identify the phase of these principates, a TEM sample was tilted to tungsten's [110] zone, and the diffraction pattern is shown in Figure **29**a. Other than the strong diffraction from the tungsten matrix, weak satellite diffraction spots were observed. Dark field images shown in Figure **29**b shows that these weak diffraction spots are from the Re/Os-rich precipitates.

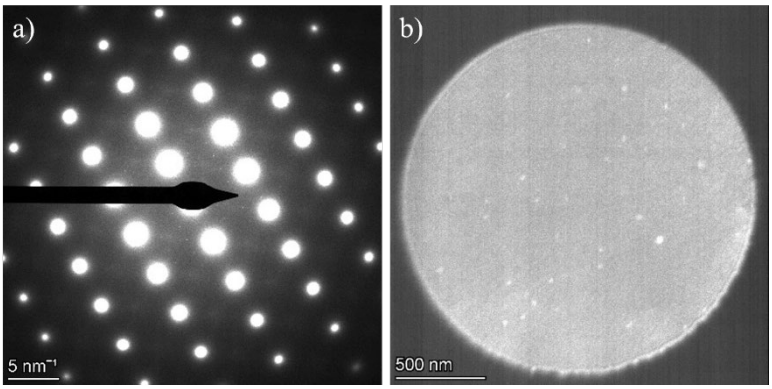

Figure 29. (left) Diffraction pattern of tungsten on the [110] zone, and (right) the dark field TEM image showing the Re/Os-rich precipitates.

High resolution (HR) TEM images were taken on these Re/Os precipitates under the [110] zone of the tungsten matrix. Examples HRTEM images of the precipitates are shown in Figure 30a and Figure 30d. The results reveal that these Re/Os-rich precipitates are of the same phase but with different orientation. Fast Fourier Transform (FFT) images of these two HRTEM images are shown in Figure 30b and Figure 30e respectively, and both of them match the pattern of χ phase under the [110] zone. These precipitates have different orientation relationships with the matrix: $[110]_W||[110]_{\mathrm{X}}, (002)_W||(006)_{\mathrm{X}}$ and $[110]_W||[110]_{\mathrm{X}}, (002)_W||(\bar{4}4\bar{2})_{\mathrm{X}}$ for precipitates in Figure 30a and Figure 30d, respectively. Simulated patterns of such orientation relationship for precipitates and the matrix are shown in Figure 30c and Figure 30f.

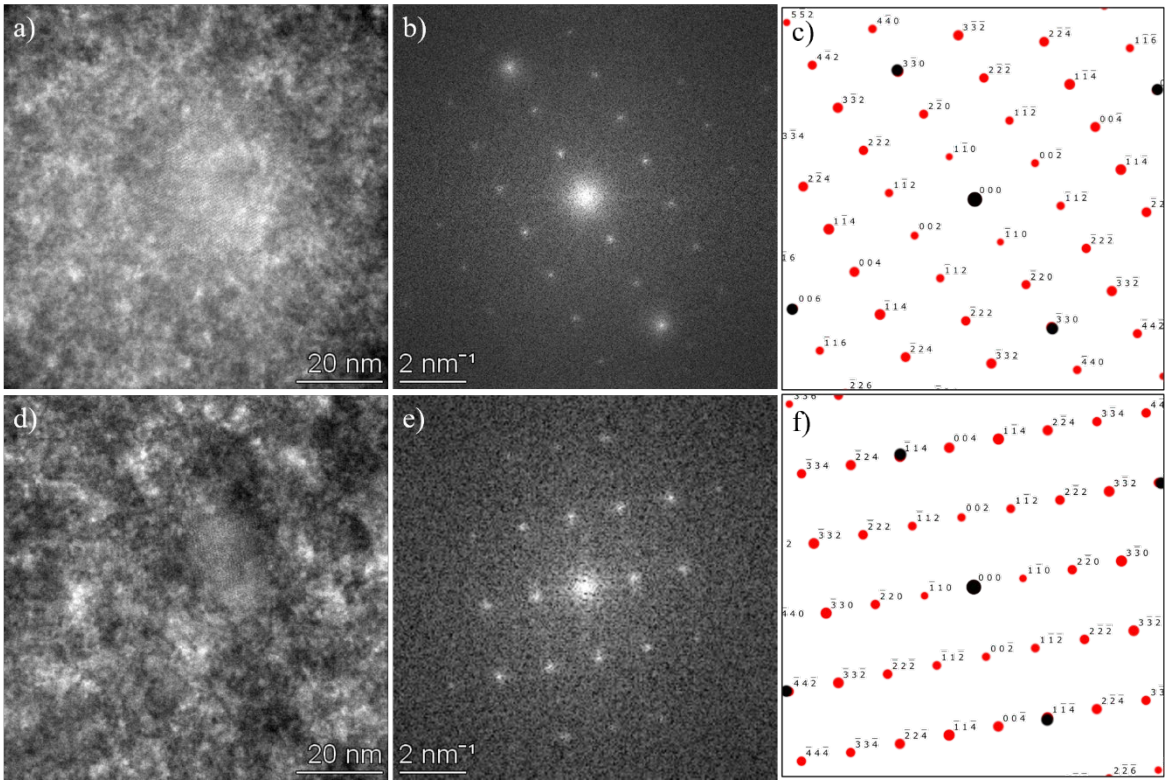

Figure 30. (a,d) High resolution TEM image of two Re/Os-rich precipitates. The FFT of a) and d) are shown in b) and e) respectively, which indicates the orientation relationship as $[110]_W||[110]_X$, $(002)_W||(006)_X$ and $[110]_W||[110]_X$, $(002)_W||(\bar{4}4\bar{2})_X$ for the tungsten matrix and χ phase precipitates, respectively. Simulated patterns of such relationships are shown in c) and f).

4.1.4 FUTURE RESEARCH

Hydrogen retention and desorption experiments will be performed on irradiated W, and the results of transmission electron microscopy will be used to identify hydrogen trapping sites.

4.2 CRACKING IN HIGH-HEAT-FLUX TESTED TUNGSTEN

C. M. Parish, R. Juneja, J. Rapp, T. Gray, and A. Hussain*
**parishcm@ornl.gov*

4.2.1 OBJECTIVE

Establish a methodology for tracing crack-paths in tungsten. This has also been reported in the semi-annual progress report [1].

4.2.2 SUMMARY

A large polycrystalline tungsten test piece was exposed to high-heat-flux in vacuum at the Applied Research Laboratory (ARL) at Pennsylvania State University. Cracking and melting were observed. The specimen (~80 mm tall, ~2.2 kg) was examined in plan-view using the large-chamber Tescan Mira3 GMH SEM in the ORNL LAMDA laboratory. Imaging and X-ray spectroscopy was used to study the cracks and melt regions. The sample was then sectioned by electrical discharge machining. One cracked section was prepared using a diamond saw and metallography for cross-sectional electron backscatter diffraction (EBSD) in scanning electron microscopy (SEM). The crack path was observed and related to grain structures.

4.2.3 PROGRESS AND STATUS

In plan-view, the structure was seen to contain thin, long cracks and some debris or dirt on the surface (Figure 31 left). The cracks contained dark electrically insulating material that showed carbon by X-ray spectroscopy. Leaf- or flower-like structures were observed (Figure 31, right) which might have been melt structures. Low-energy X-ray mapping found no carbon or oxygen concentration in the leaf structures, so they were probably either pure tungsten or a very thin surface layer of oxide or oxycarbide.

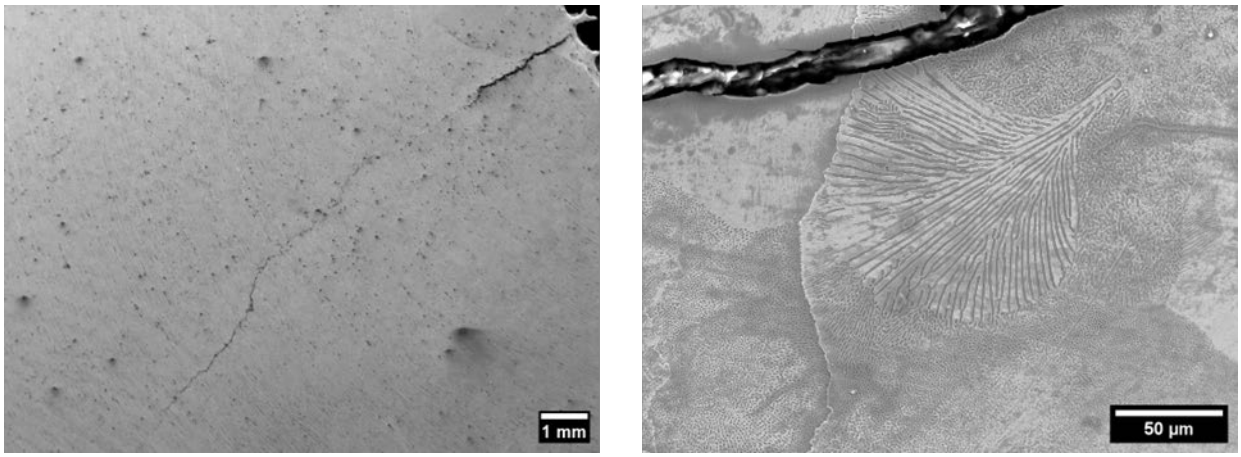

Figure 31. Plan-view SEM images at low and high magnification of cracking and melt structures.

In cross-section, large grains consistent with aggressive recrystallization from high temperature were observed (Figure 32). Further, the crack was seen to be entirely intergranular, moving down grain boundaries and not cutting through grains. (i.e., crystallographic orientations on either side of the crack were not similar.) Whether the crack occurred down the grain boundaries or the crack occurred and then grain growth occurred that was arrested by the free surface cannot be determined from post-mortem EBSD.

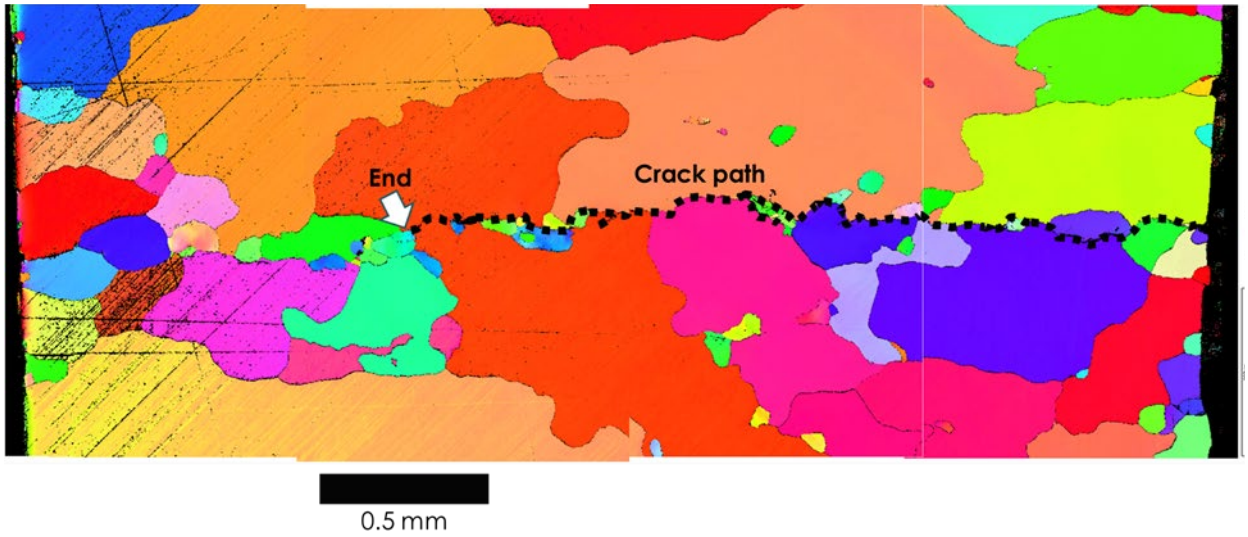

Figure 32. Cross-sectional EBSD montage showing the intergranular cracking.

4.2.4 FUTURE RESEARCH

An ORNL LDRD (R. Juneja, PI) has been funded and will couple multi-scale modeling with these results.

4.2.5 REFERENCES

[1] C. M. Parish, R. Juneja, J. Rapp, T. Gray, and A. Hussain. Cracking in High-Heat-Flux Tested Tungsten. In: Fusion Materials Program Semiannual Progress Report for the Period Ending June 30, 2023, No. ORNL/TM-2023/3142. Oak Ridge National Laboratory (ORNL), Oak Ridge, TN (United States), 2023, P. 70-71. https://www.osti.gov/biblio/2204562; https://doi.org/10.2172/2204562

4.3 DETERMINATION OF TRANSMUTATION ISOTOPIC PRODUCTS FROM IRRADIATED TUNGSTEN

X.-Y. Yu, Y.-R. Lin, L. Howard, Y. Katoh*
**yuxiaoying@ornl.gov*

4.3.1 OBJECTIVE

The objective of this project is to determine the post-neutron irradiation transmutation products of tungsten (W) using high resolution time-of-flight secondary ion mass spectrometry (ToF-SIMS). The primary goal is to demonstrate that ToF-SIMS can offer sufficient mass resolution to resolve isotopic products of W resulting from neutron irradiation.

4.3.2 SUMMARY

We performed detailed ToF-SIMS spectral analysis of irradiated tungsten specimens that were exposed to different neutron doses to demonstrate (1) that SIMS has sufficient mass resolution to resolve isotopic peaks of tungsten, rhenium (Re), and osmium (Os) that have close mass to charge ratios (*m/z*), and (2) SIMS detection is sensitive and selective to obtain chemical makeup information of irradiated tungsten specimens and to provide insights into transmutation pathways.

4.3.3 PROGRESS AND STATUS

To comprehend the effects of neutron spectrum on clustering and precipitation in neutron-irradiated tungsten specimens, a comprehensive ToF-SIMS investigation was conducted. This study involved examining two high-purity single-crystal tungsten samples, each with a starting purity exceeding 99.99 wt.%. The TE01 and W18 specimens were subjected to different neutron spectra – Gd-shielded and unshielded, respectively. The W18 sample was irradiated at a temperature of 700°C, while the TE01 sample was irradiated at 753°C. The neutron fluence was consistently maintained at a level of $2.2\text{-}3.5\times10^{25}$ n/m² (equivalent to 0.6 – 0.7 dpa).

Post-irradiation sample preparation took place in the Low Activation Materials Development and Analysis (LAMDA) laboratory at ORNL. For SIMS analysis, focused ion beam (FIB) techniques were employed to prepare lift-out samples with dimensions of $20\times15\times10$ μm^3 from the bulk. The sample was protected by capping it with platinum (Pt) before milling. The lift-out process involved initial milling and coarse surface polishing using a FEI Quanta3D Dual Beam system operating at 30 kV. The lift-out materials were then welded with Pt deposition to either a molybdenum FIB lift-out grid or a silicon wafer with dimensions of 1×1 cm.

A ToF-SIMS V spectrometer (IONTOF GmbH, Münster, Germany) was used to analyze the irradiated tungsten samples. The SIMS analysis was performed using a 30 keV pulsed bismuth (Bi_3^+) primary ion beam under high vacuum of 4.8×10^{-8} mbar during measurements. The Bi_3^+ primary ion beam scanned over a 150 × 150 μm^2 area with a resolution of 256 by 256 pixels. The spectrum was acquired for 10 scans. The primary ion doses in all measurements were lower than the static limit, and the damage artifacts resulting from the Bi_3^+ primary ion beam were negligible. The mass resolutions of the detected peaks in the SIMS spectrum are in the range of 8,000 to 11,000, varying from sample to sample depending on the sample roughness. Mass spectra were calibrated using CH^+, CH_2^+, Si^+, W^+, and Bi^+ in the positive ion mode using the SurfaceLab software version 7.0.

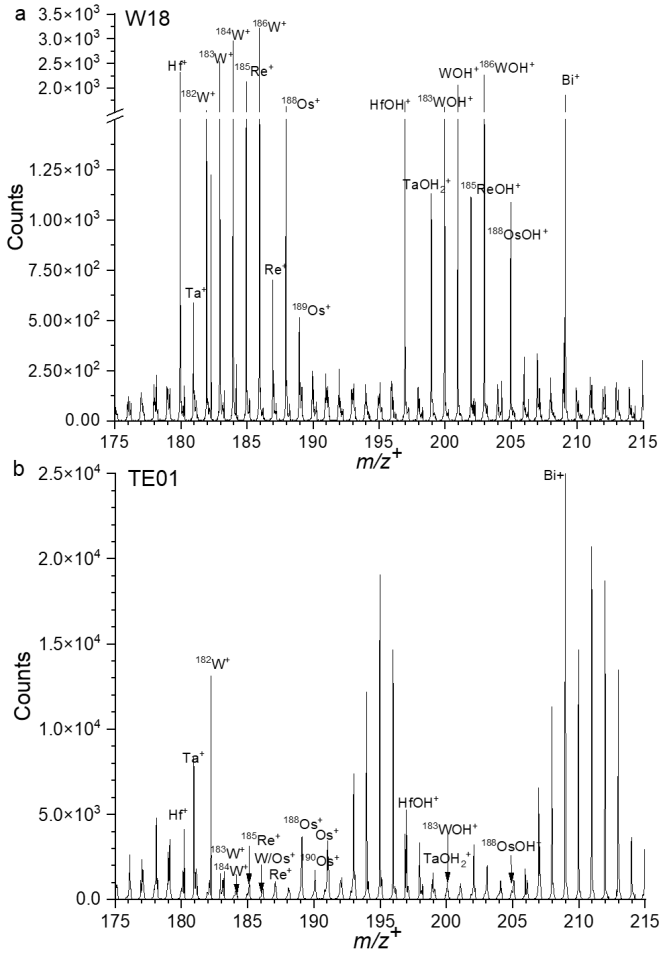

Figure 33. ToF-SIMS spectral comparison of the W18 (a) and TE01 (b) irradiated tungsten sample in the m/z^+ range of 175 – 215 in the positive ion mode.

Figure 33 depicts the ToF-SIMS spectral comparison of the W18 and TE01 irradiated tungsten samples in the m/z^+ range of 175 – 215 in the positive ion mode. The W isotopic peaks are evident in both irradiated tungsten samples, including: m/z^+ = 181.9457 for $^{182}W^+$, m/z^+ = 182.9471 for $^{183}W^+$, m/z^+ = 183.9468 for $^{184}W^+$, m/z^+ = 184.9489 for $^{185}W^+$, m/z^+ = 186.9566 for $^{187}Re^+$, m/z^+ = 187.9511 for $^{188}Os^+$, m/z^+ = 199.9575 for $^{185}ReO^+$, and m/z^+ = 209.9835 for Bi^+. The peak of m/z^+ = 209.9835 for Bi^+ comes from the bismuth primary ion beam and it is used as a reference peak in calibration. The peak of m/z^+ = 185.9463 can be assigned as either $^{186}W^+$ with a theoretical m/z^+ (m/z_{the}) of 185.95436 or $^{186}Os^+$ with a theoretical m/z^+ of 185.95384. The relative mass accuracy is defined as $\Delta m=(m/z_{obs} - m/z_{the})/m/z_{the} \times 10^6$ (in ppm), where m/z_{obs} denotes the observed m/z in SIMS. Using this formula, the Δm is 32.5 ppm if the peak is assigned as $^{186}W^+$ or 29.8 ppm if the peak is assigned as $^{186}Os^+$. While acceptable, further refinement could involve modeling to effectively distinguish the two isotopic peaks with close mass to charge ratios. The preliminary SIMS analysis illustrates that the W isotopic peaks as well as transmutation product peaks, such as Re and Os, are observable with good mass resolution. Additionally, transmutation products such as Hafnium (Hf) and Tantalum (Ta) and their corresponding oxides are observed, indicating that ToF-SIMS has the sensitivity to detect other transmutation products that are not as well characterized as Re or Os.

Similarly, Figure 34 depicts the ToF-SIMS spectral comparison of the W18 and TEO1 irradiated tungsten samples in the m/z^- range of 195 – 240 in the negative ion mode. The isotopic peaks of metal oxides are

evident in both irradiated tungsten samples, including: m/z^- = 199.9539 for $^{182}WO^-$, m/z^- = 200.9576 for $^{183}WOH^-$, m/z^- = 201.9537 for $^{186}WO^-/^{186}OsO^-$, m/z^- = 202.9511 for $^{185}ReOH^-/^{186}OsOH^-$, m/z^- = 205.9560 for $^{190}OsO^-$, m/z^- = 208.9581 for OsO^-, m/z^- = 208.9588 for $^{177}HfO_2^-$, and m/z^- = 219.9667 for HfO_2^-..

Comparisons between the W18 and TE01 samples show that W18 has higher abundances of W, Re, and Os products than TE01. This finding agrees with our previous STEM EDS results, which suggest that W18 (with an unshielded neutron spectrum) contains a larger amount of nuclear transmutation products compared to TE01 (with a shielded neutron spectrum), as expected. Additional analysis and peak identification are ongoing. SIMS spectral results will be included in a paper.

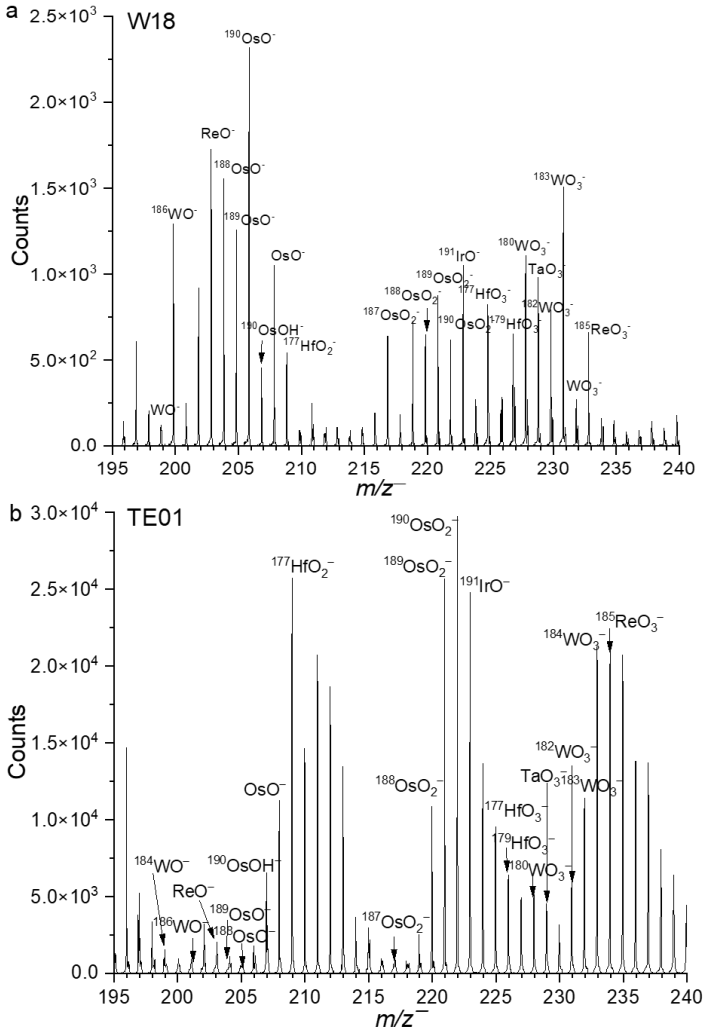

Figure 34. ToF-SIMS spectral comparison of the W18 (a) and TE01 (b) irradiated tungsten samples in the m/z^- range of 195 – 240 in the negative ion mode.

4.3.4 FUTURE RESEARCH

A manuscript outlining the current study on neutron-irradiated tungsten samples is currently underway and is nearing submission to a peer-reviewed journal. Future research will focus on post-irradiation examination of the same tungsten materials complemented with APT and TEM analysis. This effort is intended to

demonstrate SIMS's capabilities in revealing transmutation products and establish the technical foundation of product identification and quantification to further the understanding of neutron displacement damage on mechanical property changes and improve our insights of transmutation on tungsten materials.

4.3.5 REFERENCES

[1] X.-Y. Yu, Y.-R. Lin, L. Howard, and Y. Katoh. Determination of Transmutation Isotopic Products from Irradiated Tungsten. U.S. DOE Office of Fusion Energy Science, Fusion Materials, Semiannual Progress Report, DOE/ER-0313/74 (2023)

4.4 MICROSTRUCTURE, TENSILE PROPERTIES, AND ELECTRICAL CONDUCTIVITY OF NEUTRON IRRADIATED CuCrNbZr

A. E. Perrin, J. W. Geringer, Y. Yang, Y. Katoh, S. J. Zinkle (UTK)*
**perrinae@ornl.gov*

4.4.1 OBJECTIVE

High strength, high conductivity copper alloys that can resist creep at high temperatures are one of the primary candidates for efficient heat exchangers in fusion reactors. New Cu-Cr-Nb-Zr (CCNZ) alloys were designed to improve the strength and creep life of ITER grade Cu-Cr-Zr (CCZ) alloys. This was achieved through a uniform distribution of Cr_2Nb Laves phase precipitates at grain boundaries as well as Cr and Cu_5Zr nanoprecipitates in the matrix, all contributing to a reduction of grain boundary sliding. The measured creep rupture times for these improved alloys is about ten times higher than the Cu-Cr-Zr alloys at 90-125 MPa at 500°C. The electrical conductivity and tensile properties of the advanced and ITER alloys are comparable. However, the effects of neutron irradiation on these material properties have not been studied, despite the need for a clear understanding of the neutron irradiation effects on alloys designed for use in cooling channels of ITER and DEMO divertors. SS-J3 tensile specimens of CCNZ were neutron irradiated in the High Flux Isotope Reactor (HFIR) to 5 dpa between 275°C and 325°C. Post-irradiation characterization included room temperature electrical conductivity measurements, hardness, and tensile tests. Microstructural evaluation used scanning electron microscopy, transmission electron microscopy, and energy dispersive spectroscopy to characterize the irradiation-induced changes in the microstructure.

4.4.2 SUMMARY

SS-J3 specimens of high purity Cu-Cr-Nb-Zr with a composition of Cu-2Cr-1.35Nb-0.15Zr wt% were characterized post-irradiation and compared with ITER grade Cu-Cr-Zr alloys irradiated in identical conditions with composition Cu-0.81Cr-0.07Zr wt% [1]. All post-irradiation examination on CCNZ reported here was performed at room temperature; high temperature characterization of tensile properties will continue in FY24.

Microstructural characterization of irradiated CCNZ shows that the Cr_2Nb Laves phase is retained and the grain size distribution roughly retains the 2-11 μm average grain sizes from the non-irradiated, as-aged CCNZ (Figure 35) [2]. However, after irradiation, the CCNZ contains a lower number density of Cr precipitates, and Cu_5Zr precipitates are not directly observed through scanning electron microscopy. Instead, the Zr is preferentially contained in the Cr_2Nb phase. A higher Cr and Zr concentration are both detected in the Cu matrix through energy dispersive spectroscopy (EDS, Figure 35); the EDS measurements suggest the concentrations are significantly higher than equilibrium solubility limit, but as EDS is not reliable for quantitative measurement at low concentrations, atom probe tomography will be used to measure these concentrations in FY24. Cavitation during deformation was observed to occur primarily at the interface between the matrix and Laves phase in all samples.

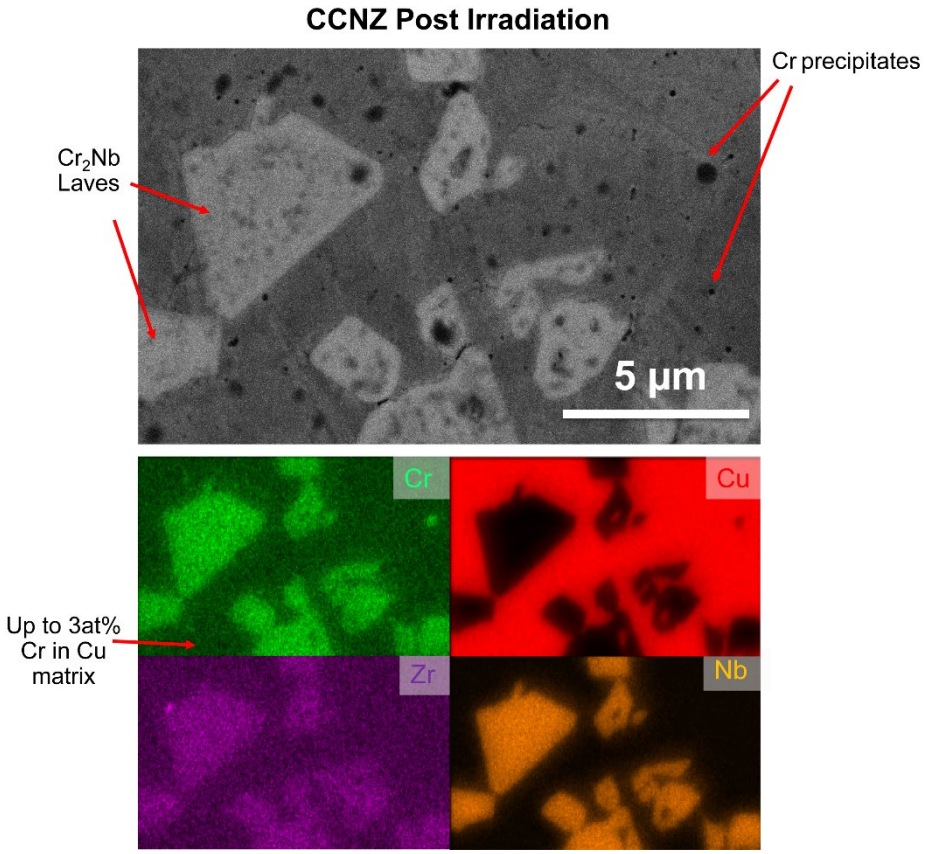

Figure 35. Top: Post-irradiation microstructure showing fine Cr precipitates in a Cu matrix, dispersed around Cr_2Nb. Bottom: Energy dispersive spectroscopy maps showing qualitative concentrations of Cr and Zr detected in the Cu matrix.

Electrical resistivity measurements were used to indirectly measure electrical conductivity of the samples; because electrical conductivity is typically proportional to thermal conductivity in metals, this provides an estimate of the degradation of the thermal properties of CCNZ under irradiation. Non-irradiated CCNZ has a lower electrical conductivity of 72% of the International Annealed Copper Standard (IACS), compared to that of CCZ (84% IACS). After irradiation, both alloys have comparable conductivity, around 45% IACS (Figure 36a). Further characterization of solute concentration in the matrix, transmutation products, and radiation damage at the nanoscale will be used to quantify their respective contributions to the decrease in conductivity, but dissolution of Cr and Zr rich precipitates back into the matrix is likely a significant factor; greater retention of Zr and Cr in the Laves phase may be why the electrical conductivity of post-irradiation CCNZ is not worse than the CCZ despite higher concentrations of both.

Hardness testing found irradiation hardening in CCNZ which decreased with increasing irradiation temperature, mimicking trends observed in CCZ (Figure 36b). Tensile testing found that CCNZ alloys maintained their advantageous yield strength and ultimate tensile strength over CCZ at room temperature even at high irradiation temperatures (Figure 36c), but a significant drop in elongation was observed above

T_{irr}=300°C (Figure 36d). Further characterization of the nanoscale is needed to determine the cause of the drastic loss of ductility at higher irradiation temperatures.

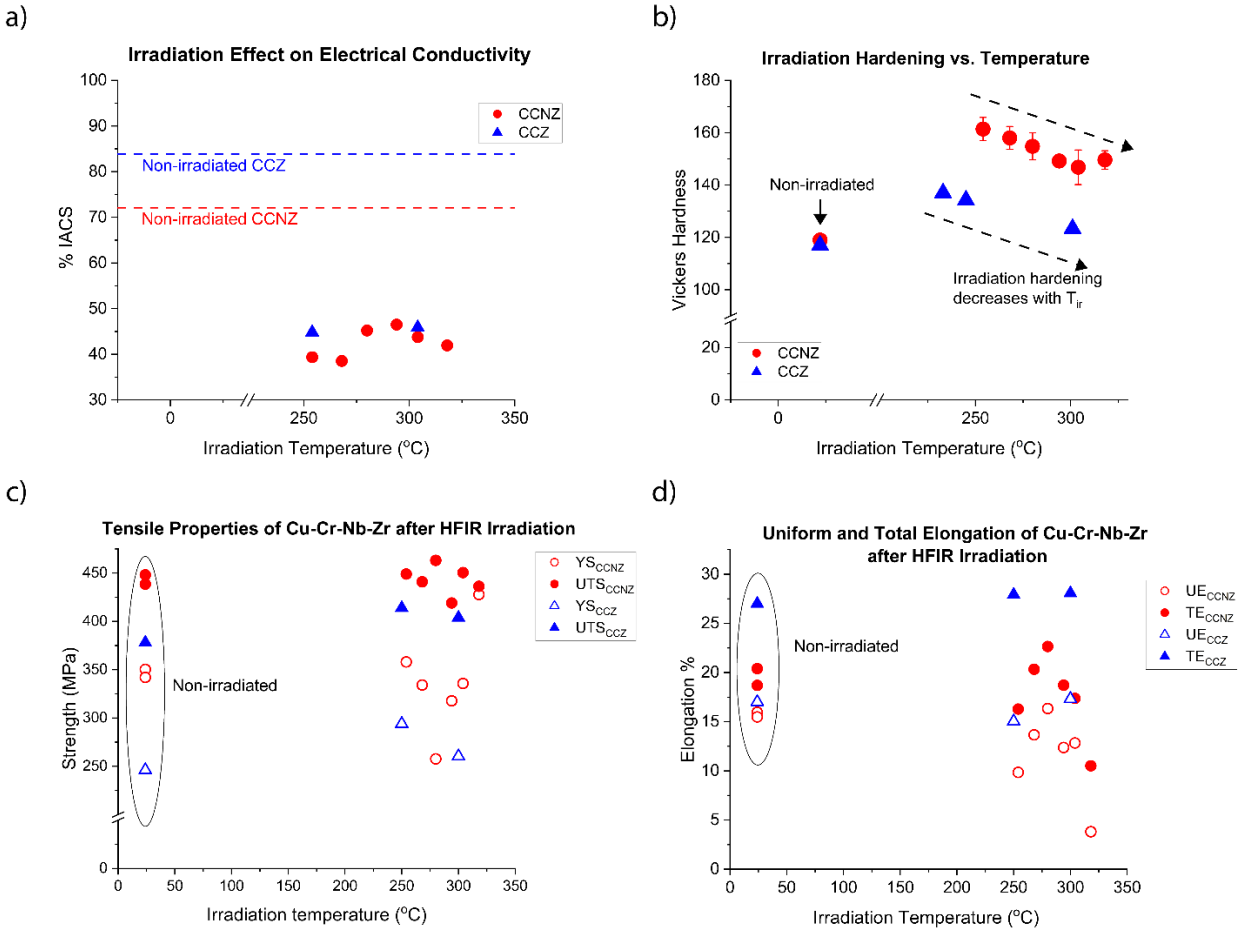

Figure 36. (a) Electrical conductivity of CCNZ compared to ITER grade CCZ before and after irradiation. (b) Hardness vs irradiation temperature of CCNZ and benchmark CCZ. (c)-(d) Room temperature tensile strength and elongation of CCNZ vs irradiation temperature with CCZ benchmark.

The broad conclusions reached by the FY23 PIE of high purity Cu-Cr-Nb-Zr alloys found that they have comparable room temperature post-irradiation electrical conductivity and tensile properties to ITER grade Cu-Cr-Zr alloys and suggest that the additional Laves phase is a promising design concept for improving creep properties of CCZ alloys for fusion environments without compromising the thermal properties.

4.4.3 FUTURE RESEARCH

Immediate future work on these alloys will include transmission electron microscopy to image irradiation damage, and atom probe tomography to assess the transmutation products and matrix composition. Relative contributions of transmutation, ballistic mixing of precipitates, solute segregation, and defect formation to the changes in electrical resistivity will be quantified using additional TEM and APT results. Elevated temperature tensile tests on samples with the same irradiation temperatures will complete the PIE for samples irradiated near 300°C. We will then focus on full post-irradiation examination of CCNZ samples irradiated at lower temperatures (100-200°C).

4.4.4 REFERENCES

[1] D. Hamaguchi, Cu alloy PIE, DOE-QST Fusion Reactor Materials Collaboration Progress Review (2023)

[2] L. Wang, C. Zheng, B. Kombaiah, L. Tan, D. J. Sprouster, L. L. Snead, S. J. Zinkle, Y. Yang. Contrasting roles of Laves Cr_2Nb precipitates on the creep properties of novel CuCrNbZr alloys. *Mat. Sci. Eng. A. 779, (2020) 139110*

4.5 PLASMA FACING COMPONENT INNOVATIONS BY ADVANCED MANUFACTURING AND DESIGN

T. Graening, Y. Yang, C. Ledford, M. Kirka, , Y. Katoh, I. Robin (UTK), D. Ebeperi (Texas A&M), I. Karaman (Texas A&M), J. Ye (LLNL), Y. Wang (UCLA)*
**graenigt@ornl.gov*

Supported by DOE-FES and ARPA-E

4.5.1 OBJECTIVE

Tungsten as a first wall/blanket material in PFCs requires integration with reduced-activation ferritic martensitic (RAFM) steels for structural components. Currently, major drawbacks are the requirement of brazing, the formation of a brittle interface, and a large difference between the coefficients of thermal expansion of tungsten and steel. The objective of this project is to develop a novel transitional multilayer structure to join tungsten and RAFM steels using three interlayers. The composition of each interlayer was selected based on computational thermodynamics and diffusion kinetics to ensure a body-centered cubic (bcc) single-phase structure and prevent the formation of a brittle intermetallic phase region in the temperature range of 550~1100 ºC.

4.5.2 SUMMARY

Additive manufacturing of tungsten and the design and application of a gradient transition from tungsten to steel for fusion reactors were tasks of this ARPA-E GAMOW and FES project. Tungsten printing using Electron Beam Melting (EBM) was successful and enables 99.98% dense prints with complex geometry. Laser Powder Bed Fusion (LPBF) was explored with W3Re and doped tungsten to enable crack-free printing using laser-based printing methods, which was otherwise not possible using pure tungsten because it suffers from faster cooling which can lead to thermal cracking. Direct Energy Deposition (DED) was used to successfully print gradient designs. Cracking was found at the interface between two components of the multilayer interface, specifically between FeCrAl and VCrAl, which was found to be caused by a B2 phase formation.

4.5.3 PROGRESS AND STATUS

4.5.3.1 Thermodynamic Simulations and gradient design

Thermodynamic simulations were performed to identify an interlayer design which can form a body centered cubic lattice cell throughout the gradient structure that is stable across the operating temperature window of 550 to 1100 °C. Preventing intermetallic phases while grading the coefficient of thermal expansion and mechanical properties of the materials would be beneficial for an extended lifetime of components. Spark Plasma Sintering (SPS) of discs of the interface materials was performed (see Figure 37) to investigate the interfaces using scanning electron microscopy (SEM) and transmission electron microscopy (TEM) techniques in comparison with simulated diffusion distances. Microstructure characterization confirmed the diffusion parameters for most elements. The interfaces between castable nanostructured alloy (CNA) steel and FeCrAl show a hardness decrease, as shown in Figure 38, caused by ferrite formation triggered by the diffusion of Al towards the CNA at SPS temperatures. A hardness increase between FeCrAl and VCrAl is shown which was thought to be caused by VC formation, but was later revealed by TEM to be caused by a B2 phase formation. The hardness gap between VCrTi and W can be overcome by grading the interface through chemical mixing using DED methods.

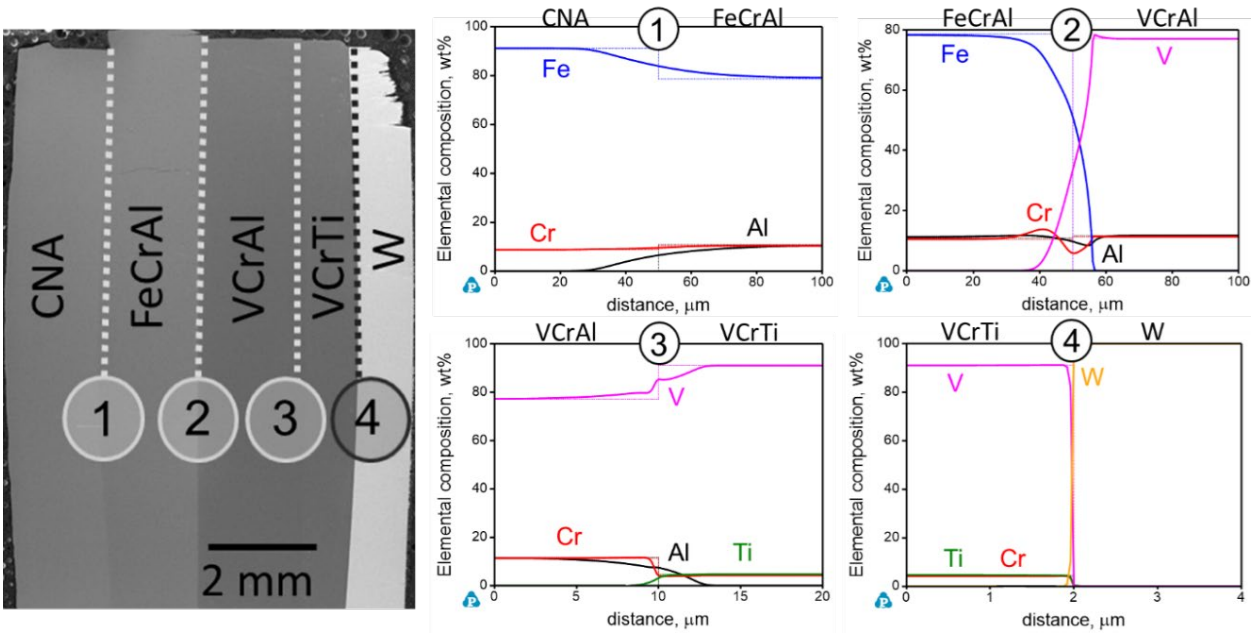

Figure 37: SEM micrograph of SPS sample with interlayers 1 to 4 next to the simulated diffusion distances of major elements for each interface.

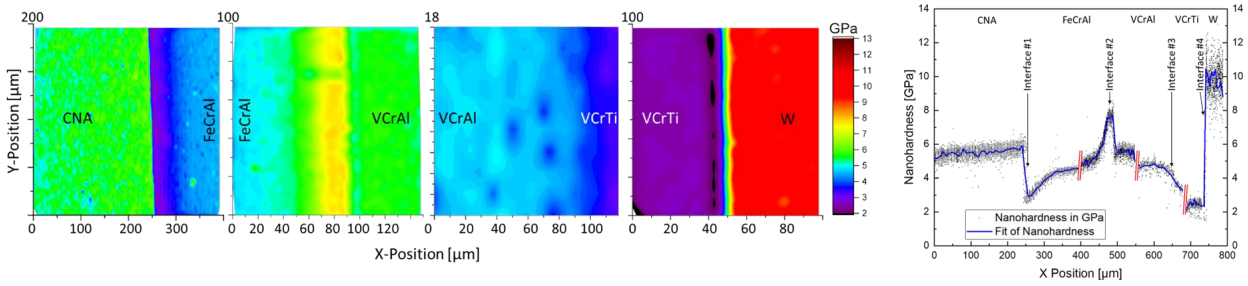

Figure 38: Hardness mapping from CNA to tungsten next to the accumulated linescan on the right side reveals significant hardness changes between CNA and FeCrAl, and between FeCrAl and VCrAl.

4.5.3.2 Additive manufacturing of tungsten and a graded transition

Additive manufacturing of W, W3Re and doped W has been performed using EBM and LPBF. Printability maps have been compiled by single parameter changes on single track and cubic prints. Such a printability map is shown in Figure 39 for LPBF. Success by adding Re and other dopants has been shown by refining the grain size and enabling crack-free prints. High density samples of 99.98% have been produced with W and W3Re. Tailoring of texture has been shown by increasing the energy density resulting in a change from (100) to a (111) orientation in the build direction. Printing of blocks and complex shapes has been demonstrated as highlighted in Figure 40. High density EBM tungsten and W3Re samples were printed for a high-heat flux exposure experiment at DIII-D, showing no unique failure mechanism for the high-density AM-W materials in comparison with conventional ITER-grade tungsten. EBM W and W3Re discs have been produced for High Flux Isotope Reactor insertion in FY24 together with graded samples from CNA to VCrTi.

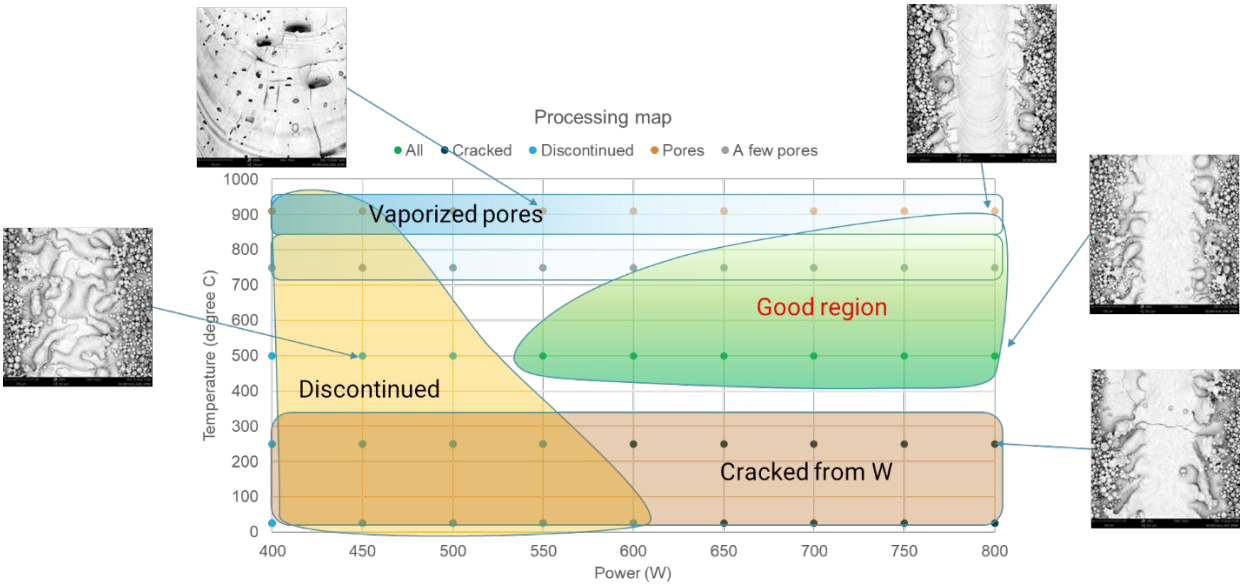

Figure 39: Printability map for W produced by LPBF

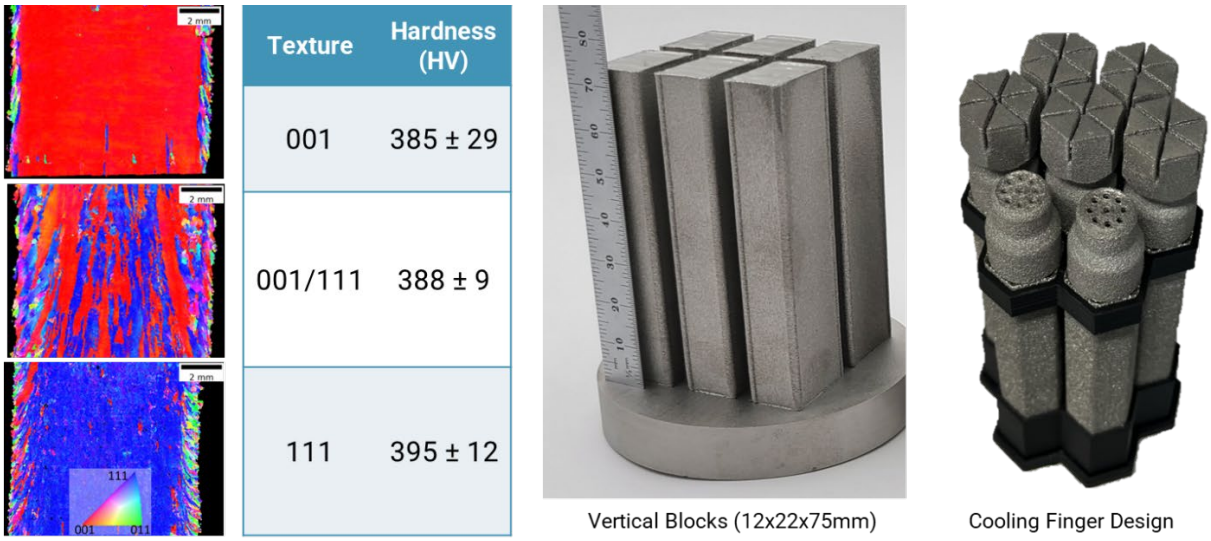

Figure 40: From left to right, tailored texture shown in EBSD maps; correlated hardness values; printed blocks and complex shapes; He-cooled modular divertor with multiple jets.

The gradient was designed using thermodynamic modeling and investigated using spark plasma sintering of discs of tungsten and CNA with 3 interlayers. On that basis, DED at Texas A&M was applied to develop printability maps for each individual chemical composition, before gradients from steel to tungsten were printed. Printed parts of each individual chemical composition were printed with a density higher than 98%, and tensile tests were conducted to compare the results with bulk properties. One major challenge was overcome in producing a graded transition between the vanadium alloy and tungsten. After several iterations, good bonding and a graded transition were achieved as displayed in Figure 41.

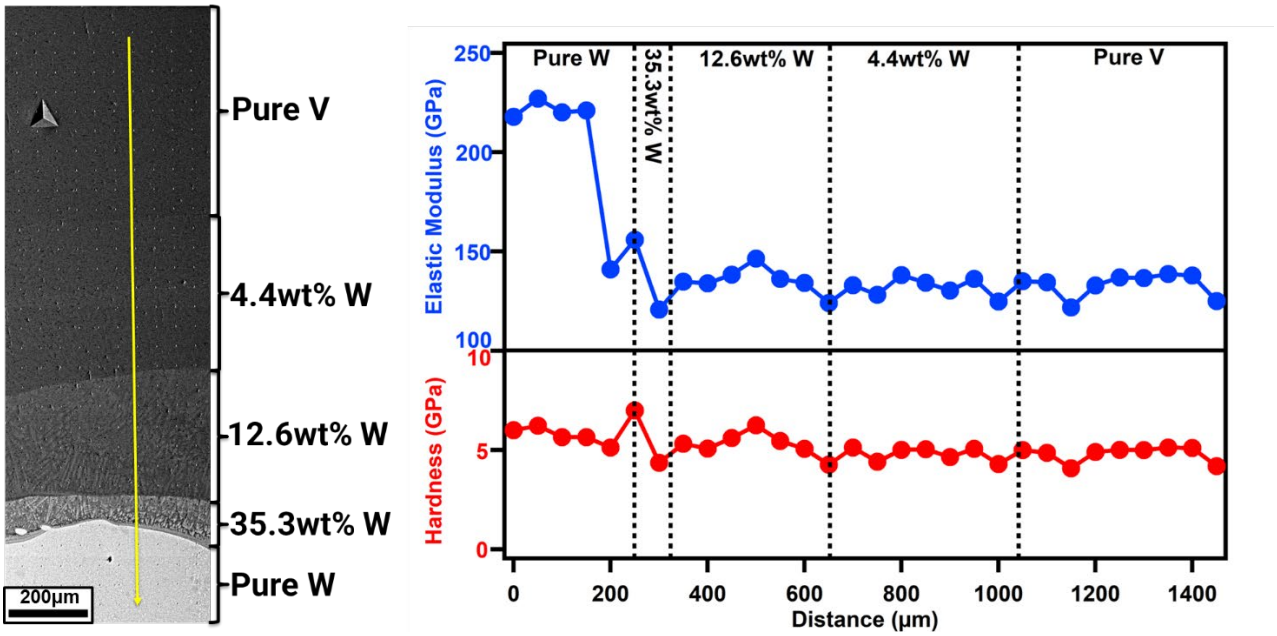

Figure 41: DED print of vanadium on tungsten with simultaneous printing of vanadium alloy and tungsten forming a gradient.

4.5.4 FUTURE WORK

Graded tensile samples fabricated using DED have been fabricated, in addition to tungsten LPBF samples, both of which will be tensile tested in FY24. DED printing with mitigation strategies to avoid a sigma or B2 phase formation during the printing process will be applied.

4.6 BORON DOPED TUNGSTEN FOR FUSION PFCs

X.-Y. Yu, T. Graening, G. Yang, Y. Katoh*
**yuxiaoying@ornl.gov*

4.6.1 OBJECTIVE

The objective of this project is to determine: 1) if boron is doped into the tungsten plates via the usual route of powder metallurgy and hot rolling and 2) if boron is doped at the desired quantity.

4.6.2 SUMMARY

The ALMT prepared boron (B) doped tungsten (W) plates were characterized using microscale spectroscopy and microscopy including scanning electron microscopy (SEM), Raman spectroscopy and imaging, and depth profiling of time-of-flight secondary ion mass spectrometry (ToF-SIMS). Boron was detected at the surface of the doped W plates using Raman and SIMS.

4.6.3 PROGRESS AND STATUS

Doping a small amount of B can reduce recrystallization of W effectively [1, 2]. B-doping ductilizes W and it is beneficial for additive manufacturing (AM) of W [3]. B-doping can potentially offer benefits to PFC performance. Therefore, understanding basic properties of B-doped W is useful for developing materials for fusion applications. ALMT prepared two B-doped W plates via powder metallurgy and hot rolling, which nominally have 0.1 at% B and 0.01 at% B, respectively. A reference W plate without B doping was also provided as the reference material.

Pieces from all three rolled plates were sectioned and the top surface of the rolled plates was polished to a 0.5 μm finish, followed by a chemical polishing step. SEM was performed using a MIRA 3 SEM (TESCAN USA, Inc.) equipped with an Oxford Symmetry electron backscatter diffraction (EBSD) detector. The probe current was around 6 nA. All EBSD data were collected using a 20 kV accelerating voltage with a 6 nA beam current. Appropriate step sizes of 0.2 μm were used for all scans. Two maps with different sizes were recorded for each sample.

The Raman mapping was collected on a confocal Raman spectrometer (Horiba, 405 nm edge, objective = 50×, a grating with 2400 grooves/ mm, numerical aperture (N.A.) = 0.42, local power <500 μW). The laser spot diameter was estimated to be 1 μm. The scan region was set 17.31 μm × 18.96 μm, with the step size of 0.4 μm × 0.5 μm/pixel. The integration time was set to 8 s for each point. Autofocus mode was applied at each step to assure consistent focus on the sample surface. All Raman mappings were analyzed using Horiba Labspec 6 imaging and spectroscopy software and via the K-means clustering algorithm integrated into the Scikit-learn platform with a previously reported similar method [4, 5].

4.6.3.1 SEM Findings

Figure 42 shows the microstructure of the pure W sheets next to the one doped variant using inverse pole figure (IPF) maps. The rolling direction (RD) of the sheets is from bottom to top. A clear change in grain size and shape is visible with the addition of boron for all boron doped samples(right: 0.01B, 0.1B not shown). The typical elongated grains in the rolling direction were observed in the reference material. They exhibit the expected (001) and (101) texture in normal direction to the rolling direction, with the (101) orientation being preferred in RD [6]. The texture is relatively weak for a rolled tungsten plate, suggesting a low rolling reduction. The texture changes for both boron-doped samples to a lower texture anisotropy, with a preferred (101) orientation in normal direction to the rolling direction. The grain shape appears more

spherical with larger grains which aligns well with current findings of doped-tungsten [7]. Those findings support the speculation that the boron supports the formation of new grains during the thermomechanical treatment process.

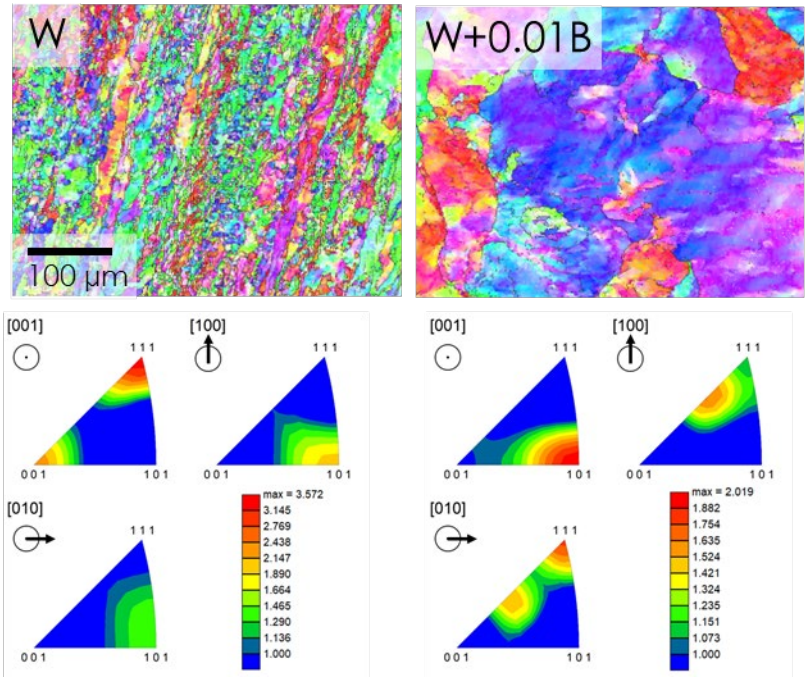

Figure 42. Inverse pole figure (IPF) maps, evaluated in the rolling direction from top to bottom of W and boron-doped W using the same magnification clearly showing a grain size difference. Pole figures on the bottom correspond to the IPF above.

4.6.3.2 Raman Mapping

Figure 43 depicts 2D Raman mapping comparison results of the B doped W coupons against a single crystal W disc. Raman surface spectral comparison in Figure 34a shows that surface compositions are quite different compared to the pristine tungsten. Tungsten oxide (WO_3) is present at room temperature as a mixture of the monoclinic (γ-phase) and triclinic (δ-phase) phases, often revealed by the presence of peaks at 183, 207, 275, 718 and 810 cm^{-1} [8]. Two-dimensional (2D) Raman imaging was also performed. Figure 34a shows the reconstructed surface map of the 0.1 at% B doped W coupon based on the principal component analysis or cluster analysis. Five components or clusters were identified as the main contributors of the spectral features observed in the 2D mapping shown in Figure 34c and Figure 34d corresponding to the B doped W and single crystal W control.

The band in the range of 100–500 cm^{-1} is associated to O–W–O bending modes, and the band in the range 600–1000 cm^{-1} is associated to W–O stretching modes [8]. Raman peaks at 143, 308, 645, 678 cm^{-1} are associated with the monoclinic ε-phase of WO_3. The band at around 960 cm^{-1} is assigned to the terminal W-O stretching mode, possibly on the surface of the cluster and in micro void structures in the plate. The band at around 950 cm^{-1} is ascribed to hydrated tungsten oxide (WO_3, xH_2O), corresponding to the W=O stretching mode [9]. The hydrates may have more bands in the lower-frequency region of under 400 cm^{-1}. These peaks are the main contributor to clusters 0, 1, and 2.

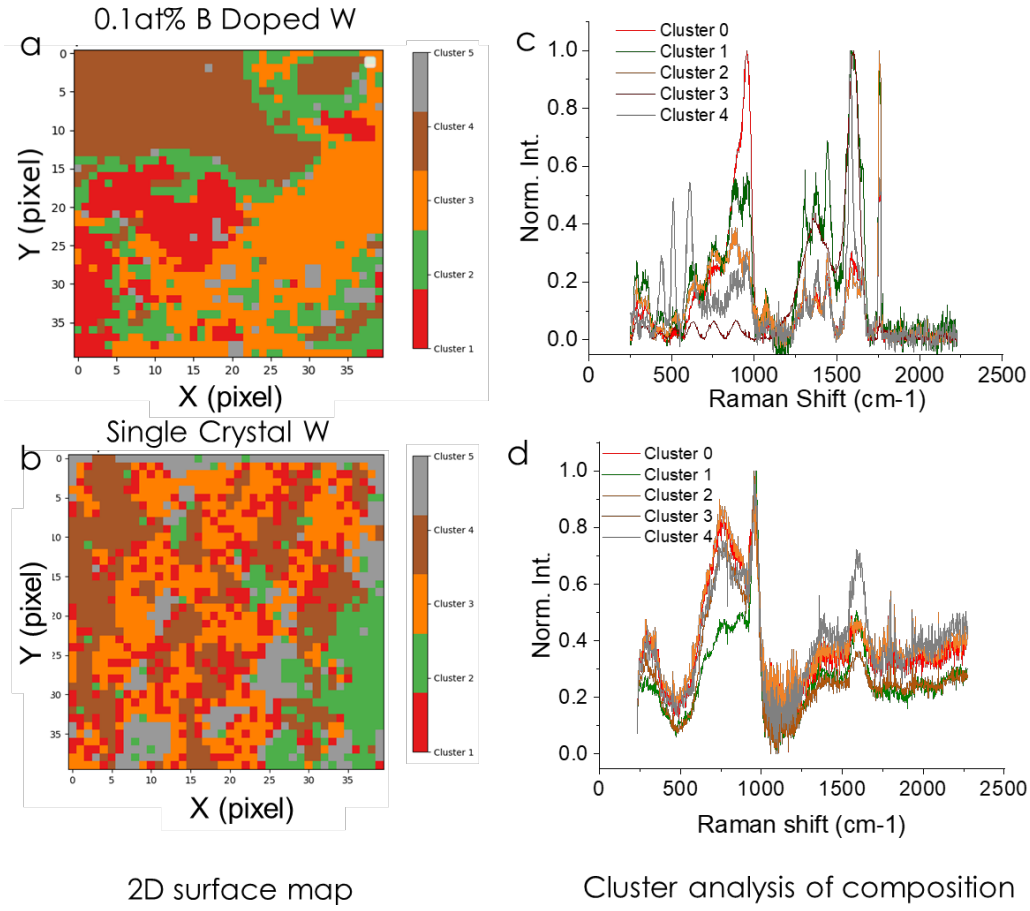

Figure 43. Comparisons of 2D Raman surface mapping of 0.1 at%B doped W coupon (a) and single crystal W (b) with corresponding cluster analyses of surface composition of (a) and (b) depicted in (c) and (d), respectively.

The Raman spectrum also has characteristics of an amorphous tungsten oxide (*a*-WO_3) [10]. The Raman peak at 713.7 cm^{-1} is attributed to *ν*(O-W-O) modes of m-WO_3. The broad band centered at ca. 760 cm^{-1} can be deconvoluted into several Raman peaks, including the strongest peaks at 715 and 807 cm^{-1} of the monoclinic WO_3. Other known vibrational shifts from W-O and O-W-O characteristic of tungsten oxides are also visible from all materials, for example 328.1, 268.5 cm^{-1} indicative of *δ*(O-W-O) [11]. Raman peaks at 318, 645, and 813 cm^{-1} are attributed *h*-WO_3. The spectrum has also characteristic bands of the crystalline tungsten oxide, namely weak bands around 430 and 450 cm^{-1} are visible [9]. These peaks contribute to the loadings of clusters 0, 1, and 2, suggesting surface oxidation of these plates.

The band at 882 cm^{-1} is typical of ethanol [12]. The appearance of bands at ~1368 and ~1590 cm^{-1} indicates existence of disordered graphitic carbon. They are contributors to clusters 3 and 4. Surface contamination is evident in all main components of the map. Among them, cluster 3 mainly represents surface contamination components like graphite. The other clusters are mixtures of WO_3 with different degree of surface contaminations or solvent used to clean the surface.

There is not a report about B doped W in Raman to the best of our knowledge. Using Raman spectra acquired from B, B doped graphite, or B doped 2D materials, we evaluated the cluster components. The Raman peak wave numbers shift to higher values due to doping. The peaks of 500 cm^{-1} and 1230 cm^{-1} were

determined previously as a result of B doping into the diamond lattice [13]. We postulate peaks at 514 cm^{-1}, 1308 cm^{-1}, 1387 cm^{-1}, and 1443 cm^{-1} may reflect the effect of boron doping on the diamond lattice, which are represented in cluster 4. The peaks appearing at 611 cm^{-1}, 717 cm^{-1}, 763 cm^{-1}, and 763 cm^{-1} can be related to b-B. The peaks occurring at ~ 850 cm^{-1}, 880 cm^{-1}, and 948 cm^{-1} can be related to g-B [14]. Thus, cluster 4 likely represents the contributions from B Raman spectral peaks. The distribution of cluster 4 is depicted in gray in Figure 43a. These findings suggest that that B is incorporated into the W matrix [15]. In comparison, the main compositions of the clusters identified in the single crystal W disc have similar Raman shifts, unlike the B doped coupons. These spectral signatures are attributed to tungsten oxides.

Additional analysis and peak identification of the Raman observations are ongoing. Results from other spectroscopy and microscopy analysis like SIMS will be incorporated in the determination of the B distribution and quantification in a manuscript.

4.6.4 FUTURE RESEARCH

A manuscript reporting the determination of B amount doped in W will be prepared. Future research will focus on post-irradiation examination of the B doped tungsten coupons after they are deployed in a neutron irradiation campaign.

4.6.5 REFERENCES

[1] C. Fan, X. Hu, Recovery and recrystallization of warm-rolled tungsten during helium thermal desorption spectroscopy annealing, Journal of Nuclear Materials 569 (2022) 153914.

[2] A. Hasegawa, T. Miyazawa, D. Itou, T. Hattori, K. Yohida, S. Nogami, Helium effects on recovery and recrystallization of powder metallurgically processed tungsten, Physica Scripta 2020(T171) (2020) 014016.

[3] Y. Liu, X. Liu, C. Lai, J. Ma, X. Meng, L. Zhang, G. Xu, Y. Lu, H. Li, J. Wang, S. Chen, Boriding of tungsten by the powder-pack process: Phase formation, growth kinetics and enhanced neutron shielding, International Journal of Refractory Metals and Hard Materials 110 (2023) 106049.

[4] F. Pedregosa, G. Varoquaux, A. Gramfort, V. Michel, B. Thirion, O. Grisel, M. Blondel, P. Prettenhofer, R. Weiss, V. Dubourg, J. Vanderplas, A. Passos, D. Cournapeau, M. Brucher, M. Perrot, É. Duchesnay, Scikit-learn: Machine Learning in Python, J. Mach. Learn. Res. 12(null) (2011) 2825–2830.

[5] G. Yang, R. Tao, C.J. Jafta, C. Shen, S. Zhao, L. He, I. Belharouak, J. Nanda, Investigating Multiscale Spatial Distribution of Sulfur in a CNT Scaffold and Its Impact on Li–S Cell Performance, The Journal of Physical Chemistry C 125(24) (2021) 13146-13157.

[6] C. Bonnekoh, P. Lied, S. Zaefferer, U. Jäntsch, A. Hoffmann, J. Reiser, M. Rieth, The brittle-to-ductile transition in cold-rolled tungsten sheets: Contributions of grain and subgrain boundaries to the enhanced ductility after pre-deformation, Nuclear Materials and Energy 25 (2020) 100769.

[7] X. Li, L. Zhang, G. Wang, Y. Long, J. Yang, M. Qin, X. Qu, K.P. So, Microstructure evolution of hot-rolled pure and doped tungsten under various rolling reductions, Journal of Nuclear Materials 533 (2020) 152074.

[8] A. Baserga, V. Russo, F. Di Fonzo, A. Bailini, D. Cattaneo, C.S. Casari, A. Li Bassi, C.E. Bottani, Nanostructured tungsten oxide with controlled properties: Synthesis and Raman characterization, Thin Solid Films 515(16) (2007) 6465-6469.

[9] A.T. Miyakawa, Raman Study on Sol-Gel Derived Tungsten Oxides from Tungsten Ethoxide, Japanese Journal of Applied Physics 30(8B) (1991) L1508.

[10] C. Santato, M. Odziemkowski, M. Ulmann, J. Augustynski, Crystallographically Oriented Mesoporous WO3 Films: Synthesis, Characterization, and Applications, Journal of the American Chemical Society 123(43) (2001) 10639-10649.

[11] Y. Djaoued, S. Balaji, R. Brüning, Electrochromic Devices Based on Porous Tungsten Oxide Thin Films, Journal of Nanomaterials 2012 (2012) 674168.

[12] S. Corsetti, D. McGloin, J. Kiefer, Comparison of Raman and IR spectroscopy for quantitative analysis of gasoline/ethanol blends, Fuel 166 (2016) 488-494.

[13] B. Dec, M. Ficek, M. Rycewicz, Ł. Macewicz, M. Gnyba, M. Sawczak, M. Sobaszek, R. Bogdanowicz, Gas Composition Influence on the Properties of Boron-Doped Diamond Films Deposited on the Fused Silica, Materials Science-Poland 36(2) (3918) 288-296.

[14] G. Parakhonskiy, N. Dubrovinskaia, E. Bykova, R. Wirth, L. Dubrovinsky, Experimental pressure-temperature phase diagram of boron: resolving the long-standing enigma, Scientific Reports 1(1) (2011) 96.

[15] X.-Y. Yu, T. Graening, G. Yang, and Y. Katoh, “Boron-Doped Tungsten for Fusion PFCS”, U.S. DOE Office of Fusion Energy Science, Fusion Materials, Semiannual Progress Report, DOE/ER-0313/74 (2023)

5. LIQUID METAL COMPATIBILITY

5.1 LIQUID METAL COMPATIBILITY

M. Romedenne, B.A. Pint, C. On, N.G. Russell, Y. Zhang (Tennessee Technological University)*
**romedennem@ornl.gov*

5.1.1 OBJECTIVE

Liquid metal compatibility studies consist of three separate tasks evaluating Li, Sn, and Pb-17at.%Li for various fusion blanket and plasma-facing applications. Compatibility between Li or PbLi with RAFM type steels (e.g. F82H) has been studied for many years; the current project considers the susceptibility of F82H to liquid metal embrittlement for liquid Li plasma facing components (divertor); and coated (aluminized) F82H interaction with SiC in flowing PbLi for the dual-coolant lead-lithium (DCLL) blanket concept. Characterization has been completed for the flowing Sn experiment and the project is now focused on analysis and characterization of samples tested in Sn-filled irradiation capsules exposed in HFIR.

5.1.2 SUMMARY

Following a previous thermal convection loop (TCL) experiment conducted for 1000 h and characterized in FY22, another TCL was completed in FY23 and characterization of specimens is ongoing. The TCL was fabricated from Kanthal alloy APMT (Fe-21Cr-5Al-3Mo) and used to study a variety of specimens that were pre-oxidized to form an alumina surface scale that would inhibit alloy-liquid interactions. The test was run for 2000 h to study reaction kinetics. More specifically, the TCL exposed SiC, pre-oxidized APMT coupons, and pre-oxidized and coated (pack-aluminized) F82H specimens to flowing Pb-Li with a peak temperature of 650°C. Compared to the 1000 h exposure, very limited interaction was observed between the Fe-based coupons and the SiC, suggesting the successful role of aluminized coatings and pre-oxidation in limiting the degradation and interaction of Fe-based alloys and SiC in flowing PbLi at temperatures up to 650°C for 2000 h. For Li liquid-metal embrittlement (LME), it was observed for the high strength (45 HRC) polished 4340 hollow tensile specimens, especially when the specimens were heated to 400°C for 1 h before tensile testing at 200°C. In contrast, no significant impact of Li on the tensile properties was observed for the moderate strength (23 HRC) polished F82H specimens, even after pre-exposure to liquid Li for 500 h at 500 °C. As-machined F82H specimens exhibited some sensitivity to LME, suggesting the need for further research on the influence of surface condition and/or notch sensitivity in the presence of liquid Li. Five HFIR irradiation capsules [1] (SNF01 to SNF05) were assembled, each containing two pre-oxidized oxide dispersion strengthened (ODS) FeCrAl SSJ specimens and SiC thermometry surrounded by 2 cm^3 of Sn (14.6g). All samples were exposed in HFIR for 10 days (240 h) at a target temperature of 400°C. The five capsules were successfully disassembled. Dilatometric analysis of the passive SiC thermometry indicated an irradiation temperature between 433-468°C for SNF01 and 391-431°C for SNF03. Metallographic preparation and secondary electron microscopy characterization of SNF03 is in progress.

5.1.3 PROGRESS AND STATUS

Liquid metals are being explored as a potential solution for the extreme environment at the plasma-materials interface (liquid metal plasma facing divertor). For Li, the high vapor pressure is not attractive, but compatibility is reasonably good with RAFM steels up to 600°C. Low alloyed carbon-steels (e.g. type 4340 steel) were reported to be susceptible to liquid metal embrittlement (LME) [2] and therefore is an area of concern for RAFM type steels where limited data is available. An LME evaluation and characterization of F82H (Fe-8Cr-2W) and 4340 steels was completed. In prior work, Hollow 4340 specimens were prepared using electrical discharge machining (EDM) and polished to 0.4 μm or 16 centerline average roughness

(CLA). The samples were tested and confirmed to exhibit LME in liquid Li. The fractured and polished surfaces were characterized. A second set of polished hollow F82H specimens (16 CLA) were tested and the results were compared to the unpolished hollow specimen from FY21. Three different displacement rates were used during mechanical testing: one to achieve the required strain rate at yield per ASTM E21 ($\varepsilon_1 = 5\ 10^{-3}$ min^{-1}), as well as higher and lower strain rates ($\varepsilon_2 = 5\ 10^{-2}$ min^{-1}, $\varepsilon_3 = 5\ 10^{-4}$ min^{-1}) to test the effect of strain rate. Strain rates were estimated from crosshead displacement rates. Tests were performed with Ar- and Li-filled hollow tensile specimens at 200°C with 1 h hold at 200°C (henceforth named 200/200°C) or 1 h hold at 400°C (henceforth named 400/200°C), with 1.5 to 2 h ramp to test temperature at three different strain rates ($\varepsilon_1, \varepsilon_2, \varepsilon_3$). In the present study, the 1 h hold at 400°C was used to accelerate dissolution of any surface oxide formed on the inner surface of the steel specimens before tensile testing at 200°C.

For the F82H specimens, similar results were measured for the unpolished and 16 CLA specimens in Ar or Li (Figure 44a). The results in Ar were more reproducible than the result in Li and a smaller reduction of elongation at rupture (25 ± 8 %) was measured (Figure 44a) compared to the 4340 alloy [3]. Mixed results were observed after pre-heating at 400°C for 1 h (Figure 44b). For the 16CLA specimen, similar strength and slightly lower deformation at rupture were measured in Li and Ar after pre-heating at 400°C (Figure 44d) and after pre-heating at 200°C (Figure 44b). However, for the unpolished specimen, a significant drop in elongation at rupture (70 % decrease) was observed (Figure 44b) compared to Ar. Finally, tensile testing of the pre-exposed specimen (500 h in Li at 500°C) did not result in noticeable change in strength and deformation at rupture for the F82H specimen (not shown here). Similarly, increasing and decreasing the strain rate did not result in a significant reduction in deformation at rupture in Li compared to in Ar (not shown here).

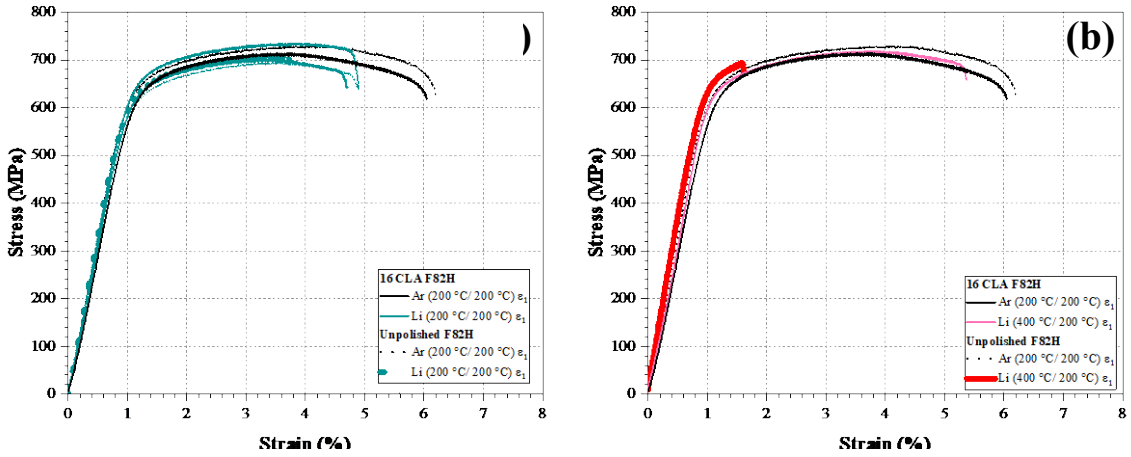

Figure 44. Stress strain curves of polished and unpolished F82H specimens during tensile testing in Ar and Li (a) 200 /200 °C and (b) 400/ 200°C at strain rate $\varepsilon_1 = 5\ 10^{-3}$ min^{-1}.

An alternative approach for this application is to use Sn, which has a much lower vapor pressure, but is known to be corrosive to most conventional alloys. In FY23, TCL specimen characterization was completed and a manuscript is being prepared. The final task was to test the performance of pre-oxidized FeCrAl in Sn at 400°C under HFIR irradiation. Five rabbit capsules [1] (SNF01 to SNF05) filled with 2 cm^3 of Sn (14.6g) and two pre-oxidized oxide dispersion strengthened (ODS) FeCrAl SSJ specimens and SiC thermometry were exposed in HFIR for 10 days (240 h) at a target temperature of 400°C. The five capsules were successfully disassembled. Analysis of the high temperature dilatometry measurements of the SiC

thermometry [4] indicated an irradiation temperature between 433-468°C for SNF01 and 391-431°C for SNF03. Metallography preparation and secondary electron microscopy characterization of SNF03 is in progress.

In FY23, the seventh Pb-Li TCL experiment also completed 2000 h with a peak temperature of 650°C and characterization of exposed specimens is in progress. Compared to the sixth TCL with a peak temperature of 650°C and 1000 h exposure, similar corrosion and interaction of the pre-oxidized and aluminized Fe-based alloys and SiC were observed (Figure 45), with transformation of α-Al_2O_3 into α and γ-Al_2O_3 on the surface of the pre-oxidized specimens after exposure to flowing PbLi (not shown here) and formation of Fe_3Si on the surface of some SiC coupons by X-ray analysis (not shown here). These results suggest the successful role of aluminized coatings and pre-oxidation in limiting the degradation and interaction of Fe-based alloys and SiC in flowing PbLi at temperatures up to 650°C for 2000 h.

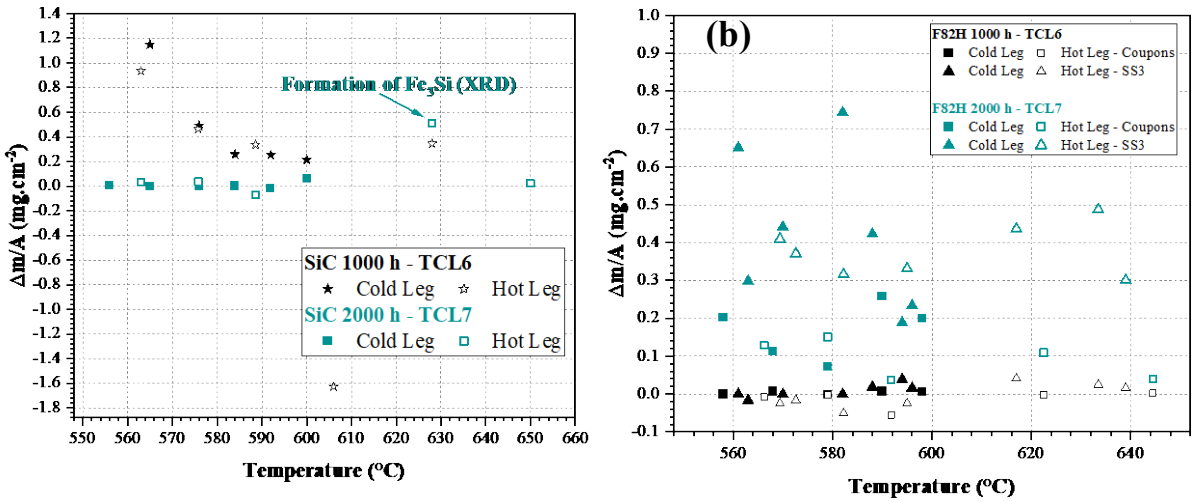

Figure 45. Mass change as function of estimated temperature in the flowing PbLi loop of (a) SiC coupons and (b) aluminized and pre-oxidized F82H coupons and SS3.

5.1.4 FUTURE RESEARCH

During FY24, the five HFIR capsules will be fully characterized using scanning electron microscopy and energy dispersive spectroscopy in LAMDA, and room temperature tensile tests will be performed in hot cells. The specimens of the TCL7 exposed for 2000 h will be characterized using XRD, secondary electron microscopy and transmission electron microscopy and the room temperature tensile tests after exposure to flowing PbLi and Ar will be analyzed.

5.1.5 REFERENCES

[1] M. Kondo, B.A. Pint, J. Jun, N. Russell, J. McDuffee, M. Akiyoshi, T. Tanaka, N. Oono, J. Miyazawa, J.W. Geringer, Y. Katoh, Y. Hatano, Conceptual Design of HFIR Irradiation Experiment for Material Compatibility Study on Liquid Sn Divertor, Plasma and Fusion Research 16 (2021) 2405040-2405040.

[2] M.G. Nicholas, C.F. Old, Liquid metal embrittlement, Journal of Materials Science 14(1) (1979) 1-18.

[3] C. Parish, C. On, Y. Kato, FUSION MATERIALS RESEARCH AT OAK RIDGE NATIONAL LABORATORY IN FISCAL YEAR 2022, United States, 2023.

[4] A.A. Campbell, W.D. Porter, Y. Katoh, L.L. Snead, Method for analyzing passive silicon carbide thermometry with a continuous dilatometer to determine irradiation temperature, Nuclear Instruments and Methods in Physics Research Section B: Beam Interactions with Materials and Atoms 370 (2016) 49-58.

6. GASSES IN MATERIALS

6.1 SIMULATING TRANSMUTATION DAMAGE TO F82H RAFM STEELS

Y. Lin, T. Byun, C. On, S. Aduloju, A. Bhattacharya (Univ. Birmingham)*
**liny@ornl.gov*

6.1.1 OBJECTIVE

This research aims to study microstructure changes in HFIR-irradiated F82H reduced activation ferritic-martensitic (RAFM) steels (doped with 1.4% ^{58}Ni or ^{60}Ni) induced by neutrons and helium, understanding their impact on mechanical properties. The focus is on quantifying helium-induced degradation, developing a model for evaluation of low-temperature hardening embrittlement, and creating a foundational basis for assessing the performance degradation of RAFM steels due to irradiation and helium exposure through structural analysis and stress-strain curve inputs.

6.1.2 SUMMARY

Following neutron irradiation at HFIR up to 86 dpa and 300°C, cavities were observed in the isotopically doped F82H steel (F82H-Ni58 and F82H-Ni60) samples. F82H-Ni58 showed higher cavity density with an elevated He per dpa ratio (11 appm He/dpa) compared to F82H-Ni60 (0.3 appm He/dpa). Notably, no distinct bimodal cavity size distribution was evident in either sample. Both materials exhibited Ni-rich clusters due to irradiation-induced or -enhanced precipitation, including small, spherical Ni- or Cr-rich particles and larger, rod-shaped clusters enriched in Ni and Cr. Ni/Cr segregation was noticed at grain boundaries and around cavities in both samples. Furthermore, the primitive $M_{23}C_6$ carbide particle showed a sponge-like structure, suggesting potential neutron irradiation effects on these precipitates. According to the dispersed barrier hardening model estimation, F82H-Ni58 displays lower contributions of obstacles except cavities compared to F82H-Ni60, indicating that the He effects on cavities play a more significant role in low-temperature hardening effects (LTHE) at higher He/dpa.

6.1.3 PROGRESS AND STATUS

RAFM steels are the leading candidates for fusion reactor components owing to their advantageous thermo-mechanical properties and established radiation tolerance. However, achieving fusion-relevant helium generation rates in these steels is challenging without fusion prototypic neutron sources. Yet, utilizing isotopically tailored methods in the mixed-energy neutron spectrum at HFIR presents a feasible solution. At LAMDA, ORNL, our study involved TEM characterizations of HFIR-irradiated F82H steel doped with 1.4% 58Ni and 1.4% 60Ni to examine helium's impact [1]. The 1.4% 58Ni-F82H steel produced approximately 936 appm helium (~11 appm He/dpa), while the 1.4% 60Ni-F82H steel yielded about 26 appm helium (~0.3 appm He/dpa) for doses up to 86.17 dpa.

Post-neutron irradiation, STEM-BF imaging revealed cavities in both the F82H-Ni58 and F82H-Ni60 samples (Figure 46). F82H-Ni58 showed a higher cavity density with an elevated He per dpa ratio (11 appm He/dpa) compared to F82H-Ni60 (0.3 appm He/dpa). Notably, neither sample displayed a bimodal cavity size distribution, likely due to the intricate microstructural changes occurring under neutron irradiation, affecting sink strength, and blurring the critical radius boundary between bubbles and voids.

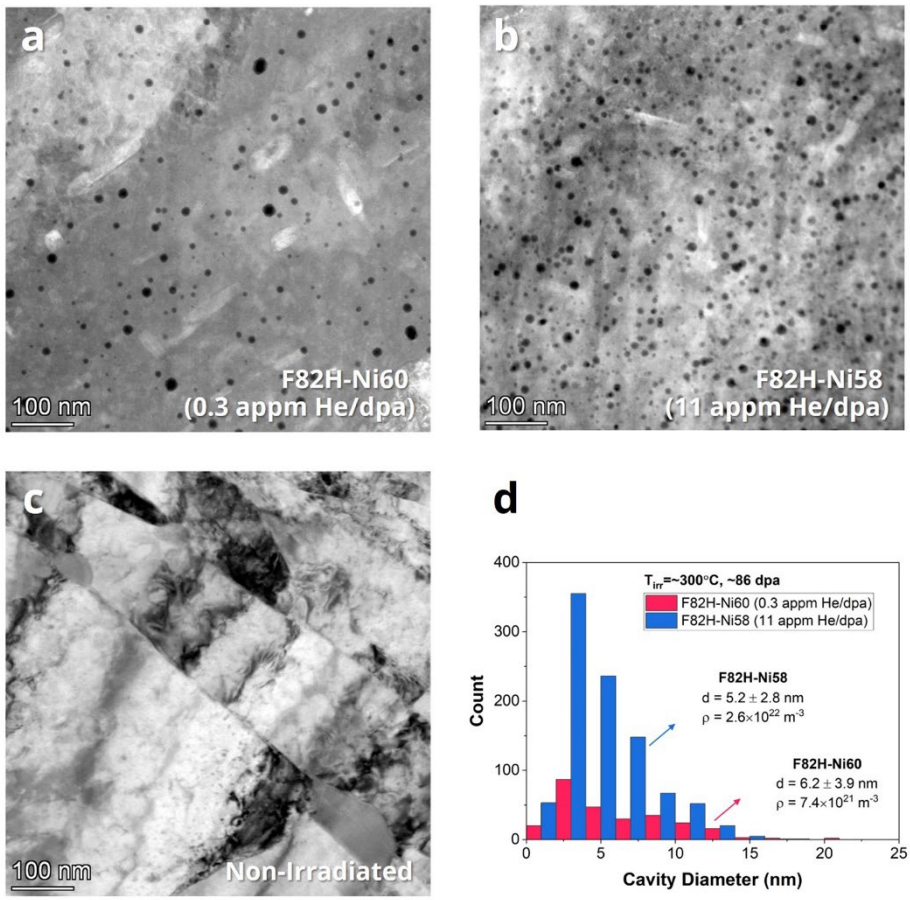

Figure 46. STEM bright-field images of cavities in (a) F82H-Ni60 and (b) F82H-Ni58; (c) STEM bright-field image of the non-irradiated F82H sample with no cavities observed; (d) Size distribution of cavities in F82H-Ni60 and F82H-Ni58.

STEM energy dispersive X-ray spectroscopy (EDS) mapping unveiled Ni/Cr-rich precipitates and clusters in both irradiated samples absent in the non-irradiated sample [1]. These are likely a consequence of irradiation-induced or enhanced precipitation, encompassing small, spherical Ni- or Cr-rich particles, and larger, rod-shaped clusters enriched in Ni and Cr. The large Cr-rich particles in the non-irradiated F82H sample are primitive $M_{23}C_6$ particles. Despite a sponge-like structure in the $M_{23}C_6$ particle after irradiation, there was no evidence of amorphization or phase transformation based on the selected area electron diffraction (SAED) pattern before and after irradiation. Further STEM-EDS mapping near the grain boundary revealed Ni/Cr segregation in both neutron-irradiated F82H materials, in line with the concept of radiation-induced segregation (RIS). The observed Ni segregation around cavity surfaces has the potential to enhance the strengthening coefficient of cavities, subsequently increasing irradiation hardening.

The quantification of all irradiation-induced microstructures, encompassing cavities, dislocations, dislocation loops, and precipitates through the modeling of dispersion hardening in the irradiated Ni-doped F82H steels (refer to Figure 47), indicates that the heightened density of cavities in the F82H-Ni58 sample, in conjunction with a higher helium production rate of 11 appm He/dpa compared to 0.3 appm He/dpa in F82H-Ni60, is likely the primary factor contributing to the observed additional increase in yield strength during tensile tests [1]. This suggests that cavities, influenced by the He/dpa ratio, play a notably more

substantial role in LTHE compared to other microstructures. The cavities (helium bubbles) can contribute to the low temperature embrittlement via multiple mechanisms, such as the dispersion hardening mechanism and weakening of boundary bonding by a preferred distribution of cavities at the boundaries.

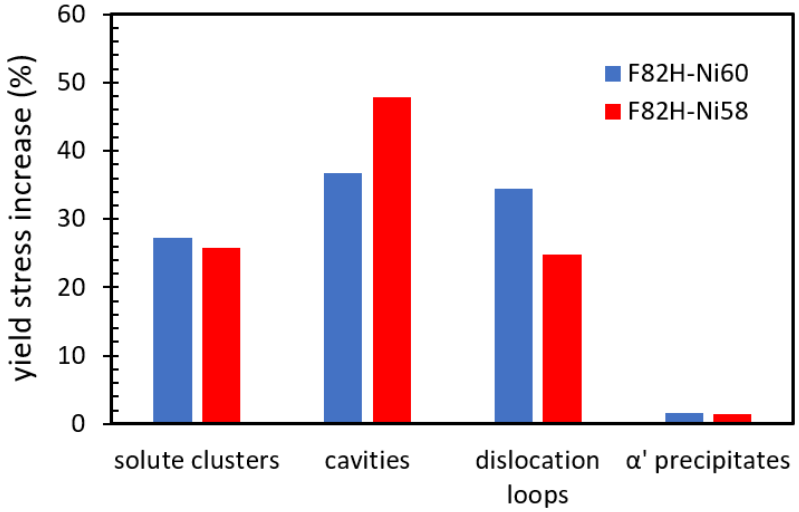

Figure 47. Hardening contributions of irradiation-induced nanoscale features in high and low transmutation F82H steels.

6.1.4 FUTURE RESEARCH

A manuscript outlining the current study on neutron-irradiated F82H is currently underway and is nearing submission to a peer-reviewed journal. Future research will focus on post-irradiation examination of the same F82H materials irradiated at the same temperature but lower doses. This is intended to confirm the combined effects of helium and displacement damage on mechanical property changes and improve a mechanical threshold stress (MTS) crystal plasticity constitutive model.

6.1.5 REFERENCES

[1] Y. Lin and T. Byun, “Impact of Helium on the Neutron Irradiation Response of Isotopically Tailored F82H RAFM steel to 86 dpa, U.S. DOE Office of Fusion Energy Science, Fusion Materials, Semiannual Progress Report, DOE/ER-0313/74 (2023)

6.2 DEUTERIUM RETENTION AND DESORPTION BEHAVIORS IN FUSION BLANKET STRUCTURAL MATERIALS AND MODEL ALLOYS

*W. Zhong**
**zhongw@ornl.gov*

6.2.1 OBJECTIVE

This goal of this work is to investigate how intrinsic microstructure in reduced activation ferritic martensitic (RAFM) steels alter the hydrogen retention behavior. In this work, we have investigated the microstructure and hydrogen retention in castable nanostructured alloys (CNAs) and model alloys that are subjected to different heat treatments to change the microstructure and hydrogen trapping-site density.

6.2.2 SUMMARY

Thermal desorption experiments were performed on the CNAs with different carbon contents, aged CNAs, and the model binary Fe-9Cr alloys. The microstructures of these alloys were analyzed using electron back-scattered diffraction (EBSD) and transmission electron microscopy (TEM) to characterize the potential hydrogen trapping sites. The results in this work demonstrate that hydrogen trapping increases in the order of microstructural complexity. In addition, low carbon CNAs show similar hydrogen trapping as high carbon CNAs, which was also observed after the thermal aging of these two alloys. Such observation combining the microstructural observation suggests stronger hydrogen trapping by TiC than $Cr_{23}C_6$ precipitates.

6.2.3 PROGRESS AND STATUS

To investigate the effect of the microstructure features to hydrogen retention and desorption behavior, CNAs and binary Fe-9Cr alloys have been subjected to different heat treatment to change the intrinsic microstructure. EBSD and TEM have been performed on these alloys, with examples shown in Figure 48, including binary Fe-9Cr alloys of coarse equiaxed grains, Fe-9Cr alloy after heat treatment, high carbon CNAs, low carbon CNAs and aged CNAs. Figure 48 illustrates the grain structure, precipitate distribution, and the kernel average misorientation (KAM) that is a surrogate metric of the dislocation density. In KAM maps, misorientations are shown in rainbow color scheme, with increasing order of blue, green, yellow and red.

CNAs demonstrate tempered martensite grain structure. The aging has reduced KAM, which is expected from the high temperature annealing. Although TEM has not been performed on aged CNAs, coarser particles with lower number density of both $Cr_{23}C_6$ and MX precipitates are expected from the thermal aging effects. On the other hand, no precipitates are expected from the binary alloy Fe-9Cr. Heat treatment of Fe-9Cr leads to high dislocation density as shown in green color in the KAM maps, while Fe-9Cr coarse grain exhibits low dislocation density.

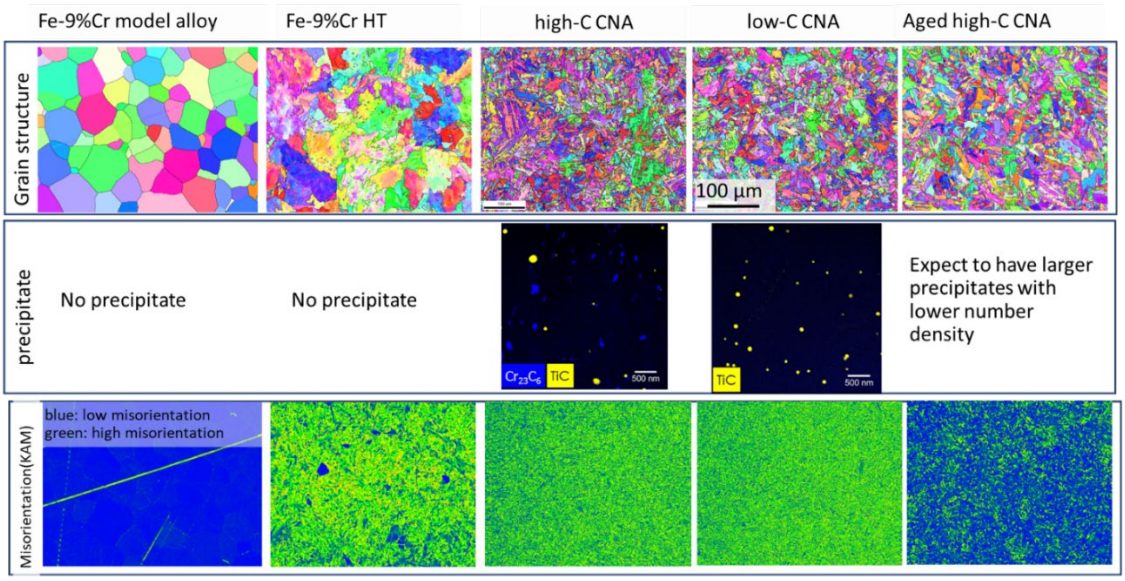

Figure 48. EBSD and TEM images to show the grain structure, preciptiate distribution and kernal average misorientation.

Hydrogen desorption experiments were performed immediately on these alloys after hydrogen charging for 1 hour at 450°C. The total hydrogen retentions were measured and are shown in Figure 49. The x-axis is arranged in the order of microstructure complexity. Hydrogen retention increases as the microstructural complexity increases. Although high-carbon CNAs have additional precipitates ($Cr_{23}C_6$) compared with low carbon CNAs, the difference between these two alloys are small, indicating possible minor effects of $Cr_{23}C_6$ on hydrogen trapping in CNAs, as compared to TiC precipitates.

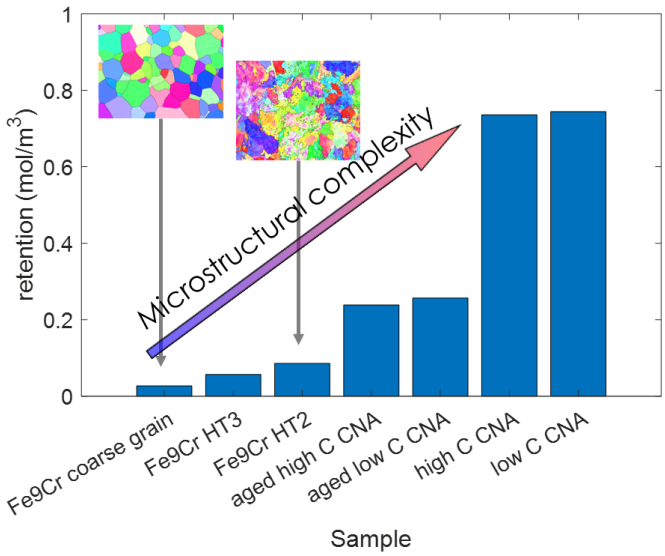

Figure 49. Calculated deuterium retention in various CNAs and binary Fe-9Cr alloys.

6.2.4 FUTURE RESEARCH

Atom probe tomography will be pursued to observe the hydrogen trapping in CNAs.

7. ADVANCED MANUFACTURING

7.1 ADDITIVE MANUFACTURING OF SiC FOR FUSION APPLICATIONS: PHASE SEPARATION DURING POWDER BED FUSION PROCESSING OF SiC

B. W. Lamm, T. Koyanagi*
**lammbw@ornl.gov*

7.1.1 OBJECTIVE

Powder bed fusion (PBF) of SiC is under study as a method of fabricating complex structural components for fusion. This study investigated the binding of particles after PBF to identify the materials present in the interparticle space.

7.1.2 SUMMARY

Solidification processes of PBF of SiC powders were uncovered by microscopy and thermodynamics. Analysis of PBF-printed SiC samples identified the formation of new phases (Si, C, and nanocrystalline SiC) within the spaces between SiC powder particles. Comparisons of the observed phase changes to calculated phase diagrams resulted in identification of a likely formation mechanism. These new phases are expected to be detrimental to the chemical and mechanical stability of SiC components in a fusion reactor environment.

7.1.3 PROGRESS AND STATUS

A series of SiC samples were produced by selective laser sintering, a type of powder bed fusion (PBF) additive manufacturing. PBF printing of SiC is of interest to produce complex components that are not practical or not feasible to produce by conventional means, specifically for fusion structural applications.

Close examination of the particle joins by transmission Kikuchi diffraction (TKD) and energy dispersive spectroscopy (EDS), shown in Figure 50, identified additional material phases along with the original SiC particles. Comparison of the EDS maps and TKD maps identified carbon in the black undefined regions of the TKD maps (example.g., Box 1 in Figure 50B), 6H-SiC in the red regions (Box 2 in Figure 50A), 3C-SiC in the all-yellow regions (Boxes 3 and 4 in Figure 50A and B, respectively), and a mixture of Si and 3C/6H-SiC in the mixed red/yellow regions (Boxes 5 and 6 of Figure 50A and B, respectively).

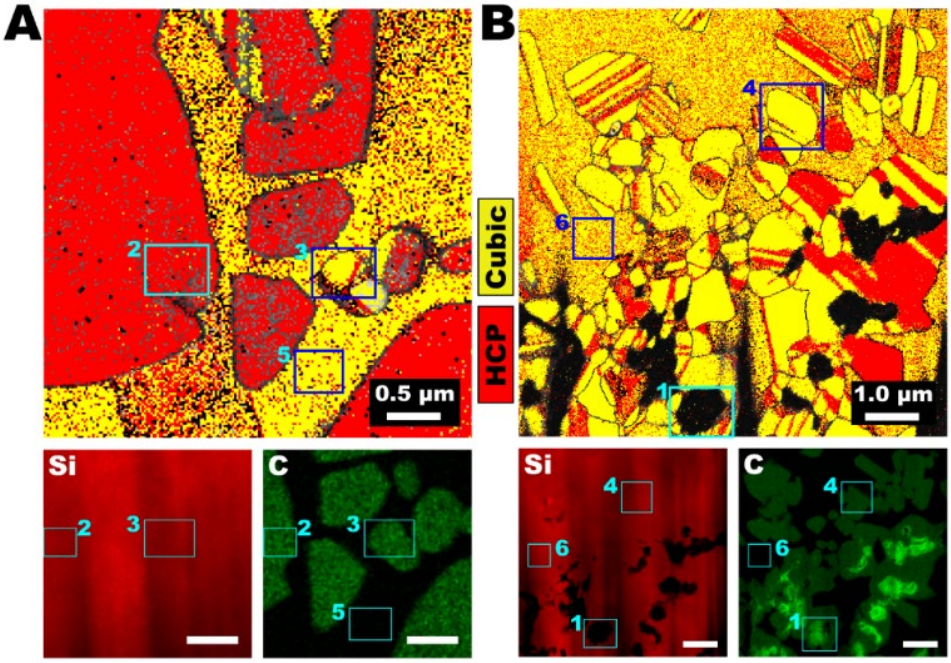

Figure 50. Silicon-rich (A) and carbon-rich (B) samples characterized by TKD (top) and EDS (bottom). TKD maps are phase-colored by cubic (yellow) and hexagonal close-packed (red). EDS element maps indicate silicon (red) and carbon (green). Scale bars are 0.5 µm (A) and 1.0 µm (B). Regions of interest are highlighted by boxes to indicate areas assigned as 1. carbon, 2. 6H-SiC, 3/4. 3C-SiC, and 5/6. Si with possible nano-SiC precipitate.

To better understand the phase changes observed in the PBF SiC samples, the experimental results were compared to calculated phase diagrams (Figure 51). From the calculated SiC phase diagram, it was observed that SiC remains solid at 1 atm until heated to 2823°C. Above this temperature, a liquid melt forms composed of liquid silicon and solid carbon. This incongruent melt transition temperature is constant with pressure down to ~0.8 atm and up to at least 30 atm (the highest pressure simulated in this study). The composition of the gas was calculated to be consistent regardless of temperature or pressure. The primary constituent (~50 mol%) was SiC_2, followed by either Si_2C or Si, where both compounds could range from 20-25 mol%. As temperature increases, the amount of Si increases, decreasing the amount of Si_2C present. The remainder of the gas consists of oligomers of Si or C, all at ≤2 mol%. By 2879°C (phase line labeled 'graphite'), all solid species have volatilized. Decreasing pressure to <0.8 atm eliminates the liquid phase region, indicating that silicon is vaporized at the phase line labeled "SiC / gas" leaving solid graphite until temperatures increase to the "graphite" phase line.

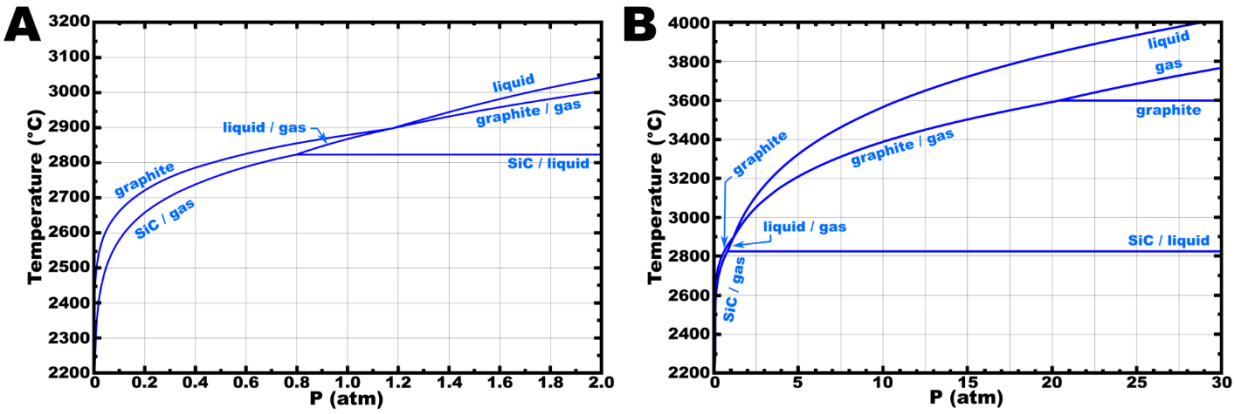

Figure 51. Temperature-pressure phase diagram for the Si-C binary at Si/(Si+C) of 0.5. The diagrams span (A) temperature T = 2200-3200°C and pressure P = 0-2 atm; (B) T = 2200-4000°C and P = 0-30 atm.

From the phase diagram comparison, it is likely that the SiC particles were joined by forming an incongruent melt of SiC (i.e., liquid Si and solid C) which quenched rapidly as the laser continued along the printing raster path. Rapid solidification of Si with a suspension of C allowed little time to reach the equilibrium phase (SiC), trapping the phases as mostly distinct materials – free Si and C.

7.1.4 FUTURE RESEARCH

The results of this work are currently under peer review in a journal article submission. Future work on the PBF of SiC will investigate ways to minimize the phase separation characteristics of SiC by altering laser print parameters and post-print processing steps. The densification of printed components is also of interest and will be investigated further.

8. COMPUTATIONAL MATERIALS SCIENCE

8.1 PLASMA MATERIAL INTERACTIONS - DEUTERIUM INTERACTION WITH TUNGSTEN SURFACE AS A PART OF MPEX DIGITAL TWIN DEVELOPMENT

Y. N. Osetskiy, G. D. Samolyuk*
**osetskiyyn@ornl.gov*

Supported by Validated Design and Evaluation of Fusion Wall Components LDRD initiative (# 10790).

8.1.1 OBJECTIVE

Material Plasma Exposure eXperiment (MPEX) is planned to be the main experimental tool to be used in Oak Ridge National Laboratory for investigating processes during plasma-materials interactions (PMI) relevant to the fusion reactor conditions. The MPEX digital twin initiative aims to develop an interlinked set of software to accelerate PMI science understanding and accelerate MPEX commissioning in achieving reactor-relevant fluences. The main objective of this task is to substitute oversimplified binary collision approximation (BCA) for the interaction of deuterium (D) with plasma facing materials, used so far, by the more realistic atomistic multibody modeling approach using classical and *ab initio* molecular dynamics.

8.1.2 SUMMARY

The interaction of D with the tungsten (W) surface was investigated using classical molecular dynamics (MD). Different target surfaces – (001), (011) and (111) – and different ion impact angles, close to the normal angle θ 12°, medium angle θ ≈ 46°, and close to the along-surface direction θ ≈ 80°; see Figure 52 (a) where the simulation cell is depicted. Because modelling and predicting plasma–material interactions (PMI) require considering a tremendous number of single plasma particle–surface interaction events, this type of modelling was, until recently, possible only within a binary collision approximation (BCA). The BCA approach considers materials as uniform temperature-insensitive media. The research presented here addresses the PMI problem within an atomistic-based approach for the first time at a statistically significant level. Approximately 10^5 molecular dynamics trajectories were generated for 100 eV deuterium ions interacting with a tungsten surface. The research demonstrated the critical importance of incorporating the discrete lattice structure of matter into the model. Deuterium penetration depth and fraction of backscattered deuterium ions strongly depend on the surface orientation, the incident ion impact directions, and the ions' initial positions. On average, the BCA-based calculations underestimate the penetration depth by a factor of two or more, and the fraction of backscattered atoms is overestimated by a factor of two or more. Furthermore, increasing the material temperature from 500 to 3000 K reduces penetration depth by about 30% and increases the fraction of backscattered atoms by 250%. The results were published [1].

8.1.3 PROGRESS AND STATUS

8.1.3.1 Surface structure effects

These were studied by initiating D-ions trajectories from the different positions along the impact surface. In total, 36 initial positions where investigated, with ~150-200 different trajectories started at different simulation time moments to accumulate statistics related to the atomic vibrations. An example of initial positions grid is presented in Figure 52b for the (001) impact surface.

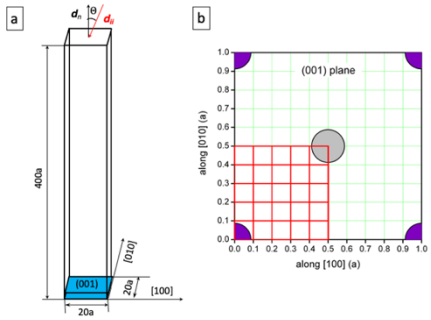

Figure 52. Schematic representation of the system for modeling deuterium interaction with (001) tungsten surface. (a) Modelled cell with sizes (*a* is the tungsten matrix equilibrium lattice parameter) in all directions and directions of the incident surface normal (d_n), ion velocity direction (d_{ii}) and incident angle (θ); (b) 2D view of the elementary cell surface fragment with the 6 × 6 grid (red lines) of the 36 tested initial deuterium ion positions.

Figure 53 shows final *z*-positions (*l*) of deuterium ions for trajectories with θ ≈ 12° and incident surface S = (001) of all the trajectories modelled at 500K. According to the method applied for trajectory counting, data between the two neighbouring vertical pink lines belong to the same line of initial positions along the [100] direction presented in Fig. 1b. Thus, trajectories counted from 1 to 870 include 145 trajectories for each of six starting positions (0.0, 0.0), (0.1, 0.0), (0.2, 0.0), (0.3, 0.0), (0.4, 0.0), and (0.5, 0.0), as indicated in Fig. 1b. Trajectories counted from 871 to 1740 correspond to the next six positions shifted along the [010] direction by 0.1*a*. The crystal lattice effect is clear: trajectories started near (0.0, 0.0) position (i.e., trajectories 1–145) collide with the nearest tungsten atom below and thus do not penetrate deep, whereas trajectories started near (0.5, 0.0) (i.e., trajectories approaching 870) have high probability for channelling and deep penetration. Most trajectories started near the centre of the position grid in Figure 52b (i.e., between (0.2, 0.2) and (0.3, 0.3) in local coordinates (i.e., trajectories between ~1500 and ~3500), have higher probability for deep penetration. When the initial position approaches (0.5, 0.5), the probability of collisions increases with decreasing penetration depth. Accounting for the target atoms' thermal vibrations introduces some stochasticity; however, the major crystallographic effects are maintained. These effects depend on the incident ion velocity vector and the surface structure (i.e., θ and S) and vary for different combinations.

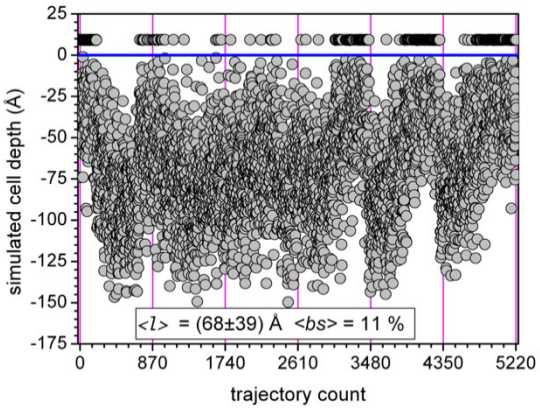

Figure 53. Final *z*-coordinate for all ions implanted at θ ≈ 12° and onto S = (001). According to Fig. 8b, trajectories are counted along the [1 0 0] direction from (0.0, 0.0) to (0.5, 0.0) and followed the 0.1*a* step increase along the [0 1 0] direction.

As shown in Figure 53 and Figure 54, the crystallographic effects correlate: the penetration depth is large when backscattering is low. The inset in Figure 54 presents the next level of statistical treatment: an average over the incident ion initial position.

8.1.3.2 Impact angle effects

Distributions like the one presented in Figure 54 were also modelled for incident angles θ ≈ 46° and θ ≈ 80° and (001), (110) and (111) planes. The results for the trajectories with impact angle θ » 12° and 46° onto all studied planes are shown in Figure 54. For θ » 12°, channelling events are more frequent for the (001) and (111) planes, whereas they are less probable for the (110) plane. For θ » 46°, the opposite is observed: more channelling occurs for the (110) plane and much less for the (001) and (111) planes. Insets in Figure 54 demonstrate the next level of statistical treatment: averaging over the incident planes. At this level, the incident angle affect becomes visible: increasing θ from 12° to 46° decreases the mean penetration depth < *l* > from 63 to 45 Å and increases the fraction of backscattered ions <*bs*> from 14% to 27%.

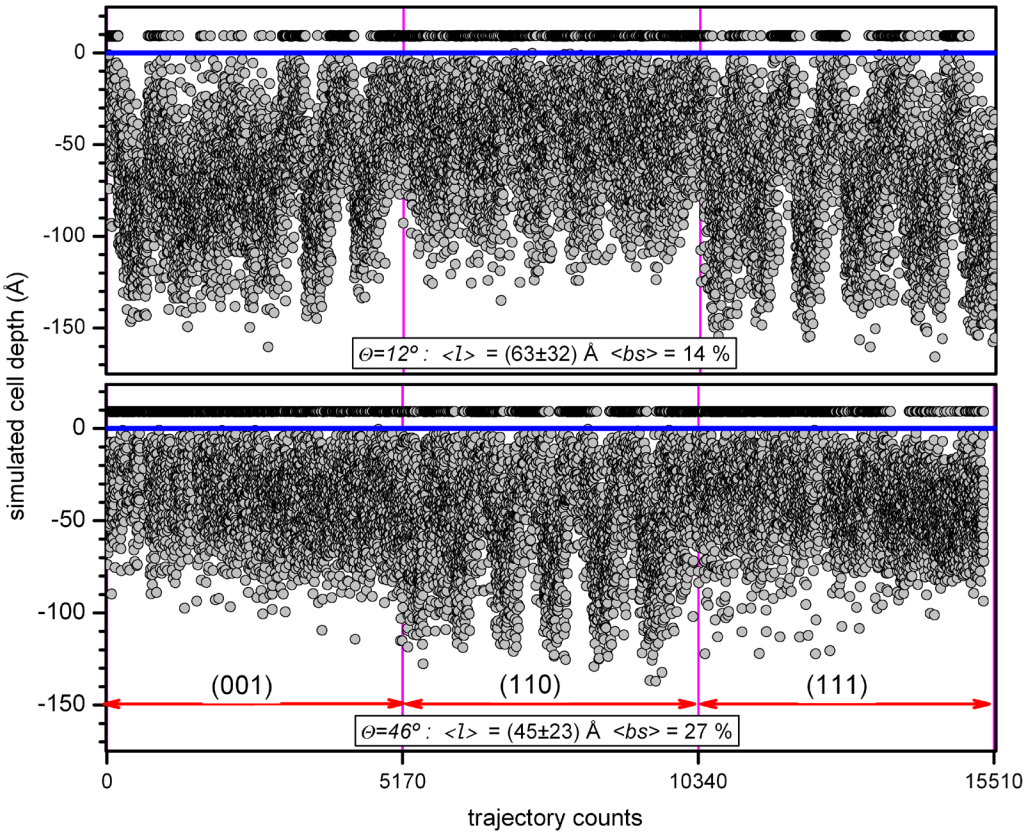

Figure 54. Final *z*-coordinate for all ions implanted at θ ≈ 12° (top) and 46° (bottom) onto (001), (110) and (111) surfaces. Groups of trajectories onto different surfaces are indicated. Insets show

the global mean values of the penetration depth and the fraction of backscattered ions for each incident angle.

All results on the statistical treatment of the incident deuterium ions mean penetration depth $< l >$ and backscattering fraction $<bs>$ obtained here by MD and BCA modelling are presented in Table 6. The global average values presented in the table are the highest level averages of the MD data that can be compared with BCA modelling for the corresponding incident angles θ.

Table 6. Results of treatment of all trajectories for each set of deuterium–tungsten interactions modelled at 500 K. Penetration depth and backscattered fraction for two modelling approaches are shown: MD with ESP and MD without ESP (in parentheses). MD with ESP global average values are obtained by treatment of all trajectories for all the studied surfaces for the given incident angle.

θ (°)	MD modelling with the incident surface			MD+ESP global average	SRIM	TRIDYN
	(001)	(110)	(111)			
Mean penetration depth, $< l >$ (Å)						
12	68 (253)	48 (181)	72 (230)	63 ± 32	28 ± 16	22 ± 8
46	39 (151)	52 (192)	42 (163)	45 ± 23	27 ± 15	18 ± 7
80	0	0	0	0	25 ± 14	9 ± 3
Mean fraction of backscattered incident ions, $<bs>$ (%)						
12	11 (16)	18 (36)	14 (19)	14	48	59
46	32 (59)	25 (39)	24 (36)	27	57	67
80	100	100	100	100	74	94

8.1.3.3 Temperature effects

Besides the extensive modelling of deuterium ion trajectories in the 500 K tungsten target, temperature effects were modelled over the range of 500–3500 K for the case of θ ≈ 12° and S = (001). Generally, increasing target temperature weakens the lattice structure. The strong dependence of deuterium ion penetration depth on the initial position is observed at 500 K, it weakens at 2000 K and it is nearly eliminated at 3000 K. This dependence affects the mean penetration depth and fraction of backscattered

atoms: < *l* > decreases, whereas <*bs*> increases. A summary analysis of the temperature effects is shown in Figure 55: a non-uniform shape of the temperature dependence of both < *l* > and <*bs*> is evident. Deuterium ion penetration is relatively weakly dependent until ~1300 K, followed by a substantial change above ~1500 K.

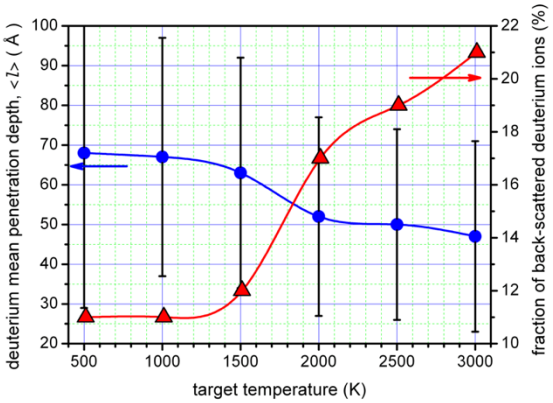

Figure 55. Temperature dependence of the mean penetration depth < l > and backscattered ion fraction <bs>. Error bars indicate standard deviation of the mean penetration depth.

8.1.4 SUMMARY

This research demonstrates the necessity of an atomistic approach to modelling PMIs. Here, ~10^5 trajectories of 100 eV deuterium ions implanted at different angles onto different tungsten target surfaces at different temperatures were modelled via MD simulations, and the results on the penetration depth and backscattered ions were statistically treated at different levels.

- The lowest level treatment enabled accounting for thermal atomic vibrations. The next level treated the non-uniform distribution of trajectory properties caused by the crystallographic features of incident surface. The highest level averaged the different incident planes and produced the overall output for particular incident angle that can be compared with BCA modelling.
- Each level allowed for investigating different effects of the crystal lattice structure on the ion–target interactions and elucidated the origin of differences in trajectory properties modelled by many-body interactions at the atomistic level and by BCA.
- Overall, MD simulations result in deeper trajectories and a lower fraction of backscattered ions, and the difference is about a factor two for small to medium implantation angles compared with BCA approximations. At large angles, the difference can be qualitative because the atomistic approach results in more intense reflection.
- Increasing temperature results in decreased penetration depth and increased backscattering fraction, and these effects are more noticeable above ~1300 K.
- General aspects of developing and using a database of plasma ions' trajectory characteristics for improving the accuracy of predictive modelling of PMI in practical applications are discussed.

8.1.5 REFERENCES

[1] D. Samolyuk, E. Zarkadoulaa, C. Lau, A. Kumar, J. Rapp, M. Eisenbach, Y. Osetskiy, Crystallographic and temperature effects in low-energy collisions for plasma–material interactions, Materialia, 32 (2023) 101886.

8.2 MECHANICAL PROPERTIES AND RADIATION EFFECTS IN FUSION MATERIALS

Y. N. Osetskiy, G. D. Samolyuk*
* *osetskiyyn@ornl.gov*

8.2.1 OBJECTIVE

The objective of this task is to obtain a better understanding of the atomic-scale mechanisms operating in fusion materials. Two main groups of effects are under consideration: mechanisms of radiation damage and properties of irradiated materials. The main materials studied are ferritic and tungsten-based alloys.

8.2.2 SUMMARY

An extensive atomic–scale study was carried out to investigate the detailed mechanisms of dislocation dynamics in the environment of radiation-induced obstacles in ferritic alloys and tungsten. Interactions between a moving ½<111>{110} edge dislocation and spherical obstacles in the size range 1 to 9 nm diameter were modeled by molecular dynamics. At this stage, we investigated processes at 300 K in Fe and 600 K in W which are the same homologous temperatures $T_H \approx 0.16T_M$ for these materials (T_M is the corresponding melting temperature) . Physical parameters of the computational model such as dislocation length and density, strain rate, and their effects on the accuracy and uncertainty of simulation results were investigated. The main aim was to obtain and compare obstacle strength parameters for different obstacles for application within the dispersed barrier hardening (DBH) model. In the first stage, we obtained and compared parameters for voids, He-filled bubbles, Cu-precipitates and rigid obstacles in Fe and voids and Re-precipitates in W.

8.2.3 PROGRESS AND STATUS

Interactions between the moving ½<111> {110} edge dislocation and spherical obstacles were modeled by molecular dynamics (MD) using the atomic scale model developed in [1]. This model considers the dynamics of a periodic array of dislocations and obstacles. In this, the main parameter is the dislocation length, *L*, which is equivalent to the distance between obstacles along the dislocation line direction <112>. This distance should be long enough to reproduce the correct dislocation line shape at the critical resolved shear stress (CRSS), τ_c. CRSS is defined as the maximum shear stress which usually occurs just before the dislocation is released from the obstacle. For strong obstacles, like voids, rigid inclusions, and some precipitates interacting with edge dislocations, the dislocation line shape corresponding to CRSS usually presents an extended dipole of screw dislocation segments formed in the obstacle's vicinity [1]. In this study, the same dislocation segment length, *L*=42 nm, was used for all obstacles to ensure the correct comparison of CRSS for different obstacles and sizes. This length is significantly longer than the largest simulated obstacle diameter, *D*=9 nm. Depending on the obstacle size the modeled system contained from ~2M to above 8M mobile atoms. In bcc Fe we simulated voids, He-filled bubbles with the vacancy/He ratio 0.5, initially coherent Ce-precipitates, and rigid inclusions to simulate oxide particles. In W we simulated voids and coherent Re-precipitates. Two types of precipitates were modeled, 100 at.%Re and 50 at.% Re randomly distributed within the spherical volume of diameter *D*.

The current atomistic modeling of the periodic array of dislocations and obstacles is fully consistent with Bacon-Kocks-Scattergood (BKS) continuum modeling [2,3]. The atomistic modeling results were fitted to the following expression for CRSS (omitting the Taylor factor):

$$\tau_c = A\frac{\mu b}{L}[ln(D^{-1} + L^{-1})^{-1} + B] \qquad (1)$$

were $A = 1/2\pi$ and $A = 1/2\pi(1-\nu)$ for edge and screw dislocations respectively, μ and ν are the shear modulus and Poisson ratio respectively. B is a constant characterizing the interaction between the dislocation and matrix-obstacle interface and is related to the obstacle-matrix interface energy. Here we use B as a parameter to adjust the CRSS level to modeling results.

MD values obtained for CRSS, in units ($\mu b/L$) are presented as a function of the harmonic mean $(D^{-1}+L^{-1})^{-1}$ (D and L are in units of the Burgers vector b) in Figure 56. This shows that the modeling results are quite well described by the BKS model. The interesting case is Cu-precipitates in Fe. It was observed that initially coherent with the bcc matrix precipitates with $D \geq 6$nm during interaction with intersecting dislocation transform towards fcc structure. This transformation changes the CRSS(D) dependence as shown in Figure 56a.

The data presented in Figure 56 can be used to calculate strength parameters that can be used in estimating mechanical properties response via the widely used dispersed-barrier hardening (DBH) model that describes CRSS increase from localized obstacles with a density N and a mean diameter D as:

$$CRSS = M\alpha\mu b\sqrt{ND}, \quad (2)$$

where M is the Taylor factor that we omit here like in the eq. (1), and α is the obstacle strength parameter. Here $1/\sqrt{ND}$ is an estimation of the mean distance between obstacles, which, in the current approach, is equal exactly to the modeled dislocation segment length L. Combining eq. (1) and (2) one can get the expression for the strength parameter:

$$\alpha = A[ln(D^{-1}+L^{-1})^{-1}+B] \quad (3)$$

Note, that coefficient A in eq. (4) is different for different obstacles, as indicated by the results fitting presented in Figure 56 by solid lines. In the case of reasonably low obstacle density, $L>>D$, eq.(4) can be simplified to:

$$\alpha = A[ln(D)+B] \quad (4)$$

Table 7 presents the expressions for calculating the strength parameter for different obstacles and particular values of α calculated for the relevant sizes. One can see that the obstacle strength is size dependent, which is usually not taken into account. The logarithmic dependence on the obstacle diameter is not a strong function, however, α increases by >3 times when the obstacle diameter changes from 2 nm to 20 nm. This might induce quite a significant difference to the strengthening compared with estimations using the size-independent α. An example of size dependence for obstacles in Fe is presented in Figure 57. One can see that the overall change in the α values is quite significant and should not be ignored.

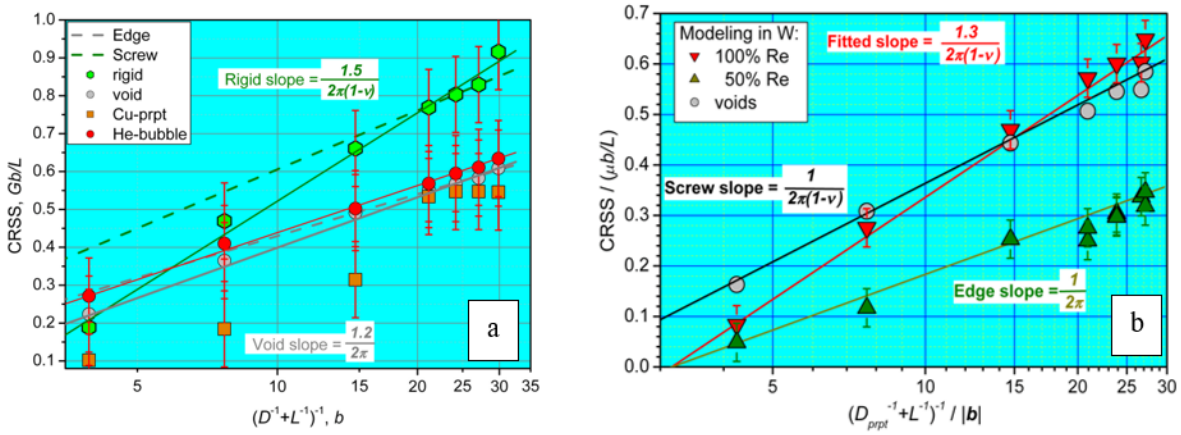

Figure 56. MD derived CRSS for different obstacles in (a) Fe at 300K and (b) W at 600 K as a function of the obstacle size *D* and spacing *L*.

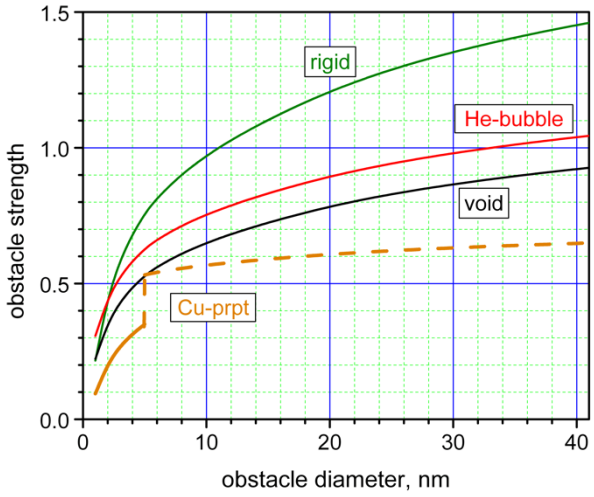

Figure 57. Size dependence of the strength parameter for different obstacles in Fe.

8.2.4 FUTURE PLANS

This study will be continued modeling other obstacles in W such as Re-rich precipitates and other materials and environmental conditions such as temperature, strain rate and multiple obstacles. Contribution from thermally activated processes will be also studied. The final aim is to obtain a robust approach for estimation mechanical properties change in irradiated W-based materials.

Table 7. Expressions for estimating obstacle strength parameter α for different obstacles in Fe (300K) and W (600K) and particular values for obstacles of different sizes. The core radius of the

½<111> dislocation is taken as its Burgers vector length $r_0 = \frac{\sqrt{3}}{2}a$, where a is the lattice parameter in Fe and W for the corresponding T.

matrix/obstacle	α	2nm	5nm	10nm	20nm
Iron:					
rigid	$0.336\left[ln\left(D_{prpt}/r_0\right) - 0.75\right]$	0.45	0.76	0.99	1.22
void	$0.190[ln(D_{void}/r_0) - 0.22]$	0.35	0.53	0.66	0.79
Bubble	$0.199[ln(D_{bubble}/r_0) + 0.15]$	0.45	0.63	0.77	0.90
Cu-prpt (small)	$0.159\left[ln\left(D_{prpt}/r_0\right) - 0.80\right]$	0.20	0.35		
Cu-prpt (large)	$0.056\left[ln\left(D_{prpt}/r_0\right) + 6.50\right]$			0.57	0.61
Tunrgsten:					
50at.% Re	$0.159\left[ln\left(D_{prpt}/r_0\right) - 1.15\right]$	0.13	0.28	0.39	0.50
Void	$0.221[ln(D_{void}/r_0) - 0.68]$	0.29	0.49	0.65	0.80
100at.% Re	$0.287\left[ln\left(D_{prpt}/r_0\right) - 1.15\right]$	0.24	0.50	0.70	0.90

8.2.5 REFERENCES

[1] Y.N. Osetsky and D.J. Bacon. An atomic-level model for studying the dynamics of edge dislocations in metals. Modelling Simul.Mat.Sci.Eng. 11 (2003) 427.

[2] D. J. Bacon, U. F. Kocks and R. O. Scattergood. The effect of dislocation self-interaction on the Orowan stress, Philos. Mag., 28 (1973) 1241-1263.

[3] R.O. Scattergood and D.J. Bacon. The strengthening effect of voids, Acta. Metall., 30 (1982) 1665.

[4] Y. Osetsky. Atomic scale mechanisms of void strengthening in tungsten, Tungsten, 3 (2021) 65.

[5] Y. Osetsky. Strengthening of tungsten by coherent rhenium precipitates formed during low fluence irradiation, , Tungsten, 4 (2022) 20.

8.3 TRANSMUTATION EFFECTS IN W-BASED ALLOYS UNDER IRRADIATION

G. D. Samolyuk[*]*, Y. N. Osetskiy*
[*] *samolyukgd@ornl.gov*

8.3.1 OBJECTIVE

The objective of this task is to obtain understanding of specific effects related to transmutation in W under irradiation. Several effects are observed due to the transmutation reactions chain W→Re→Os. Accumulation of Re and Os strongly affects to W behavior and properties degradation under irradiation conditions. We study Re effects to atomic transport and segregation. The new direction is the effect of Re and Os accumulation to electrical and thermal conductivity. The main technique to study thermal and electric conductivity is density functional theory (DFT).

8.3.2 SUMMARY

This is a new direction and preliminary results have demonstrated quite strong effects of Re and Os solid solution concentration to electric and thermal conductivity. We applied the multiple scattering theory approach to calculate the electronic structure of W-Re-Os solid solutions within the frame of coherent potential approximation. This approach allows incorporating electron scattering due to both chemical disorder and disorder induced by atomic thermal vibration. The parameters of the approach used are the Debye temperature and alloy composition. The example of electric resistivity as function of Re and Os concentration estimated at 600 K is presented in Figure 58a and a comparison with the available experimental data is shown in Figure 58b.

At this stage of the research, we conclude that electronic structure of W-Re_Os alloys can be accurately calculated considering scattering effects due chemical and structural disorders. Electric resistivity strongly dependent on the ambient temperature and alloy composition as shown in Figure 58a and can be predicted by DFT modeling quite accurately as shown in Figure 58b.

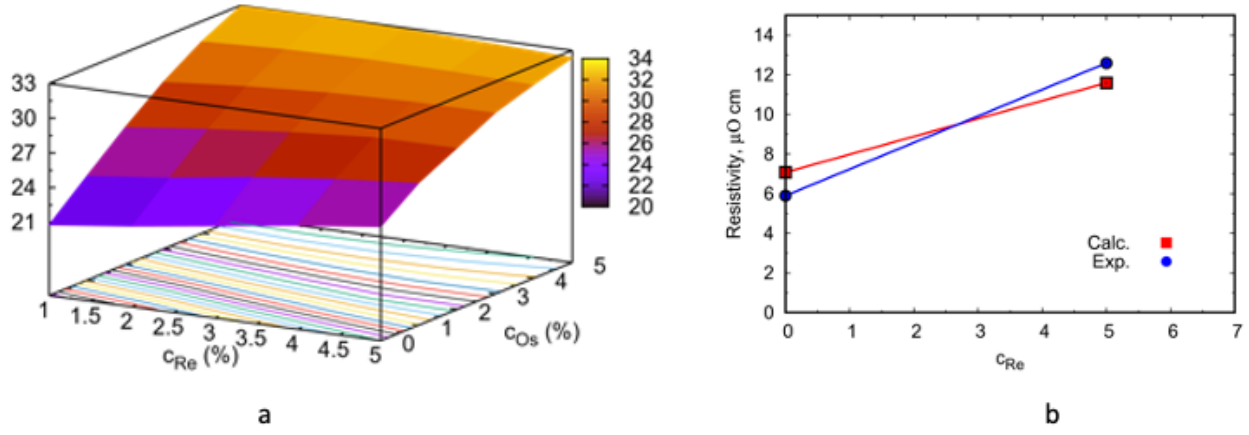

Figure 58. (a) Resistivity of W-Re-Os alloy in μΩ cm calculated at T=600 K. (b) Comparison of calculated and experimentally derived in [1] electric resistivity as function of Re content.

8.3.3 FUTURE RESEARCH

Incorporating structural disorder due to radiation induced defects.

8.3.4 REFERENCES

[1] T. Tanno, et al. Precipitation of solid transmutation elements in irradiated tungsten alloys. Materials Transactions, 49.10 (2008) 2259.

9. INTERNATIONAL COLLABORATIONS

9.1 EUROFUSION COLLABORATION PROJECT

T.S Byun, J.W. Geringer, T. Graening, Y. Katoh, M. Reith (KIT)*
**byunts@ornl.gov*

9.1.1 BACKGROUND

The Karlsruhe Institute of Technology (KIT), as an EUROfusion project, seeks to produce blanket, baseline, design-relevant materials properties data for EUROFER material variants. ORNL is under contract to assist the neutron irradiation and materials testing and evaluation tasks by preparation, irradiation, and post-irradiation examination/evaluation (PIE) of the steels to determine their suitability for use in fusion energy systems. This requires the use of several unique ORNL facilities including the HFIR, Irradiated Materials Examination and Testing (IMET) hot cell facility, and Low Activation Materials Development and Analysis (LAMDA) laboratory.

9.1.2 WORK SCOPE

The Phase I contract ended back in 2019 after completing Phase 1a project. Later, both KIT and ORNL intended to continue the collaboration project in the field of neutron irradiation and post-irradiation examination (PIE) for qualification of EUROfusion materials in simulated fusion reactor environments. The current KIT-ORNL collaboration program has two subprojects: One (Phase 1b) project is to perform the PIE of specimens that are still irradiated within the Phase 1a (EUROfusion LOT-I campaign) KIT-ORNL contract. This Phase 1b project (LOT-I PIE) can be started as soon as HFIR irradiation is completed. The second project targets the investigation of neutron irradiation damage by gas transmutation in 9%Cr steels based on isotopic tailoring. The KIT-ORNL application (Phase 2) includes various elements: (1) Extending an already running irradiation of EUROFER-54Fe to 25 dpa, (2) 54Fe and 58/60 Ni isotope procurement, fabrication of isotopic tailored EUROFER-type materials, and machining samples, (3) design and fabrication of irradiation capsules, (4) neutron irradiation to approximate target levels of 12-15, and >50 dpa, (5) PIE of EUROFER-54Fe from point (1), and (6) PIE of isotopic tailored materials from point (2) after 12-15 dpa.

9.1.3 PROGRESS AND STATUS

- After the Phase I contract ended back in 2019, the 14 remaining irradiation vehicles (i.e., rabbit capsules) completed the original planned irradiation in HFIR, which targeted at ~20 dpa (~12 cycles) and temperatures ranging between 200 to 400 °C. The capsules were loaded with Eurofer-97 alloys provided by KIT and the EUROfusion program collaborators.
- The disassembly of the Phase-1b capsules occurred during summer and PIE activities started in the fourth quarter of 2023.
- Production of Ni-58 isotope doped RAFM alloys with high helium generation rate in HFIR irradiation is underway. The HFIR irradiation for these materials will begin in the FY.

9.1.4 FUTURE PLANS

- To complete the Phase-1B PIE mechanical testing during 2024.
- To finish the design and assembly of 12 new rabbits and start irradiation during Spring of 2024.

9.2 UKAEA COLLABORATION PROJECT

T.S Byun, J.W. Geringer, Y. Lin, Y. Katoh, A. Gandy (UKAEA)*
**byunts@ornl.gov*

9.2.1 BACKGROUND

The United Kingdom Atomic Energy Authority (UKAEA) is engaged in exploring critical challenges related to the realization of fusion energy, including fundamental research on structural materials that can survive the harsh environments envisaged inside a future fusion reactor. The required research needs to use irradiation and post-irradiation testing and evaluation capabilities at UKAEA and ORNL. ORNL is under contract to perform preparation, neutron irradiation, and post-irradiation examination/evaluation (PIE) of the select materials to determine their suitability for use in fusion energy systems. This requires the use of unique ORNL facilities including the High Flux Isotope Reactor (HFIR), Irradiated Materials Examination and Testing (IMET) hotcell facility, and Low Activation Materials and Development Analysis (LAMDA) laboratory. This collaboration also includes shipping of irradiated materials and performing PIE at UKAEA.

The objective of this collaboration program is to perform systematic studies on the irradiation-induced changes in the structural materials envisaged for fusion reactor applications. The main outcomes of the research include comprehensive understanding of the irradiation-induced phenomena including materials degradation mechanisms and informative feedback to the fusion materials development and characterization activities, including the steels development works at UKAEA and ORNL.

9.2.2 PROJECT SCOPE

This collaborative research focuses to investigate the behavior of fusion structural materials under irradiation. The materials of interest, in order of priority, include the Fe-Cr binary alloys, high-Cr ODS alloys, CNA alloys, FM steel welds, austenitic stainless steels, Cu alloys and SiC/SiC composites. The two thrusts of the program are: (i) a PIE campaign on existing HFIR irradiated materials at ORNL and (ii) a new HFIR irradiation/PIE campaign for a select set of materials. The PIE activities include mechanical testing, physical property measurement, and microscopy at IMET and LAMDA facilities, which also include micromechanical testing and microscopy on irradiated materials at UKAEA. In addition to the funding for the PIE and irradiation activities at ORNL, UKAEA will dispatch assignees for PIE tasks.

9.2.3 PROGRESS AND STATUS

- The new proposal for collaborative research between ORNL and UKAEA had been reviewed and approved as a strategic partnership project (SPP) and the project was launched (funded) in February 2023.
- PIE campaign for the specimens from former JP and FMP irradiation campaigns are well underway.
- Three new irradiation capsules (UKF1 – UKF3) completed design and assembly and started HFIR irradiation in cycle 503, August 2023. These capsules are targeting a dose of 5-7 dpa during FY 2024.

9.2.4 FUTURE PLANS

- To host three to four assignments during Winter/Spring of US FY24
- Continue the non-irradiated, baseline testing on the companion samples of the FMP and/or JP capsules.
- Ship the BOR-60 samples to the UKAEA facilities.

9.3 FRONTIER IRRADIATION CAMPAIGN: IN-SITU HYDROGEN AND DEUTERIUM LOADING FOR FUSION MATERIALS UNDER NEUTRON IRRADIATION

A. Schrell, T. Koyanagi*
**schrellam@ornl.gov*

9.3.1 OBJECTIVE

To investigate the effects of neutron irradiation on hydrogen isotope retention in fusion reactor structural and functional materials, a unique irradiation vehicle filled with hydrogen or deuterium gas was designed.

9.3.2 SUMMARY

The US-Japan FRONTIER collaboration program developed the design of an irradiation vehicle to test tungsten-based disc specimens under hydrogen or deuterium environments at 500 and 800°C in HFIR. This new design enables significantly higher hydrogen pressure under irradiation than that of previous designs.

9.3.3 PROGRESS AND STATUS

The aim of this irradiation experiment is investigating how irradiation-induced defects trap hydrogen isotopes in HFIR. A schematic image of a capsule housing configuration is shown in Figure 59a. This irradiation vehicle has 32 disk specimens that are nominally 0.5 mm thick and 6.0 mm in diameter. The specimens are mainly W-based materials and composites. There are two sets of 16 specimens located on either side of the center retainer spring. Each set has 2 layers of 8 specimens stacked between SiC thermometry pieces. There are SiC thermometry bars and SiC retainer specimens pressed against the disk specimens. Tungsten foil will be inserted between SiC thermometry and disc specimens to avoid potential chemical reactions between the specimens and SiC. Thermometry and specimens are pushed to the inside surfaces of the holder with SiC springs. The target irradiation temperatures are 500 and 800ºC (Figure 59b), and the neutron fluence level will be about 2×10^{25} n/m^2 (E> 0.1 MeV).

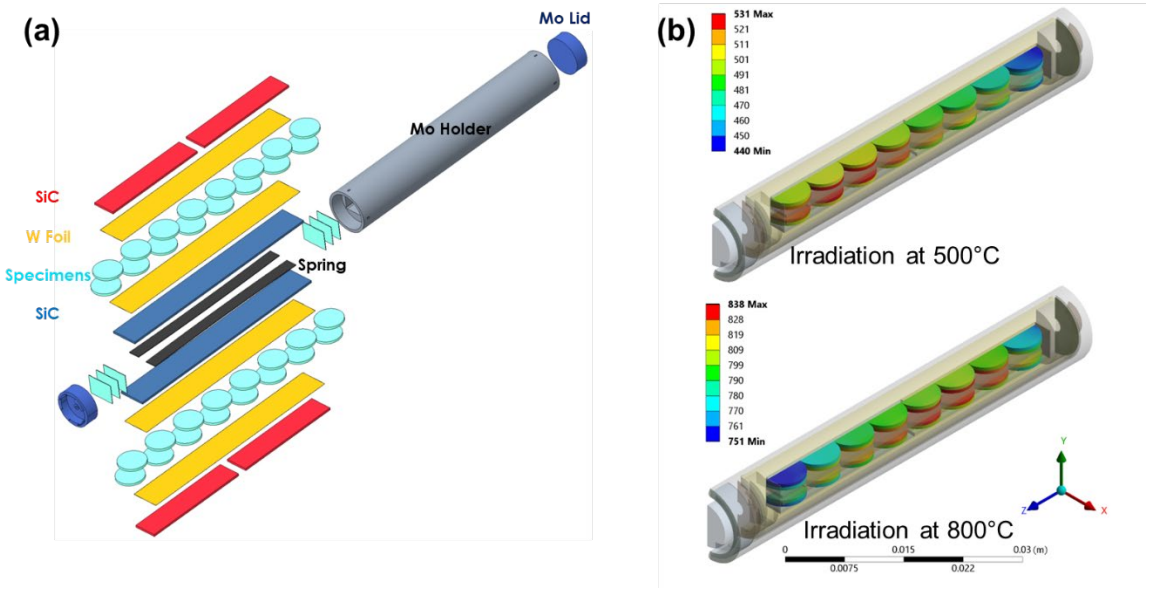

Figure 59. (a) Specimens and components of HFIR irradiation vehicle filled with hydrogen isotope and (b) simulated irradiation temperatures (in °C) of specimens. The target irradiation temperatures are 500 and 800 °C.

The outer aluminum housing, which is in contact with the HFIR water coolant, will be the ultimate gas barrier. The expected internal hydrogen or deuterium gas pressure is ~6 MPa for irradiation at 500 ºC and ~8 MPa for irradiation at 800 ºC. This novel irradiation vehicle design achieves significantly higher gas pressure than that of a previous irradiation [1]. Additionally, a welding strategy has been developed to safely seal the irradiation vehicle under hydrogen or deuterium environment.

9.3.4 FUTURE RESEARCH

Test specimens and components of the irradiation vehicle will be prepared, and then the irradiation capsules will be built. The irradiation experiment is scheduled for insertion during a HFIR cycle in fiscal year 2024.

9.3.5 REFERENCES

[1] N.O. Cetiner, Y. Hatano, J.L. McDuffee, D. Ilas, Y. Katoh, J.W. Geringer, T. Toyama, Neutron irradiation of tungsten in hydrogen environment at HFIR Fusion Engineering and Design 178 (2022) 113089.

9.4 US-JAPAN (QST) COLLABORATION ON STRUCTURAL MATERIALS

C. On, X. Chen, Y. Katoh, T. Nozawa (QST), M. Ando (QST), D. Hamaguchi (QST), T. Kato (QST), H. Tanigawa (QST)*
**onc1@ornl.gov*

9.4.1 BACKGROUND

The long-standing collaboration between the U.S. DOE and the National Institutes for Quantum Science and Technology (QST), Japan jointly pursues activities using the advanced capabilities for materials irradiation and post-irradiated examination at ORNL, especially HFIR, hot cells, and LAMDA. The focus is on ferritic steels and other advanced materials, especially the development of the materials database for the design of facilities beyond ITER. The goals include achieving DEMO-relevant performance data on structural materials that are neutron irradiated in HFIR to high levels of displacement damage.

The DOE-QST collaboration continues to steadily build the materials databases for the RAFM alloys that include F82H, ODS and EUROFER97 steels and other materials such as nuclear grade SiC composites and copper alloys. This database is being used by QST to predict changes in mechanical performance of components of a DEMO fusion reactor.

9.4.2 PROGRESS AND STATUS

Dai Hamaguchi was assigned to visit ORNL from September 2 to November 2, 2022, to perform microhardness, tensile testing, and electrical resistivity tests on Cu alloys. The annual steering committee meeting was hosted by ORNL on March 1 and 2, 2023.

The existing irradiation experiments that continue irradiation in the reactor include rabbit capsules of the JCR series, the SCF series, the FH series, and the FMP series. The low-dose rabbit capsules with reduced activation ferritic/martensitic (RAFM) steels, mainly F82H, as well as some SiC specimens, have completed irradiation while other high-dose capsules remain in the reactor. The FH rabbit capsules with F82H alloy variants targeting 80 dpa started irradiation in FY23.

As for the post-irradiation examinations, FH51, FH61, FH62, and JCR11-07 rabbit capsules were disassembled in FY23. Tensile and hardness tests on selected specimens from RB19J, FH51, FH61, and FH62 capsules were completed as well.

9.4.3 FUTURE PLANS

The next QST steering committee meeting will be hosted at ORNL in February 2024.

10. HFIR IRRADIATION PROGRAM

10.1 HFIR IRRADIATION EXPERIMENTS

*C. On**
**onc1@ornl.gov*

10.1.1 OBJECTIVE

The goal of this report is to describe the progress of the neutron irradiation experiments that were performed in the High Flux Isotope Reactor (HFIR) and the operating status of HFIR.

10.1.2 SUMMARY

During the twelve-month period starting from October 1, 2022 to September 30, 2023, a total of thirty-four rabbit capsules continued their irradiation. Eleven rabbits have completed the scheduled irradiation.

10.1.3 PROGRESS AND STATUS

Neutron irradiation experiments were performed in support of the research and development of fusion reactor materials using various materials irradiation facilities in the High Flux Isotope Reactor. The reactor operating history for the period from October 1,2022 – September 30, 2023, is detailed in Table 2.

Table 8. HFIR operating record for FY2023.

Cycle Number	Cycle End Date	Power (MWD)
500*	October 17	2062.91
501	February 4	2115.76
502	March 20	2138.24
503	May 7	2177.95

*Cycle was in two parts, due to scram (unexplained increase in power). Cycle 500A received 882.80 MWD, while cycle 500B received 1180.11 MWD.

All the fusion materials program irradiation experiments performed during this period (FY2023) used the nominally two-inch rabbit capsules, with no full-length target rod nor instrumented reflector position capsules within that period. Thirty-four target zone rabbit capsules remain in the reactor to complete the scheduled irradiations. These capsules are listed in Table 3 along with condensed information on the material, specimen type, temperature, fluence, and period of irradiation. Eleven rabbits have completed the scheduled irradiation as shown in in Table 3.

Table 9. The rabbit capsules to continue irradiation in HFIR.

Experiment Designation	Primary Materials	Specimen Types	Irradiation Temperature (°C)	Max Exposure (dpa)	Number of Reactor Cycles	HFIR Cycles Start–End
FH11	F82H-IEA / F82H-mod3	Tensile	300	80	46	496 – 541
FH12	F82H-IEA / F82H-mod3	Tensile	400	80	46	496 – 541
FH13	F82H-IEA / F82H-mod3	Tensile	500	80	46	496 – 541
FH21	F82H-IEA / F82H-mod3	Bend Bar	300	80	55	496 – 550
FH22	F82H-IEA / F82H-mod3	Bend Bar	300	80	55	496 – 550
FH23	F82H-IEA / F82H-mod3	Bend Bar	400	80	55	496 – 550
FH24	F82H-IEA / F82H-mod3	Bend Bar	400	80	55	496 – 550
FH25	F82H-IEA / F82H-mod3	Bend Bar	500	80	48	496 – 543
FH26	F82H-IEA / F82H-mod3	Bend Bar	500	80	48	496 – 543
FH31	F82H-IEA / F82H-mod3	Tensile	300	50	29	500 – 528
FH32	F82H-IEA / F82H-mod3	Tensile	400	50	29	500 – 528
FH33	F82H-IEA / F82H-mod3	Tensile	500	50	29	500 – 528
FH41	F82H-IEA / F82H-mod3	Bend Bar	300	50	35	500 – 534
FH42	F82H-IEA / F82H-mod3	Bend Bar	300	50	35	500 – 534

FH43	F82H-IEA / F82H-mod3	Bend Bar	400	50	29	500 – 528
FH44	F82H-IEA / F82H-mod3	Bend Bar	400	50	29	500 – 528
FH45	F82H-IEA / F82H-mod3	Bend Bar	500	50	29	500 – 528
FH46	F82H-IEA / F82H-mod3	Bend Bar	500	50	29	500 – 528
FMP07	F82H	Tensile	300	20	21	487 – 507
FMP08	F82H	Tensile	300	80	45	487 – 531
FMP11	F82H	Tensile	385	20	21	488 – 508
FMP12	F82H	Tensile	385	80	45	488– 532
FMP14	F82H	Tensile	525	20	21	484 – 504
FMP17	F82H	Tensile/MPC*	650	80	45	484 – 528
FMP22	F82H	Bend Bar	300	20	21	488 – 508
FMP23	F82H	Bend Bars	300	80	45	488 – 532
JCR11-03	SiC/SiC	Mini Bend Bar	950	200	100	487 – 586
JCR11-05	SiC/SiC	Mini Bend Bar	950	200	115	444 – 568
JCR11-08	SiC/SiC	Mini Bend Bar	950	200	115	444 – 560
JCR11-11	SiC/SiC	Mini Bend Bar	950	100	55	448 – 524
SCF4	SiC/SiC	Mini Flexure Bar	250	100	90	457 – 547

SCF5	SiC/SiC	Mini Flexure Bar	250	200	45	457 – 511
SCF9	SiC/SiC	Mini Flexure Bar	600	200	90	457 – 548
SCF11	SiC/SiC	Mini Flexure Bar	950	100	57	458 – 517

*MPC: Multi-Purpose Coupon

Table 10. The rabbit capsules that completed irradiation in FY2023.

Experiment Designation	Primary Materials	Specimen Types	Irradiation Temperature (°C)	Max Exposure (dpa)	Number of Reactor Cycles	HFIR Cycles Start–End
SNF01	Japan ODS FeCrAl Alloy	Tensile	400	6.5	1*	500A
SNF02	Japan ODS FeCrAl Alloy	Tensile	400	6.5	1*	500A
SNF03	ORNL ODS FeCrAl Alloy	Tensile	400	6.5	1*	500A
SNF04	ORNL ODS FeCrAl Alloy	Tensile	400	6.5	1*	500A
SNF05	Kanthal APMT FeCrAlMo Alloy	Tensile	400	6.5	1*	500A
FR11	Joint W Alloy	Disc (D6)	300	1.2	6	495 – 500
FR53	Joint W Alloy	Disc (D3)	800	0.6	3	498 – 500
FR51	Joint W Alloy	Disc (D3)	300	0.6	3	499 – 501
FR52	Joint W Alloy	Disc (D3)	500	0.6	3	499 – 501
FR12	Joint W Alloy	Disc (D6)	300	1.2	6	497 – 502
SCF8	SiC/SiC	Mini Flexure Bar	600	100	45	457 – 502

*The capsules were only irradiated for 10 days instead of one full cycle (from November 8-18, 2022).

11. AWARDS, HONORS, AND RECOGNITIONS

11.1 AWARDS DURING FY2023

1. Takaaki Koyanagi, DOE Early Career Research award from Office of Fusion Energy Sciences for proposal "Mechanistic framework for additive manufacturing of highly radiation-resistant SiC components".
2. Takaaki Koyanagi, lead-authored paper titled "Additive manufacturing of silicon carbide for nuclear applications" listed as one of the most cited articles published in the past 3 years on the Journal of Nuclear Materials website, as of April 2023. Koyanagi, T., Terrani, K., Harrison, S., Liu, J., & Katoh, Y. (2021). Additive manufacturing of silicon carbide for nuclear applications. Journal of Nuclear Materials, 543, 152577.
3. Lauren Garrison, Josina Geringer, and Yutai Katoh, co-authored paper titled "Neutron irradiation effects on the mechanical properties of powder metallurgical processed tungsten alloys" listed as one of the most cited articles published in the past 3 years on the Journal of Nuclear Materials website, as of April 2023. Miyazawa, T., Garrison, L. M., Geringer, J. W., Fukuda, M., Katoh, Y., Hinoki, T., & Hasegawa, A. (2020). Neutron irradiation effects on the mechanical properties of powder metallurgical processed tungsten alloys. Journal of Nuclear Materials, 529, 151910.
4. Xiao-Ying Yu and Yutai Katoh, DOE RENEW award from Office of Fusion Energy Sciences for proposal "Research training pathway for underrepresented minority students in advancing manufacturing for fusion power" with Vijay Vasudevan of University of Northern Texas in collaboration with PNNL and Ames.
5. Xiao-Ying Yu, Tim Graening and Guannan Zhang, DOE Machine Learning award from Office of Fusion Energy Sciences for proposal "Accelerating discovery and diagnostics of plasma-wall interactions using machine learning" with Xinghang Zhang of Purdue University.
6. Xiao-Ying Yu, named a fellow of the American Vaccum Society for "Inventions and significant contributions to advancing in situ and operando chemical inaging of condensed-phase surfaces and interfaces using vacuum-based instruments" in Portland, Oregon (Nov. 5 – 10, 2023).
7. Bruce Pint and Marie Romedenne, RENEW project, Liquid Metal-Materials Interactions in Extreme Environments, with U. New Mexico and UT.

11.2 PROFESSIONAL RECOGNITION IN FY2023 AND CONTINUING

11.2.1 TAKAAKI KOYANAGI

1. Takaaki Koyanagi, Lead organizer of the symposium "Development and Applications of Advanced Ceramics and Composites for Nuclear Fission and Fusion Energy Systems" for the 47th International Conference and Expo on Advanced Ceramics and Composites in Daytona Beach, Florida (January 22 – 27, 2023).
2. Takaaki Koyanagi, ORNL Laboratory Directed Research and Development initiative review committee for the theme "Validated Design and Evaluation of Fusion Wall Components".
3. Takaaki Koyanagi, Brookhaven National Laboratory NSLS-II Technical Review Panel.

11.2.2 XIAO-YING YU

4. Xiao-Ying Yu, Lead organizer of the symposium "Correlative Analysis and Multimodal Microscopy and Spectroscopy" for the Microscopy and Micoranalysis Conference in Minneapolis, Minnesoda (July 23 – 27, 2023).

5. Xiao-Ying Yu, Lead organizer of the symposium “Surface and Subsurface Microscopy and Microanalysis” for the Microscopy and Micoranalysis Conference in Minneapolis, Minnesoda (July 23 – 27, 2023).
6. Xiao-Ying Yu, Lead organizer of the focused topic symposium “Chemical Anaylysis and Imaging at Interfaces” for the International Conference of the American Vaccum Society in Portland, Oregon (Nov. 5 – 10, 2023).

11.2.3 XIANG (FRANK) CHEN

7. Xiang (Frank) Chen, co-chair for the ASTM E08.07.06 task group in charge of ductile-brittle transition fracture toughness standard development, i.e., ASTM E1921, hosting semi-annual subcommittee meetings, answering technical questions related to the use and revision of the standard, handing ballot for the ASTM E1921 standard.
8. Xiang (Frank) Chen, chair of ASME 2023 PVP conference CS-19-01 session: Fracture Toughness and Other Small Specimen Mechanical Properties.
9. Xiang (Frank) Chen, co-chair of ASME 2023 PVP conference MF-06-01 session: Materials and Technologies for Nuclear Power Plants.
10. Xiang (Frank) Chen, served on technical program committee for the 21st International Conference on Fusion Reactor Materials
11. Xiang (Frank) Chen, chair of Irradiation Damage session for the 21st International Conference on Environmental Degradation of Materials in Nuclear Power Systems - Water Reactors

12. PUBLICATIONS AND PRESENTATION IN FISCAL YEAR 2023

12.1 PAPERS PUBLISHED IN FY2023

1. N. Bibhanshu, M.N. Gussev, **T.S. Byun**, "Two-step deformation-induced martensitic transformation in additively manufactured High-Si stainless steel," Materials Science and Engineering A V861 (2022) 144341. DOI: j.msea.2022.144341
2. **X. Chen**, M. Serrano, R. Hernandez, **D. Lu, M. A. Sokolov**, S. M. Gonzalez De Vicente, and **Y. Katoh**, "Influence of fatigue precracking and specimen size on Master Curve fracture toughness measurements of EUROFER97 and F82H steels," Nuclear Materials and Energy V34 (2023) 101393. DOI: 10.1016/j.nme.2023.101393
3. **X. Chen, M.A. Sokolov,** S.M. Gonzalez De Vicente, **Y. Katoh**, "Specimen Size and Geometry Effects on the Master Curve Fracture Toughness Measurements of EUROFER97 and F82H Steels, Proceedings of the ASME 2022 Pressure Vessels & Piping Conference Volume 1: Codes and Standards, Las Vegas, Nevada, USA, July 17–22, 2022, V001T01A048. DOI: 10.1115/PVP2022-84514
4. **J.R. Echols, L.M. Garrison, N. Reid, C.M. Parish,** A. Hasegawa, **A. Bhattacharya, W. Zhong, D. Morrall, M. Lance**, **Y. Katoh**. "Degradation of electrical resistivity of tungsten following shielded neutron irradiation," Acta Materialia (2023): 119025. DOI: 10.1016/j.actamat.2023.119025
5. **L.M. Garrison, Y. Katoh,** T. Hinoki, N. Hashimoto, **J.R. Echols,** N. C. Reid, J. P. Allain, B. Cheng, D. Dorow-Gerspach, V. Ganesh, **H. Gietl**, S. A. Humphry-Baker, E. Lang, I. McCue, J. Riesch, L. L. Snead, G. D. W. Smith, J. R. Trelewicz, **Y. Yang,** S. J. Zinkle, "Review of Recent Progress in Plasma-Facing Material Joints and Composites in the FRONTIER U.S.-Japan Collaboration," Fusion Science and Technology V79(6) (2023) P. 662-670. DOI: 10.1080/15361055.2023.2176687
6. **T. Gräning, L. Tan**, I. Robin, **Y. Katoh, Y. Yang**, "A novel design of transitional layer structure between reduced activation ferritic martensitic steels and tungsten for plasma facing materials," Journal of Materials Research and Technology V24 (2023) P. 4285-4299. DOI: 10.1016/j.jmrt.2023.04.019.
7. **T. Koyanagi, J. J. Lee, J. R. Keiser, H. Gietl, Y. Katoh**, "Corrosion characteristics of monolithic SiC materials in beryllium-bearing molten fluoride salt," Corrosion Science V220 (2023) 111301. DOI: 10.1016/j.corsci.2023.111301
8. **Y.-R. Lin, A. Bhattacharya,** D. Chen, Y. Zhao, J.-J. Kai, J. Henry, S.J. Zinkle, "The role of Cr concentration and temperature on cavity swelling with co-injected helium in dual-ion irradiated Fe and Fe-Cr alloys," Materials & Design V223 (2022) 111134. DOI: 10.1016/j.matdes.2022.111134.
9. **Y. Lin**, **A. Bhattacharya**, S.J. Zinkle, "Analysis of position-dependent cavity parameters in irradiated metals to obtain insight into fundamental defect migration phenomena", Materials & Design V226 (2023) 111668. DOI: 10.1016/j.matdes.2023.111668
10. E. Lucon, M. L. Martin, B. L. Calvo, **X. Chen, and M.A. Sokolov**, "Assessment of Different Approaches for Measuring Shear Fracture Appearance in Charpy Tests," Journal of Testing and Evaluation V51(5) (2023) DOI: 10.1520/JTE20220691

11. I.K. Robin, **T. Gräning, Y. Yang**, S. B. Haider, E. A. Lass, **Y. Katoh**, and S. J. Zinkle, "Evaluation of Tungsten—Steel Solid-State Bonding: Options and the Role of CALPHAD to Screen Diffusion Bonding Interlayers," Metals V13 (2023) 1438. DOI: 10.3390/met13081438

12. **M. Romedenne**, Y. Zhang, **Y-F. Su, B.A. Pint**. "Evaluation of the interaction between SiC, pre-oxidized FeCrAlMo with aluminized and pre-oxidized Fe-8Cr-2W in flowing PbLi," Journal of Nuclear Materials V581 (2023) 154465. DOI: 10.1016/j.jnucmat.2023.154465

13. D.J. Sprouster, J. Gentile, M. Ouyang, C. Killeen, J.R. Trelewicz, **W. Zhong, Y. Yang**, D. Bhardwaj, W.S. Cunningham, M.M.A. Shawon, B. Cheng, D. Olds, H. Yan, A. Pattammattel, **L. Tan**, L.L. Snead, "Sintered nanostructured alloys for advanced fusion energy applications," Journal of Nuclear Materials V586 (2023) 154683. DOI: 10.1016/j.jnucmat.2023.154683.

14. H. Tanigawa, X. Ruan, T. Nozawa, and **Y. Katoh**, "Probabilistic failure assessment of an irradiated DEMO breeding blanket component under ferromagnetic loads: Impacts of material data scattering and uncertainty in local stress intensities," Journal of Nuclear Materials V574 (2023) 154148. DOI: 10.1016/j.jnucmat.2022.154148

15. C. N. Taylor, M. Shimada, Y. Nobuta, M. I. Kobayashi, Y. Oya, Y. Hatano, **T. Koyanagi**, "Surface chemistry of neutron irradiated tungsten in a high-temperature multi-material environment," Nuclear Materials and Energy V34 (2023) 101323. DOI: 10.1016/j.nme.2022.101323

12.2 **REPORTS ISSUED IN FY2023**

1. —, “Fusion Materials Semiannual Progress Report for the Period Ending December 31, 2022,” Volume 73
2. —, “Fusion Materials Semiannual Progress Report for the Period Ending June 30, 2022,” Volume 72
3. Y. Katoh, C. On, and C. M. Parish, “Fusion Materials Research at Oak Ridge National Laboratory in Fiscal Year 2022,” ORNL/TM-2023/2970
4. C. M. Parish, Y. Katoh, and C. On, “ORNL Fusion Materials Program Quarterly Progress Report Highlight for the 3rd and 4th Quarters of FY2022.” (Limited distribution)
5. C. M. Parish, Y. Katoh, and C. On, “ORNL Fusion Materials Program Quarterly Progress Report Highlight for the 1st Quarter of FY2023.” (Limited distribution)
6. C. M. Parish, Y. Katoh, and C. On, “ORNL Fusion Materials Program Quarterly Progress Report Highlight for the 2nd Quarter of FY2023.” (Limited distribution)
7. C. M. Parish, Y. Katoh, and C. On, “ORNL Fusion Materials Program Quarterly Progress Report Highlight for the 3rd Quarter of FY2023.” (Limited distribution)

12.3 **PAPERS SUBMITTED IN FY2023**

1. **M. Romedenne**, C. S. Hawkins, D. Pierce, J. Jun, S. Dryepondt, **B. A. Pint,** "Evaluation of liquid metal embrittlement of steels in liquid lithium," Journal of Nuclear Materials

12.4 PRESENTATIONS DELIVERED IN FY2023

AMERICAN PHYSICAL SOCIETY (APS)

W. Zhong, L. Tan, Y. Yang, T. Graening, T. Wei, K. Field, **Y. Katoh**, The Development of Castable Nanostructured Alloys for Fusion Reactor First-Wall/Blanket Applications, American Physical Society, Division of Plasma Physics, Oct 17-21, 2022, Spokane, Washington.

NUCLEAR MATERIALS (NUMAT)

J.R. Echols, L. Garrison, W. Zhong, Y. Katoh, Effects of irradiation temperature and Re/Os content on the Thermal Diffusivity of Neutron-Irradiated W and W-Re alloys, NuMAT, Oct 24-28, 2022, Gent, Belgium.

ARPA-E FUSION PROGRAMS ANNUAL MEETING

Y. Yang, ARPA-E Annual Review Meeting: "Development of Castable Nanostructural Alloys for fusion first wall/blanket application," June 14-15, Boston, MA, 2023 ARPA-E Fusion Programs Annual Meeting.

KIT EUROFUSION MEETING

T. Graening, KIT EUROFusion Meeting: "Transition Layer Design for Fusion Components," April 2023, Karlsruhe, Germany

PLASMA FACING MATERIALS AND COMPONENTS (PFMC) 2023

T. Graening, PFMC 2023: "Transition Layer Design for Divertor and First Wall Components: From Tungsten to Steel," April 2023, Bonn, Germany

DOE ARPA-E FUSION ENERGY WORKSHOP

B. A. Pint, "'Testing,' Accelerating evaluations of new fusion materials," DOE ARPA-E Fusion Energy Workshop, New Orleans, LA, March 2023.

THE MINERALS, METALS, AND MATERIALS SOCIETY (TMS) 2023

1. **C. M. Parish**, "Characterizing Transmutation Products in Materials via STEM and Machine Learning," invited talk at TMS 2023, San Diego, CA, March 2023.
2. M. Gilbert, A. Bhattacharya, P. Edmondson, J.-C. Sublet, "Experimental Validation of Simulated Transmutation Predictions for Fusion Materials," invited talk at TMS 2023, San Diego, CA, March 2023.
3. **Y. Osetskiy, G. Samolyuk**, "Ab initio and classical molecular dynamics study of Re transport in W," contributed talk at TMS 2023, San Diego, CA, March 2023.
4. **Y. Osetskiy, G. Samolyuk**, "Estimating the strengthening parameters for irradiated alloys using atomic scale modeling," contributed talk at TMS 2023, San Diego, CA, March 2023.
5. **G. Samolyuk**, **P. Edmondson**, **Y. Osetskiy**, "Stability of a Li2TiO3 Candidate Solid-breeder Material Following Li Transmutation," contributed talk at TMS 2023, San Diego, CA, March 2023.
6. **W. Zhong**, **L. Tan**, "Initial Microstructure Effects on Radiation Response in Ferritic-Martensitic Steels (Ta alloyed and Nb-alloyed)," contributed talk at TMS 2023, San Diego, CA, March 2023.

7. E. Proehl, **L. Tan**, **W. Zhong**, D. Sprouster, C. Lear, S. Zinkle, "Laves phase volume fraction quantification in creep-ruptured optimized Grade 92 steel,", contributed talk at TMS 2023, San Diego, CA, March 2023.
8. T.M. Kelsy Green, **T. Graening**, **W. Zhong**, **Y. Yang**, K.G. Field, "Dynamic Sink Strength Effects of Irradiation-Induced Precipitates in Advanced Steels for Fusion Reactor Applications," contributed talk at TMS 2023, San Diego, CA, March 2023.

2023 ASME PRESSURE VESSELS & PIPING CONFERENCE (PVP 2023)

X. Chen, M. Serrano, R. Hernandez, **M. Sokolov,** "Specimen Size Effect on Homogeneity Screening of Master Curve Results of EUROFER97 and F82H Steels," contributed talk at PVP 2023, Atlanta, GA, July 2023

INTERNATIONAL CONFERENCE ON PROCESSING & MANUFACTURING OF ADVANCED MATERIALS PROCESSING, FABRICATION, PROPERTIES, APPLICATIONS (THERMEC'2023)

X. Chen, M. Serrano, R. Hernandez, **M. Sokolov, Y. Katoh,** S. Gonzalez De Vicente, "Specimen Size Effect on the Master Curve Fracture Toughness Characterization of EUROFER97 and F82H Steels," invited talk at Thermec'2023, Vienna, Austria, July 2023

THE GORDON RESEARCH CONFERENCE

M. Romedenne, D. Pierce, C.S. Hawkins, **B.A. Pint,** "Liquid metal embrittlement (LME) assessment of 4340 steel and F82H in Lithium," poster presented at the Gordon Research Conference on High temperature corrosion, New London, NH, July 2023.

15TH INTERNATIONAL SYMPOSIUM ON FUSION NUCLEAR TECHNOLOGY (ISFNT)

B.A. Pint, M. Romedenne, D. Sulejmanovic, "Compatibility assessments for fusion applications: Sn, Pb-Li, FLiBe," presentation at ISFNT 2023, Las Palmas de Gran Canaria, Spain, September 2023

FUSION NEUTRONICS MEETING

W. Zhong, **FW Wiffen**, **Y. Katoh**, "Neutronics Support for the Fusion Materials Program," Fusion Neutronics Meeting, Knoxville, TN, January 2023